



THE HONG KONG  
POLYTECHNIC UNIVERSITY

香港理工大學

Pao Yue-kong Library

包玉剛圖書館

---

## Copyright Undertaking

This thesis is protected by copyright, with all rights reserved.

**By reading and using the thesis, the reader understands and agrees to the following terms:**

1. The reader will abide by the rules and legal ordinances governing copyright regarding the use of the thesis.
2. The reader will use the thesis for the purpose of research or private study only and not for distribution or further reproduction or any other purpose.
3. The reader agrees to indemnify and hold the University harmless from and against any loss, damage, cost, liability or expenses arising from copyright infringement or unauthorized usage.

### IMPORTANT

If you have reasons to believe that any materials in this thesis are deemed not suitable to be distributed in this form, or a copyright owner having difficulty with the material being included in our database, please contact [lbsys@polyu.edu.hk](mailto:lbsys@polyu.edu.hk) providing details. The Library will look into your claim and consider taking remedial action upon receipt of the written requests.

ROBUST FRINGE PROJECTION  
PROFILOMETRY

BUDIANTO

Ph.D

The Hong Kong Polytechnic University

2016

The Hong Kong Polytechnic University

Department of Electronic and Information Engineering

# Robust Fringe Projection Profilometry

Budianto

A thesis submitted in partial fulfillment of the requirements

for the degree of Doctor of Philosophy

October 2015

## CERTIFICATE OF ORIGINALITY

I hereby declare that this thesis is my own work and that, to the best of my knowledge and belief, it reproduces no material previously published or written, nor material that has been accepted for the award of any other degree or diploma, except where due acknowledgement has been made in the text.

\_\_\_\_\_ (Signed)

Budianto \_\_\_\_\_ (Name of student)

*Dedicated to my wife Eveline Nathalia and my parents*

## ABSTRACT

Fringe projection profilometry (FPP) is a popular optical three-dimensional (3D) scanning methodology, which allows real-time measurements of an object's 3D information. It has salient advantages of low cost, high resolution, fast data acquisition, and full-field measurement as compared to other existing 3D scanning approaches. This thesis focuses on the development of robust FPP methods for obtaining accurate 3D estimation of the objects from incomplete or degraded observations due to the interference in the working environment.

In a practical FPP procedure, some parts of the fringe images can be masked by the highlights generated due to the reflection of the surrounding global illuminations. In this research, an iterative inpainting regularization algorithm is proposed to restore the missing fringe patterns. The new algorithm detects the highlight regions automatically using a Gaussian mixture model (GMM). The geometrical structure of the missing fringe pattern is then sketched and used as the initial guess to guide the iterative regularization process. The simulation and experimental results show that the proposed method can detect the highlight regions and inpaint the missing fringe pattern accurately. They show that the proposed approach outperforms the traditional approaches in both quantitative and qualitative evaluations.

Traditional FPP methods have the ambiguity problem that only the wrapped phase information (confined to  $-\pi$  to  $\pi$ ) of the fringe pattern can be measured, although the true phase information is required. Various phase unwrapping methods have thus been proposed for the FPP; however, most of them have problem if the captured fringe images have a complex scene, for instance, containing multiple and occluded

objects, having different kinds of artifact, such as high noise level in dark regions and discontinuities in fringe pattern, etc. In this research, a new marker encoding and detection algorithm is proposed to assist the phase unwrapping procedure to solve the ambiguity problem. For the proposed algorithm, unique markers that encode the true phase information of the fringes are embedded into the fringe pattern. Using the proposed marker detection and period order estimation algorithm, the markers are first detected and the true phase information is estimated accurately using a two-dimensional dual tree complex wavelet transform analysis. Then this true phase information is used to facilitate the phase unwrapping algorithm at the later stage. As shown in the simulation and experimental results, the proposed scheme is robust in obtaining the correct 3D model of objects with fringe images of complex scene. Besides, the algorithm is simple that does not introduce a significant burden to the FPP process computationally.

The above marker encoding and detection algorithm encodes the true phase information based on the position of the markers in the fringe pattern. A natural question arises if there is other form of encoding method that can give an even better performance in terms of robustness. In this research, we propose another algorithm which embeds a set of textural code patterns into the fringe pattern. It encodes the true phase information based on the morphological structure of the textural code patterns. During the fringe analysis procedure, the code patterns are separated from the fringe pattern using a modified morphological component analysis method. They are then decoded using a discriminative dictionary which is learned to give the sparse representations of the code patterns. They are integrated to a multilevel quality guide phase unwrapping procedure to allow the phase unwrapping to be carried out in fringe images of complex scene efficiently. The experimental results show that the

proposed algorithm is superior over the traditional approaches in terms of robustness. It is also computationally efficient as it requires only approximately 300ms when running on a normal personal computer in the Matlab environment.

# LIST OF PUBLICATIONS

## International Journal Papers

1. B. Budianto, and Daniel P.K. Lun, “Robust Fringe Projection Profilometry via Sparse Representation,” *IEEE Trans. Image Process.*, vol. 25, no. 4, pp. 1726-1739, 2016.
2. B. Budianto, and Daniel P.K. Lun, “Inpainting for Fringe Projection Profilometry Based on Geometrically Guided Iterative Regularization,” accepted in *IEEE Trans. Image Process.*, vol. 24, no. 12, pp. 5531-5542, 2015.
3. B. Budianto, Daniel P.K. Lun, and T.C. Hsung, “Marker Encoded Fringe Projection Profilometry for Efficient 3D Model Acquisition,” *Applied Optics*, vol. 53, no. 31, pp. 7442-7453, 2014.

## International Conference Papers

1. B. Budianto and Daniel P. K. Lun, “Gabor Feature Based Discriminative Dictionary Learning for Period Order Detection in Fringe Projection Profilometry,” in *Proc. 2015 Asia-Pacific Signal and Information Processing Association Annual Summit and Conference (APSIPA ASC 2015)*, pp. 283-288, December 2015.
2. B. Budianto and Daniel P. K. Lun, “Inpainting for Fringe Projection Profilometry Based on Iterative Regularization,” in *Proc. 2014 International Conference on Digital Signal Processing (DSP 2014)*, pp.668-672, August 2014.
3. B. Budianto and Daniel P.K. Lun, “Efficient 3-Dimensional Model Reconstruction Based on Marker Encoded Fringe Projection Profilometry,” in *Proc. 2014 International Conference on Acoustics, Speech and Signal Processing (ICASSP 2014)*, pp.574-578, May 2014.

## ACKNOWLEDGEMENTS

During my doctoral study at HK Polytechnic University, I have had a privilege to become intimately familiar with the study of digital image, a representation of reflected light from physical scene in term of pixels. And when properly considered, naturally lead one's mind to the image of the invisible God, Jesus Christ, the light of the world who gives the light of life (John 8:12). All praise, honor, and glory to my Lord, Jesus Christ for His riches grace and mercy to accomplish this thesis.

Completion of this thesis was possible with the support of many people. First of all, I would like to express my deep gratitude to my PhD supervisor, Dr. Daniel P.K. Lun, for his guidance, encouragement, and advices which are the most appreciated. I am also thankful to him for carefully reading, commenting, and revising the draft of this thesis. He has been always given me lots of insights and constructive comments in every discussions that helped me sort out the technical details of my research works. I am also grateful for the privilege being his teaching assistants in his laboratory works and for his patience during the course of this research, without which the completion of this research work would not have been possible. Thanks to the Centre for Signal Processing, Department of EIE, HK Polytechnic University, and Research Grants Council of the HKSAR, China which provide facilities, research studentship, and other supports during my study.

My sincere thanks to Prof. Wan-Chi Siu for being an inspiring lecturer and his tremendous views on signal processing. His insightful suggestions during the weekly meeting and dinners also gives invaluable ideas to this research as well. Also thanks to Dr. Chris Y.H. Chan and Dr. Kwok-Tung Lo who has taught me the fundamental concept of image and audio processing and Prof. Michael G. Somekh who introduce me to bioengineering. Thanks to Dr. Zeru Chi, Dr. Yui-Lam Chan, Dr. Bonnie Law, and all other academic staffs whom I cannot name them one by one.

I also wish to thanks to the general office staffs of EIE and the research office staffs who has provided me administration assistants during my study. Special thanks to Cora Au, who always assists me, Suki Chu, and all other general office staffs of EIE.

Also thanks to May Chu who has helped me in my student visa application and all other research related administrative services.

My experience at Polyu was greatly enhanced by the interaction with colleagues at EIE. Glory Lee who always give a great help for various daily lifes in HK and PolyU particularly; Cheung Siu Chak and Hui Wai Lam's supports in any technical issues at the office. The friendship with Shen Tak Wai, William Lam, Kwok Tung, Li Tiangtian, Dr. Cheng Kin On, Dr. Tsang Sik Ho, Wu Hao, Huang Junjie, Zhang Hungbin, Yang Xuefei, Wu Hao, Shi Chao, Animasahun I. Oluwaseun, Nuwan, Turan Cigdem, and many other friends also made difficult times more bearable and manageable.

I feel really grateful also for the great fellowship with brothers and sisters in Christ that I have found in Hong Kong that giving me such a huge supports and motivations; Thanks to your support and prayer of my friends (Daniel, Claudia, Yuliana, and others) at PRII HK. Thanks to Ricky Lam, Diane Lam, Belinda, and all other choir members at TST Baptist church.

I wish to thank to my beloved parents for their supports, and especially their guidance and also the encouragements given. For their love and understanding that are the most precious things for my life. The prayer, love, passion, and support of my wife, Eveline, give such a great encouragements for me during my study and until now. Thank you for lunch box that will surely give me energy to work hard to accomplish this research. Besides, her proofread of this thesis is also appreciated even without knowing all those technical terms written in it.

Finally, I thank God for granting me talents and opportunities that made this possible and for the Salvation. Fundamentally, everything is vanity without Him.

Soli Deo Gloria, Hong Kong, September 2015.

# TABLE OF CONTENTS

CERTIFICATE OF ORIGINALITY .....	ii
Abstract .....	iv
List of publications.....	vii
Acknowledgements .....	viii
Table of Contents .....	x
List of Figures .....	xiii
List of Tables.....	xxi
1 INTRODUCTION .....	1
1.1 Optical 3D Scanning System.....	2
1.1.1 Time-of-Flight Camera .....	2
1.1.2 Stereo Vision.....	3
1.1.3 Structure Light System.....	3
1.1.4 Active Stereo Vision .....	5
1.2 Motivation and Objectives .....	5
1.3 Thesis Structure .....	7
2 Fringe Pattern Projection Profilometry .....	9
2.1 Principle of FPP Methods.....	10
2.1.1 Fringe Analysis .....	12
2.1.2 Phase Unwrapping Process .....	15
2.2 FPP in the Real Working Environment.....	17
2.2.1 Noise and Bias Problem.....	18

2.2.2	Global Illumination .....	21
2.2.3	Ambiguity Problem .....	22
2.3	DTCWT FPP Framework.....	25
3	Inpainting Fringe Pattern Using Geometrically Guided Iterative Regularization	30
3.1	Related Works .....	31
3.2	Sparse Representation based Inpainting.....	34
3.3	Highlight Detection .....	37
3.3.1	Highlight Detection using Interpolated 2D-DTCWT Coefficients.....	38
3.3.2	Highlight Detection using GMM Smoothed Fringe Image.....	41
3.4	Geometric Sketching of Fringe Pattern .....	44
3.4.1	T-Junction Point Detection .....	44
3.4.2	Finding Possible Configurations .....	48
3.4.3	Curve Completion .....	50
3.4.4	Selecting the Best Configuration .....	52
3.5	Simulation and Experiment .....	54
3.6	Summary .....	62
4	Period Order Encoded Complex Wavelet Transform Profilometry.....	64
4.1	Related Works .....	65
4.2	Proposed Marker Coding for Consistent Phase Unwrapping.....	67
4.3	Period Order Estimation Algorithm .....	70
4.4	Simulation and Experiment Result.....	76
4.5	Summary .....	86

5	Robust Fringe Projection Profilometry via Sparse Representation .....	87
5.1	Background .....	88
5.1.1	MCA based on Variable Splitting using SALSA.....	89
5.1.2	Dictionary Learning .....	90
5.2	Proposed Algorithm .....	92
5.2.1	Encoding of the Period Order Information .....	92
5.2.2	Overview of the Proposed Decoding Algorithm.....	93
5.2.3	The Modified MCA .....	96
5.2.4	Dictionary Learning .....	100
5.2.5	Applying to Phase Unwrapping .....	102
5.3	Experiment .....	107
5.4	Summary .....	113
6	CONCLUSIONS AND FUTURE WORKS .....	115
6.1	Conclusions .....	115
6.2	Future Works .....	118
	Appendix A.....	120
7	Appendix B .....	122
8	REFERENCES.....	124

# LIST OF FIGURES

Figure 1-1. Mesa Imaging SR4000 (left), PMD Technologies 3D ToF Camera (the second column) , Depth Sense 325 from softkinectic (the third column) and the principle of ToF camera (right) adopted from [11]..... 3

Figure 2-1 Phase based fringe projection profilometry arrangement in the crossed-optical-axes geometry. .... 10

Figure 2-2. Frequency spectra of the deformed fringe pattern [44]. .... 12

Figure 2-3 the fringe pattern with bias (left) and the intensity plot at row indicated by red line (right) ..... 19

Figure 2-4 Illustration of direct illumination and global illumination from other light sources in the scene [73]. .... 22

Figure 2-5 Illustration of the ambiguity problem due to isolated multiple objects [36].  
..... 23

Figure 2-6 Illustration of the ambiguity problem due to occlusions [36]. .... 24

Figure 2-7. The conventional DTCWT FPP framework (adopted from [67, 69]).... 26

Figure 2-8. Realization of the 2D DTCWT using four DWT trees ( $J=2$ ) ..... 26

Figure 2-9. Enhanced DTCWT based FPP Framework ..... 27

Figure 3-1 (a) The texture image of a plastic banana; (b) the fringe image captured using an FPP system; and (c) the 3D model (depth map) evaluated from the fringe image in (b). .... 31

Figure 3-2 A fringe pattern with highlight. The entire fringe image is denoted by  $R$ ; the highlight region and its contour are denoted by  $\Omega$  and  $\partial\Omega$  , respectively. .... 35

Figure 3-3 (a) The fringe image of a plastic banana; (b) histogram of the fringe pattern, dash lines are the threshold obtained by the Otsu method [114] (left) and the minimum error method [115] (right); (c) the result using the Otsu method; and (d) the result of the minimum error method. ....	37
Figure 3-4 (a) The texture image of a ceramic plate with a highlight region; and (b) the fringe image of the plate with the highlight region. (c) Interpolated magnitude of complex wavelet coefficients at the coarse level; and (d) the estimated highlight region (white). .....	40
Figure 3-5 Histogram, mixtures and pdf of two classes. The histogram is obtained after the smoothing operation. The dash line is the optimum threshold. ....	42
Figure 3-6 The object and its highlight area obtained by thresholding the histogram with the optimum threshold (see solid red line) obtained from the proposed multi-classes GMM approach. ....	43
Figure 3-7 (a) T-junction with binary label for maxima (red circle) and minima (blue circle); (b) the orientation of T-junction with labels: the leaving T-junctions are green in color; and (c) the curve generated between pairwise compatible T-junction using the Bezier curve (blue curve) and the Clothoid (red curve). .....	46
Figure 3-8 (a) Gradient of the fringe pattern; (b) direction of the fringe pattern.....	46
Figure 3-9 The flow of T-junction: inward, outward, and transition.....	47
Figure 3-10 Curves generated by the Bezier functions. A C-shape curve (left) and a S-shape curve (right). .....	51

Figure 3-11	Some possible configurations obtained from Algorithm 1 given the starting transition T-junctions (red arrow). (a) Non-optimal configuration; and (b) the optimal configuration.....	52
Figure 3-12.	The 2D-DTCWT regularization on a fringe pattern. (a) Original fringe pattern after the curve interpolation. Note that the rest missing area is initialized to zero; (b) and (c) the regularization results after several iterations.....	54
Figure 3-13.	The object used in the simulation. (a) A computer generated 3D object “peak” (ground truth); (b) the deformed fringe pattern; (c) the deformed fringe pattern with noise and the circle shape mask added; (d) the deformed fringe pattern with noise and the oval shape mask added; ..	55
Figure 3-14.	The object used in the simulation. (a) A computer generated 3D object “peak” (ground truth); (b) the deformed fringe pattern; (c) the deformed fringe pattern with noise and the mask added; (d) the deformed fringe pattern with noise and the oval shape mask added; .....	55
Figure 3-15.	Experiment with a ceramic plate with highlight. (a) The fringe image; (b) the reconstructed 3D model; (c) the generated depth image using the conventional approach; (d) the blow up of the highlight region in (c); (e) The generated depth image using the proposed approach; and (f) the blow up of the highlight region in (e). .....	58
Figure 3-16.	Comparison with other inpainting methods on a rectangular melamine plate with long highlight. The 1st column: (1st row) The fringe image with highlights and the 3D model reconstructed using the proposed method; (2nd row) iterative regularization with the oriented 2D-DTCWT; (3rd row) the exemplar based inpainting method [102, 122];	

(4rd row) the wrapped phase image inpainting (WP-II) [54]; The 2nd column: (1st row) the vector-valued image regularization with PDEs (VVIR-PDE) [123]; (2nd row) the adaptive inpainting algorithm based on DCT induced wavelet regularization (AI-DCT-WR) [106]; (3rd row) the image inpainting approach using spatially adaptive iterative singular-value thresholding algorithm (SAIST) [124]; (4th row) the proposed method..... 60

Figure 3-17. Comparison with other inpainting methods on a melamine plate with large highlights. The 1st column: (1st row) The fringe image with highlights and the 3D model reconstructed using the proposed method; (2nd row) iterative regularization with the oriented 2D-DTCWT; (3rd row) the exemplar based inpainting method [102, 122]; (4rd row) the wrapped phase image inpainting (WP-II) [54]; The 2nd column: (1st row) the vector-valued image regularization with PDEs (VVIR-PDE) [123]; (2nd row) the adaptive inpainting algorithm based on DCT induced wavelet regularization (AI-DCT-WR) [106]; (3rd row) the image inpainting approach using spatially adaptive iterative singular-value thresholding algorithm (SAIST) [124]; (4th row) the proposed method ..... 61

Figure 3-18. Performance of the proposed method for objects with complex shape and strong color variation. .... 62

Figure 4-1. The original sinusoidal fringe pattern (for a particular row) and the markers (top). Resulting fringe pattern with markers embedded (bottom). .... 68

Figure 4-2. A fringe pattern with markers located at different phase angles of the sinusoidal fringes. ....	69
Figure 4-3. Marker detection results: (a) using only the maxima of Q; (b) the zoom in version which shows many falsely detected markers (circled). ....	72
Figure 4-4. A comparison of local phase and local relative phase: (left) local phase; (right) local relative phase. ....	74
Figure 4-5. (a) Marker detection results after using the proposed thresholding method; (b) the zoom in version. ....	75
Figure 4-6. The object used in the simulation. (left) A computer generated 3D cone (ground truth); (right) the deformed fringe pattern.....	77
Figure 4-7. Comparison of the proposed algorithm and the traditional phase unwrapping method. (a) texture image; (b) fringe pattern illumination; (c) reconstructed 3D shape with texture using the proposed method; (d) reconstructed 3D shape with height profile using the proposed method; (e) reconstructed 3D shape with texture using the traditional DTCWT+Goldstein; and (f) reconstructed 3D shape with height profile using the traditional DTCWT+Goldstein .....	79
Figure 4-8. (a) Texture images (b) markers encoded fringe image; (c) one of the PMP-DF fringe images. ....	80
Figure 4-9. Texture images captured at low ISO (100) and different shutter speeds: (left) shutter speed 1/15s and (right) shutter speed 1/30s .....	81
Figure 4-10. (Left column) A comparison of the proposed algorithm and PMP-DF with fringe images captured at ISO 100 and shutter speed 1/15s: (a) the height profile generated by the proposed method, (b) the 3D shape with texture generated by the proposed method, (c) the height profile	

generated by PMP-DF, (d) the 3D shape with texture generated by PMP-DF. (Right column) A comparison of the proposed method and PMP-DF with fringe images captured at ISO 100 and shutter speed 1/30s: (e) the height profile generated by the proposed method, (f) the 3D shape with texture generated by the proposed method, (g) the height profile generated by PMP-DF, (h) the 3D shape with texture generated by PMP-DF. .... 82

Figure 4-11. Texture images captured at high ISO (1600) and different shutter speeds: (left) shutter speed 1/80s and (right) shutter speed 1/125s. .... 83

Figure 4-12. (Left column) A comparison of the proposed algorithm and PMP-DF with fringe images captured at ISO 1600 and shutter speed 1/80s: (a) the height profile generated by the proposed method, (b) the 3D shape with texture generated by the proposed method, (c) the height profile generated by PMP-DF, (d) the 3D shape with texture generated by PMP-DF. (Right column) A comparison of the proposed method and PMP-DF with fringe images captured at ISO 1600 and shutter speed 1/125s: (e) the height profile generated by the proposed method, (f) the 3D shape with texture generated by the proposed method, (g) the height profile generated by PMP-DF, (h) the 3D shape with texture generated by PMP-DF. .... 84

Figure 4-13. 3D model reconstruction of a human hand. (a) Texture image; (b) the fringe image; (c) wrapped phase of the hand; (d) the detected markers; (e) the reconstructed 3D model with texture image; and (f) the reconstructed 3D model. .... 85

Figure 5-1. 5×5 pixels binary textons (most left), the code pattern generated by textons (second column), and the coded fringe pattern with one unique texture assigned for each k-value (column three).....	93
Figure 5-2. The captured coded fringe pattern of a shiny flat board.....	94
Figure 5-3. The captured coded fringe pattern of a jar .....	95
Figure 5-2. Flowchart of the proposed dictionary learning based FPP method for 3D reconstruction.....	96
Figure 5-3. Input of the coded fringe pattern. ....	97
Figure 5-4. the coded fringe pattern decomposition using TQWT with different threshold value. The result of decomposition: the fringe pattern, $G1$ (top row) and the code pattern $G2$ (bottom row) with its regularization parameter $\lambda$ . ....	99
Figure 5-6. Code patterns and Q-map at various locations.....	104
Figure 5-7. Relationship between the root mean square (RMS) reconstruction error (phase error) and the number of periods $P$ . The number of patterns used by PMP-DF is six whereas the number of patterns used by other methods is three. ....	108
Figure 5-8. Objects that form complex scenes. (a) A head sculpture and a plastic toy; (b) a plastic banana occluded by a jar; (c) a jar with texture and highlights; (d) a plastic bag with regular textual pattern; and (e) a ceramic plate with complex texture cover the whole object.....	110
Figure 5-9. 3D reconstruction of various complex scenes with multiple objects, occlusion, highlight regions, and textures. (First row) Results of the conventional PSP+Goldstein method; (second row) results of the PSP-Speckle method; (third row) results of the proposed method; and (fourth	

row) the ground truth. The numbers under the images of the first 3 rows are the SNR as compared with the ground truth. .... 112

Figure 5-10. A scene of complex objects (the first column). Result of 3-D reconstruction using the proposed algorithm (second column). The top view of 3D reconstruction (the last column). .... 113

## LIST OF TABLES

Table 3-1 Comparison of inpainting results on the object “cone” with an oval shape mask and a circle shape mask respectively .....	57
Table 3-2 Comparison of inpainting results on the object “peak” with an oval shape mask and a circle shape mask respectively .....	57
Table 3-3 Comparison of execution time.....	57
Table 4-1 Comparison between the proposed method, the conventional DTCWT+Goldstein method, and the WFF+Goldstein method in terms of execution time and SNR.....	78

# CHAPTER 1

## INTRODUCTION

Optical three-dimensional (3D) scanning is an active research field recently. Related techniques have been successfully applied in various non-contact 3D measurement applications such as medical tomography [1], 3D scene reconstruction [2, 3], 3D face scanning [4], industrial quality control [5, 6], and 3D reconstruction of complex objects, e.g., multiple objects with strong global illumination [7-10]. Among the existing optical 3D scanning techniques, the fringe projection profilometry (FPP) has salient advantages of low cost, high resolution, fast data acquisition, and full-field measurement. For a typical FPP procedure, fringe patterns are projected onto the target objects. Due to the 3D structure of the objects, the fringe patterns as shown on the object surface will be distorted. By measuring the amount of distortion (expressed in terms of the phase changes in the fringe patterns), the 3D information of the objects can be inferred.

While many traditional FPP methods can perform satisfactorily in simulations, their performance can degrade significantly in actual practice. It is often due to the assumption that the phase changes of the fringe patterns can be completely observed

and captured by an imaging device, such as a digital camera. It is unfortunately not the case in many practical working environments where different kinds of interference can seriously affect the quality of the captured images. In this thesis, we develop a series of robust FPP methods which can accurately estimate the phase information of the fringe patterns from low quality captured images. Before further explaining the motivation and objective of this research, let us have a brief review about the existing 3D scanning technologies and their limitations that lead to this study.

## 1.1 OPTICAL 3D SCANNING SYSTEM

In last two decades, the development of computers and optical components has contributed significantly to the achievement and advancement of optical 3D scanning systems. In this section, several widely adopted optical 3D scanning systems are briefly reviewed.

### 1.1.1 TIME-OF-FLIGHT CAMERA

A time of flight (ToF) camera is a range imaging camera system which emits light pulses, i.e. laser beam, toward the target and captures the partially reflected signal pulses [11]. By measuring the time interval between the emission and the receipt of the reflected pulses, the system can measure the distance to the target object with reference to the speed of light. Its primary advantage is that it can obtain a 3D complete scene with a single shot at the video frame rate. In addition, the accuracy of the measurement at each pixel is independent of the object surface. However it only produces a low resolution depth map such that additional super-resolution process is often required as in [12]. Besides, the obtained 3D model of a scene often contains

severe artifacts due to light scattering and interferences. Hence this approach is not suitable for measuring the 3D model of complex scene. Figure 1-1 shows some examples of commercial ToF cameras and the principle of ToF phase measurement method.



Figure 1-1. Mesa Imaging SR4000 (left), PMD Technologies 3D ToF Camera (the second column) , Depth Sense 325 from softkinectic (the third column) and the principle of ToF camera (right) adopted from [11]

### 1.1.2 STEREO VISION

To mimic human eyes, a stereo vision system employs a pair of cameras to capture two images from two different angles [13]. With the knowledge of the camera parameters and the captured images, the 3D coordinates of the scene can be obtained by triangulation [14]. In practice, more than two cameras are commonly employed to get accurate 3D geometric structures of a scene. Stereo vision systems have been used in various applications such as 3D building reconstruction [15], aerial survey, 3D face recognition [16], and 3D body scanning [17]. However, most passive stereo vision systems have low accuracy [16] and are computationally intensive [18]. Hence they are not suitable to real-time applications.

### 1.1.3 STRUCTURE LIGHT SYSTEM

For stereo vision systems, it can be difficult to find the corresponding points of the two images even when the epipolar constraint is taken into account. In contrast, the 3D model reconstruction of an object can be considerably alleviated by an active vision method [19]. To simplify the searching process of the corresponding points, a structure light system (SLS) employs a projector which replaces one of the two

cameras used in stereo vision systems. More specifically, the projector projects a code pattern of a particular structure so that the code points in the captured image can be easily distinguished by means of a coding strategy [19, 20]. Many coding strategies can be found in the literature. For instance, [21-24] employ a color coding technique to encode the pixels; [25] employs a binary coding method which uses two illumination levels, i.e. 0 and 1, in their code pattern; [26, 27] employ an N-ary coding method to reduce the large number of patterns used in the binary coding techniques; [28] proposes a hybrid method, i.e., color N-ary Gray code, to obtain an accurate 3D model; [29-31] employ the De Bruijn sequences which are claimed to be the best uncorrelated code; [32] employs an unstructured light pattern and [33-40] propose a periodic fringe pattern. Although these approaches may work effectively for simple objects, erroneous results will be generated when working with images of complex scene, for instance, containing multiple and occluded objects, having high noise level in dark regions and discontinuities in the code pattern. The current FPP system developed in this thesis can be considered as a particular SLS system which employs periodic fringe patterns. However, extra measures are developed in this research to improve the robustness when working in practical environment. They will be discussed in detail in the next few chapters.

Two of the most popular consumer SLS devices perhaps are the Kinect [5, 41] and XTion [42]. In these consumer systems, infrared (IR) light is employed as the light source and is projected onto the object in the form of random speckles. An IR camera will capture the speckle pattern image that is shifted due to the shape of the object. The 3D shape of the object can be inferred by triangulation between the camera and the light source. However, these devices can only be applied to perform low precision and low resolution 3D measurements. Their performance can be further

limited due to the various interferences of the working environment, such as the illumination variations, radiometric noises, etc. For example, Kinect system projects fix speckles pattern using near infra-red (NIR) laser projector and the depth information of a pixel is estimated by finding the best correlation pattern patch, typically in a 9x9 pixel window. Hence, it can give only a lower resolution depth image but faster in term of computational time as it requires minimum projected pattern and simple calculation.

#### 1.1.4 ACTIVE STEREO VISION

An active stereo vision system incorporates both the active vision and stereo vision techniques. For instance, in the active stereo vision system described in [7], a standard active vision method, phase measuring profilometry (PMP)<sup>1</sup>, is implemented but includes a pair of stereo cameras to improve the 3D measurement accuracy. Similarly, a coded structured light system with an additional stereo vision method has been reported in [43] to achieve highly accurate 3D measurement without the system calibration process. The stereo vision technique is also incorporated into the active vision system in [2] to mitigate the phase ambiguity problem during the phase unwrapping process, which is typical in most FPP systems. While the active vision system has somehow benefited from the additional information given by the stereo vision system, it also inherits its problem such as high computational complexity and higher hardware cost.

## 1.2 MOTIVATION AND OBJECTIVES

The above 3D scanning technologies have a common feature; they are contactless. It is an important feature since any contact between the scanner and the object can lead

---

<sup>1</sup> PMP is a general term for a phase based FPP method including both phase shifting profilometry (PSP) and Fourier transform profilometry (FTP) method.

to artifacts on the object surface which is unacceptable in many applications. While the systems are contactless, it means that there must be a distance between the scanning device and the object. In general, we do not want the distance to be too short, since it will limit the flexibility in the system setup. However, the longer is the distance, the higher will be the probability that the system is affected by the interference in the working environment. It is particularly the case for optical-based systems such as the stereo vision systems and the structured light systems. It is because the performance of the system can be easily affected by the ambient lighting condition and the light reflected by the object itself, which are difficult to perfectly control. In a typical optical-based 3D scanning process, the resulting images captured for 3D reconstruction can have strong reflection due to the surrounding strong global illumination. They can also have strong white Gaussian noise in the dark regions of the images. Sometimes some parts of them can be totally blocked due to the occlusion between multiple objects. And the images can also have sudden jumps in intensity due to the discontinuities, coloration and structural changes of the objects. All these will lead to severe errors in a 3D measurement process. In this thesis, we define a captured image to have a complex scene if the image contains one or more of the abovementioned problems. The study of robust 3D measurement of objects based on images with complex scenes has a high research value since it deals with the real problems in practical working environments.

In this research, we confine our study to one of the SLS methods, i.e. the fringe projection profilometry (FPP). As mentioned above, the FPP has salient advantages of low cost, high resolution, fast data acquisition, and full-field measurement over the existing optical 3D scanning techniques. We focus on developing robust FPP methods that can maintain the accuracy when working on images with complex

scenes. We are particularly interested in tackling the following problems in the captured images: (i) high noise level in the dark regions of the image; (ii) bias in the image due to the coloration of the object; (iii) reflection due to strong global illumination; (iv) sudden intensity change due to the discontinuities or sharp structural changes of the object; and (v) occlusion due to multiple objects. These problems are typical in real working environments.

To summarize, the general objective of this research is to develop robust FPP methods that can function effectively in adverse working environments. It is achieved by the following two strategies:

- Develop efficient and effective methods to enhance the captured images which are affected by the interference in the working environment.
- Develop good projection methods so that the projection patterns can be robustly detected despite of the possible artifacts in the captured images introduced by the working environment.

### 1.3 THESIS STRUCTURE

This thesis consists of six chapters. Chapter 1 provides an overview of some related 3D measurement techniques and outlines the motivation and objectives of this research.

Chapter 2 presents the principle of different FPP methods and their problems in real working environments. We also describe a dual-tree complex wavelet transform FPP framework which our research team developed recently for tackling the noise and bias problems in the captured images.

Chapter 3 presents the proposed inpainting algorithm for the captured images using geometrically guided iterative regularization method. The new algorithm solves the reflection problem introduced by surrounding global illuminations. It shows our first effort of tackling the problems in FPP due to the imperfect working environment.

In Chapter 4, a novel marker encoding and detection algorithm is proposed to solve the ambiguity problem in FPP. Traditional FPP procedures have the ambiguity problem since the phase information evaluated from the captured images is always confined to  $-\pi$  to  $\pi$ . Such ambiguity problem will be amplified if the captured images have noises, bias, discontinuities and other artifacts. The algorithm embeds a set of special markers into the fringe pattern to help determining the true phase information.

The markers used in Chapter 4 encode the true phase information based on their positions in the fringe pattern. A natural question arises if there is other form of encoding method that can give an even better performance in terms of robustness. We thus propose another algorithm in Chapter 5. The new algorithm embeds a set of textural code patterns into the fringe pattern. It encodes the true phase information based on the morphological structure of the textural code patterns. For decoding the code patterns, different sparse coding and sparse dictionary learning techniques are adopted.

Based on the results in Chapter 3 to 5, we draw the conclusions in Chapter 6. Future works for this research are also outlined in that Chapter.

# CHAPTER 2

## FRINGE PATTERN PROJECTION PROFILOMETRY

A fringe projection profilometry (FPP) system projects fringe patterns to an object and captures the deformed patterns caused by the object height distribution. By analyzing the displacement of the fringes, the 3D model of the object can be measured. Although there are many techniques available for FPP, many of them in fact do not function properly in practice. It is because the assumptions made by these approaches often cannot be fulfilled in practical working environments. This chapter first reviews the principle of FPP methods. Then the common problems when the conventional FPP is applied in the real working environment are described.

This chapter is organized as follows: Section 2.1 presents the principle of the FPP method; Section 2.1.1 describes the two fringe analysis methods namely, the Fourier transform profilometry (FTP) method and the phase shifting profilometry (PSP) method respectively; Section 2.1.2 reviews the principle of the phase unwrapping process for FPP. Section 2.2 presents three common problems of FPP methods in real world applications. And finally Section 2.3 describes the dual-tree complex wavelet transform (DTCWT) FPP framework and the specific problems which are tackled in this research.

## 2.1 PRINCIPLE OF FPP METHODS

In this section, we first review the principle of the conventional FPP methods [44].

An FPP system is typically set up based on the crossed-optical-axes geometry as shown in Figure 2-1 [44].

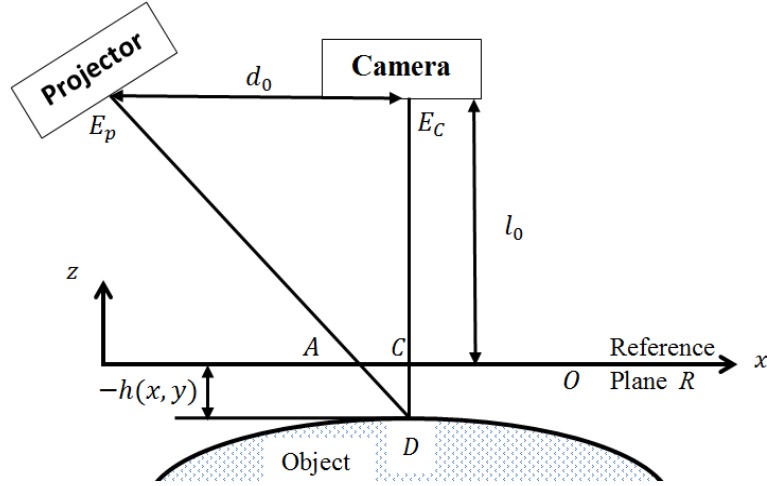


Figure 2-1 Phase based fringe projection profilometry arrangement in the crossed-optical-axes geometry.

As shown in Figure 2-1, a fringe pattern image is projected by the projector located at  $E_p$  and the deformed fringe pattern as shown on the object surface is captured by the camera at  $E_c$ . The resulting image can be modeled using the following equation [45],

$$G(x, y) = a(x, y) + b(x, y) \cos[\phi(x, y)] \quad (2-1)$$

where  $a(x, y)$  is the bias caused by the object's texture and color;  $b(x, y)$  is the amplitude of the fringe pattern which is model as a sinusoidal function. In (2-1),  $\phi(x, y) = 2\pi f_0 x + \phi_\delta(x, y)$  is the phase angle at pixel position  $(x, y)$  of the fringe image, where  $f_0$  is the carrier frequency of the fringe; and  $\phi_\delta(x, y)$  is the phase difference from the reference. Its value is related to the height of the object. It can be explained as follows. First, assume that there is a reference plan R placed as in Figure 2-1. The fringe projected onto R at point A will be seen by the camera to be at

point  $D$  on the object. The amount of displacement in  $x$ -axis is given by  $AC$ , which is related to the object height at point  $D$ , i.e.  $-h_D$ , by,

$$\frac{AC}{-h_D} = \frac{d_0}{l_0 - h_D} \quad (2-2)$$

Hence if  $AC$  is known, the object height at point  $D$  can be evaluated by,

$$h_D = \frac{l_0 AC}{AC - d_0} \quad (2-3)$$

The next question is how to obtain  $AC$ . Assume that the fringe projected onto the reference plane  $R$  is captured by the camera as a reference image. And denote  $\phi^0(x, y) = 2\pi f_0 x$  be the phase angle of the sinusoidal fringe pattern on that reference image. Now the same fringe is projected onto the object. The resulting image captured by the camera is given in (2-1) with phase angle  $\phi(x, y)$ . To estimate  $AC$ , we just need to measure the phase difference between  $\phi(x, y)$  and  $\phi^0(x, y)$ , i.e.  $\phi_\delta(x, y)$  at point  $C$ , since it is linearly proportional to the distance  $AC$ . In general, the height profile  $h(x, y)$  of the object can be computed as follows:

$$h(x, y) = \frac{l_0 \phi_\delta(x, y)}{\phi_\delta(x, y) - d_0} \quad (2-4)$$

The evaluation of  $\phi_\delta(x, y)$  requires the true phase of  $\phi(x, y)$ . Unfortunately, it cannot be directly measured from the observed image  $G(x, y)$  in (2-1) since any integer multiple of  $2\pi$  added to  $\phi(x, y)$  will give the same  $G(x, y)$ . Or in other words, only the modulo- $2\pi$  wrapped  $\phi(x, y)$  can be obtained from  $G(x, y)$ . To obtain the true phase of  $\phi(x, y)$ , the phase unwrapping procedure needs to be applied. Then once the phase information is obtained, the 3D model of an object can be reconstructed. In the following sub-sections, the fringe analysis methods for obtaining the wrapped  $\phi(x, y)$  from the fringe image  $G(x, y)$  as well as the phase unwrapping procedure will be described in detail.

### 2.1.1 FRINGE ANALYSIS

Referring to (2-1), the objective of the fringe analysis procedure is to obtain  $\phi(x, y)$  from the fringe image  $G(x, y)$ . This seemingly simple problem becomes difficult in practice since real fringe images can deviate significantly from the mathematical model in (2-1). More specifically, real fringe images may contain higher order harmonics in addition to the  $dc$  bias and the cosine term in (2-1). Besides, these higher order harmonics as well as the  $dc$  bias can “alias” into the fundamental frequency component (i.e. the cosine term in (2-1)) that makes the estimation of  $\phi(x, y)$  erroneous. Many approaches have been devised to deal with these problems. In this subsection, two types of fringe analysis method will be reviewed, namely, the Fourier transform profilometry (FTP) and the phase shifting profilometry (PSP).

#### **FTP method**

We first focus on the FTP method which was first proposed in [44]. In FTP, the fundamental frequency spectrum is assumed to have no aliasing components from the  $dc$  bias and the higher order harmonics as in Figure 2-2. Hence it can be extracted directly in the Fourier domain such that the phase of interest which is associated with the object’s height can be estimated accurately.

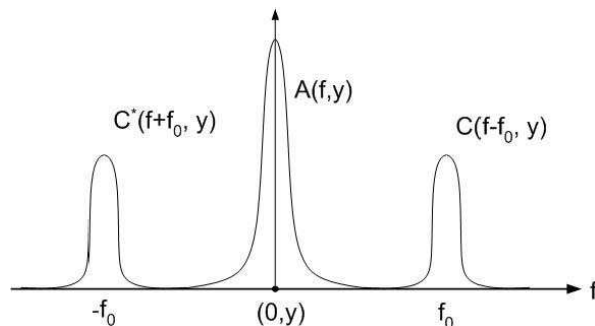


Figure 2-2. Frequency spectra of the deformed fringe pattern [44].

The above procedure can be mathematically explained as below. We first assume that the higher order harmonics are insignificant and there is no aliasing among

frequency spectra, then we can continue to use (2-1) to describe the fringe image. Suppose  $G_y(x) = G(x, y)$  for a particular  $y$ , (2-1) can be formulated by using the Euler's formula as follows [46]:

$$G_y(x) = a_y(x) + c_y(x)e^{i2\pi f_0 x} + c_y(x)e^{-i2\pi f_0 x} \quad (2-5)$$

where

$$c_y(x) = \frac{1}{2} b_y(x) e^{i\delta\phi_y(x)} \quad (2-6)$$

Taking the Fourier transform on (2-5), the following equation can be obtained,

$$\hat{G}_y(f_x) = \hat{a}_y(f_x) + \hat{c}_y(f_x - f_0) + \hat{c}_y^*(f_x + f_0) \quad (2-7)$$

where  $\hat{G}_y(f_x)$ ,  $\hat{a}_y(f_x)$ , and  $\hat{c}_y(f_x - f_0)$  are the frequency spectra of  $G_y(x)$ ,  $a_y(x)$ , and  $c_y(x)$ , respectively, as illustrated in Figure 2-2. Note that the superscript \* in (2-7) represents a complex conjugate. To estimate  $\delta\phi_y(x)$ , we just need the  $\hat{c}_y(f_x - f_0)$  term. It can be directly extracted from  $\hat{G}_y(f_x)$  assuming we know the bandwidth of  $\hat{c}_y(f_x - f_0)$ . The resulting spectra is inverse-transformed back to the spatial domain. Then, an estimation of  $c_y(x)$  is obtained. The wrapped phase difference  $\delta\hat{\phi}_y(x)$  can be extracted by computing only the imaginary part of the logarithm of  $c_y(x)$  [46],

$$\delta\hat{\phi}_y(x) = \Im[\log[c_y(x)]] = \Im\left[\log\left[\frac{1}{2} b_y(x)\right] + i\delta\hat{\phi}_y(x)\right] \quad (2-8)$$

where  $\Im$  is an operator that extracts the imaginary part of a complex number.  $\delta\hat{\phi}_y(x)$  in (2-8) is the wrapped phase difference of  $\delta\phi_y(x)$  which has a principle value  $[-\pi, \pi)$ . FTP has the advantage that, in principle, it only requires one fringe image to compute the wrapped phase difference  $\delta\hat{\phi}_y(x)$  and in turn the 3D model of the target object. However, FTP assumes there is no aliasing among frequency spectra, which is in general not the case in practice since the color pattern and the texture of the

object can introduce a *dc* bias with large bandwidth. It often introduces the aliasing problem that makes the FTP method not as popular as the other fringe analysis methods.

### **PSP method**

Unlike the FTP method which directly removes the *dc* bias and higher order harmonics in the frequency domain, the PSP method employs  $N$  phase shifted fringe patterns to remove them in the spatial domain. Again, assuming the higher order harmonics are insignificant, the  $N$  shifted fringe patterns captured by the camera can be expressed as,

$$G^n(x, y) = a(x, y) + b(x, y) \cos \left[ \phi(x, y) - \frac{2\pi n}{N} \right] \quad (2-9)$$

where  $n = 1, \dots, N$  and  $N$  is the total number of fringe patterns used. Note that (2-9) is in fact the shifted version of (2-1). The phase information  $\phi(x, y)$  can be obtained by,

$$\hat{\phi}(x, y) = \arctan \left[ \frac{\sum_{n=0}^N G^n(x, y) \sin \left( 2\pi \frac{n}{N} \right)}{\sum_{n=0}^N G^n(x, y) \cos \left( 2\pi \frac{n}{N} \right)} \right] \quad (2-10)$$

Since (2-9) has three unknown terms,  $a(x, y)$ ,  $b(x, y)$ , and  $\phi(x, y)$ , theoretically, it can be solved using only three shifted fringe patterns. Hence using three shifted fringe pattern images is popular in many PSP based fringe analysis researches [10, 33, 34, 36, 38, 39, 47-49]. The three fringe pattern images captured by the camera can be expressed as follows:

$$\begin{aligned} G^1(x, y) &= a(x, y) + b(x, y) \cos \left[ \phi(x, y) - \frac{2\pi}{3} \right] \\ G^2(x, y) &= a(x, y) + b(x, y) \cos[\phi(x, y)] \\ G^3(x, y) &= a(x, y) + b(x, y) \cos \left[ \phi(x, y) + \frac{2\pi}{3} \right] \end{aligned} \quad (2-11)$$

Since it uses three fringe patterns,  $N=3$ , the phase information in (2-10) can be reduced to [47],

$$\hat{\phi}(x, y) = \arctan \left[ \frac{\sqrt{3}(G^1(x, y) - G^3(x, y))}{2G^2(x, y) - G^1(x, y) - G^3(x, y)} \right] \quad (2-12)$$

The PSP method does not suffer from the aliasing problem due to the *dc* bias as in the FTP method. However, it requires 3 fringe images which may introduce difficulty to some real-time systems, particularly when the object is fast moving. Besides, similar to the FTP method, the PSP method can also give only the modulo- $2\pi$  wrapped phase rather than the true phase. Hence an extra phase unwrapping procedure is necessary.

### 2.1.2 PHASE UNWRAPPING PROCESS

It has been shown that both fringe analysis methods, i.e., FTP and PSP, give only a modulo- $2\pi$  wrapped phase  $\hat{\phi}$ , which has a principle value  $[-\pi, \pi)$ . Given only the wrapped phase  $\hat{\phi}$  after the fringe analysis, a phase unwrapping procedure is performed to recover the absolute (true) phase  $\phi$ . In a traditional phase unwrapping procedure, it is generally assumed that the absolute value of phase differences between neighboring pixels is less than  $\pi$ . If the assumption is valid, the solution of the absolute phase image can be easily determined. The above assumption was first reckoned by Itoh and known as the Itoh condition which can be expressed as follows [50]:

$$|\Delta\phi(x)| \leq \pi \quad (2-13)$$

where

$$\Delta\phi(x) = \phi(x) - \phi(x - 1) \quad (2-14)$$

with  $\phi(x)$  denoting the unwrapped phase at a particular location  $x$ . Note that the delta operator  $\Delta$  will hold, irrespective of the phase being an absolute or a wrapped phase. Thus the relation between the wrapped phase  $\hat{\phi}$  and the absolute phase  $\phi$  can be written as follows,

$$\Delta\phi(x) = \mathcal{W}(\Delta\hat{\phi}(x)) \quad (2-15)$$

where

$$\mathcal{W}(t) = \langle t + \pi \rangle_{2\pi} - \pi \quad (2-16)$$

is the wrapping operator which gives  $\Delta_y(x) \rightarrow [-\pi, \pi)$  and  $\langle a \rangle_b$  denotes  $a$  modulo  $b$ .

Using (2-14), the absolute phase at position  $x'$  can be recovered by,

$$\phi(x') = \sum_{x=1}^{x=x'} \Delta\phi(x) + \phi(0) \quad (2-17)$$

By substituting (2-15) into (2-17), the absolute phase  $\phi(x')$  can be obtained from the wrapped phase  $\hat{\phi}$  as follows:

$$\phi(x') = \sum_{x=1}^{x=x'} \mathcal{W}(\Delta\hat{\phi}(x)) + \phi(0) \quad (2-18)$$

After the true phase is obtained, the 3D model of the object can be readily reconstructed.

In the last two decades, there have been many phase unwrapping algorithms developed based on the Itoh assumption [51]. One of the classic algorithms is Goldstein's branch cut algorithm [52]. In this algorithm, the nearby residues<sup>2</sup> are first detected and then connected by branch cuts<sup>3</sup> so that the residues are balanced and the phase can be unwrapped along any path that does not cross the branch cuts. This

---

<sup>2</sup> A residue is an inconsistent pixel which is located somewhere inside a "loop" of four pixels whose integration of the phase derivative, i.e., the sum of the wrapped phase differences, is not zero, but  $2\pi$ (positive charge) or  $-2\pi$  (negative charge).

<sup>3</sup> A branch cut is a line that connects two residues with difference polarities; the phase cannot be unwrapped crossing this line.

algorithm is simple and fast. Another classic algorithm is the quality-guided phase unwrapping algorithm [51]. It is in fact a floodfill algorithm in which the order of fill is determined by a quality map<sup>4</sup> which was first introduced by Bone [53]. Since then, there have been many phase quality guided unwrapping algorithms developed [37, 54-57]. Besides, the phase unwrapping procedure can also be performed by separating the phase image into regions by means of the fringe lines and adding a multiple of  $2\pi$  to each region such that the discontinuities are minimized. This approach was proposed in [58] which employs an edge detection technique to find the boundary of regions. An improved version of this approach was later introduced by Flynn [59] and was used to unwrap the interferometric phase. This approach is robust but is also computationally expensive. Although there are many robust phase unwrapping algorithms, they often cannot give accurate results since the assumption of the Itoh condition made by these algorithms is not valid in many practical working environments, which is the topic for discussion in the next section.

## 2.2 FPP IN THE REAL WORKING ENVIRONMENT

When a camera captures the projected fringe pattern on the scene, the light intensity as shown in each pixel in the captured image can be viewed of composing by two components, namely, the direct light and the indirect light. The direct light is generated by the direct illumination of the fringe pattern projected by the projector. The indirect light is the global illumination from the scattering of light of other parts in the scene. In addition to those two components, a fringe image can also contain bias and noise. As mentioned above, the bias is caused by the object' texture and

---

<sup>4</sup> A quality map is a quality or goodness of phase values to guide the unwrapping path, i.e. the second difference, phase derivative variance, maximum phase gradient, etc.

coloration which reflect only some of the direct light; whereas noise is caused by the different noise sources, such as, electronic noise of the CCD, camera lens, air, etc.

In real working environments, shadows are also commonly exist when the scene consists of multiple objects. In such situation, the light from the projector can be blocked due to the objects' shape. The captured fringe image may thus contain regions with low intensity pixels known as shadows. Hence the phase value in this region cannot be inferred. And in some extreme situations, even some parts of the object cannot be seen in the image due to occlusion. In this situation, the conventional phase unwrapping algorithm will fail to recover the true phase since the continuity of the phase cannot be guaranteed. In the following subsections, some traditional methods in FPP that deal with the noise and bias problem, the global illumination problem, and the ambiguity problem are reviewed.

### 2.2.1 NOISE AND BIAS PROBLEM

The noise and bias problem in FPP has been analyzed for nearly three decades [44, 60-63]. For the FTP method, the noise and bias problem is particularly crucial to the fringe analysis process since the incurred aliasing effect cannot be simply removed in the frequency domain. The noise problem can be relatively easier to resolve. In [60-63], a short time Fourier transform is employed to deal with the non-stationary fringes and noise. One of the limitations of this approach is that the width of the window needs to be determined. Besides, it is also computationally expensive. Alternatively, the wavelet transform can be used to detect the phase and at the same time remove noise as in [64-68]. All these approaches are however computationally expensive and cannot handle the bias problem.

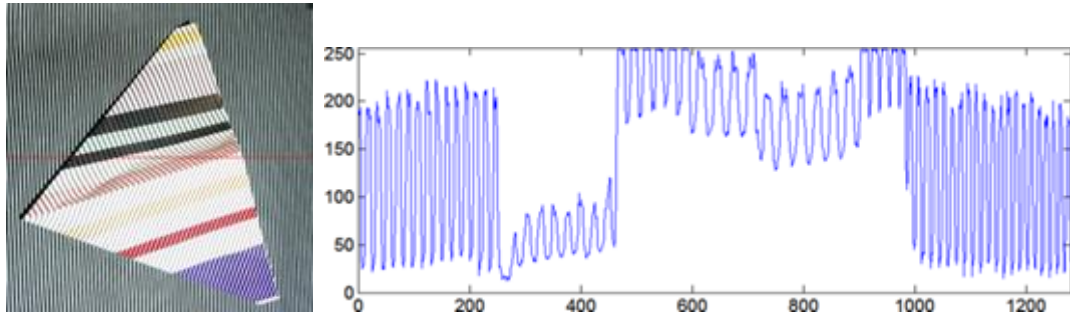


Figure 2-3 the fringe pattern with bias (left) and the intensity plot at row indicated by red line (right)

The bias problem occurs usually when the target object contains textures and/or color patterns of large luminance differences. In this case, the resulting bias will have a large bandwidth and lead to spectral leakage. An example is shown in Figure 2-3. In the figure, the paper aeroplane has a few color strips such that sharp changes in luminance are found on the strip boundaries. In this case, conventional FTP methods which try to remove the bias in the frequency domain will not be effective. The 3D model reconstructed from the resulting fringe image will thus contain severe artifacts. Different approaches were developed to solve the problem. In [46], an additional background image is captured to remove the bias prior to the fringe analysis process. This approach is simple but requires additional image, which may cause problem if the object is moving rapidly. In [67], a bias removal method is successfully integrated into the dual-tree complex wavelet transform (DTCWT) based FTP system [69]. By adopting the special feature of the fringe image in DTCWT domain, the bias in the fringe image can be much easily detected and removed. In fact, some of the works in this research were also carried out based on this system. More details of this system will be given in a later section of this Chapter.

As it is mentioned above that using more fringe images can help to remove the bias, the PSP method which inherently uses multiple fringe images for fringe analysis has been shown to be able to mitigate the noise and bias problem easily. It is resistant to

the ambient light and the reflection due to the cancelation effect from several shifted fringe images. As it is mentioned in Section 2.1.1, the PSP method needs a minimum of three phase shifted fringe images. Then the bias component can be removed by averaging the three images [2, 17, 70].

While using more fringe images can improve the performance in removing noise and bias, it can also introduce problem to applications with moving objects as mentioned above. To minimize the number of fringe patterns without sacrificing the accuracy of the measurement, [6, 70, 71] propose a two plus phase shifting algorithm which requires only two fringe patterns and one flat image. In [6], a two-step method is employed to obtain an accurate 3D measurement of soldering paste on a printed circuit board; whereas in [70, 71], a two-step method is employed to speed up the process particularly in dealing with motion which commonly presents during the capturing process.

To further improve the accuracy of the PSP method, a pre-filtering stage has also been introduced [6, 7, 72]. In [6], an additional median filter is incorporated to obtain an accurate 3D measurement of the tiny solder paste on a printed circuit board. In [7], a stereo camera with additional Kullback-Leibler divergence refinement is used to enhance the final 3D reconstruction of a complex scene; and in [72], the FTP method is applied to each phase shifted fringe pattern to further improve the accuracy of the phase measurement. Although all the abovementioned approaches can effectively reduce the effect of the noise and bias problem, they will still fail to reconstruct the 3D model of objects if the fringe images have a complex scene, for instance, containing multiple objects and/or with strong global illumination. It will be discussed in the following sections.

### 2.2.2 GLOBAL ILLUMINATION

In FPP, it is expected that the camera will capture only the direct light emitted from the projector. However in practice, it is unavoidable for the camera to be affected by the illumination generated by other light sources in the scene. It is known as the “global illumination”. Figure 2-4 shows a camera that captures light from both the direct illumination from the projector and the global illumination from various indirect light sources such as: (B) inter-reflections, (C) subsurface scattering, (D) volumetric scattering, and (E) translucency [73].

In the presence of global illumination, the phase measured from the fringe analysis process is unlikely to be accurate. It introduces additional bias to the fringe image. And in some extreme cases that the global illumination is strong and the material of the object is reflective, specular highlights are formed on the object surface and the fringes in the highlight regions can be totally washed out [74]. Hence the continuity of the fringes cannot be preserved and introduces much difficulty to phase unwrapping. To minimize the global illumination effects, some FPP methods employ high frequency fringe patterns [9, 10, 75-77]. However all of these approaches require more than the theoretical three fringe patterns of PSP. Alternatively, additional hardware systems are employed to the PSP method such as sliding projector [78], polarizer [10], special coaxial optical scanner [76], laser scanner [8], and additional camera [7]. Obviously they introduce additional cost and complicate the system setup. In fact, the approach in [10] still requires more than the minimum three fringe images and is designed specifically for reconstructing the 3D model of translucent objects.

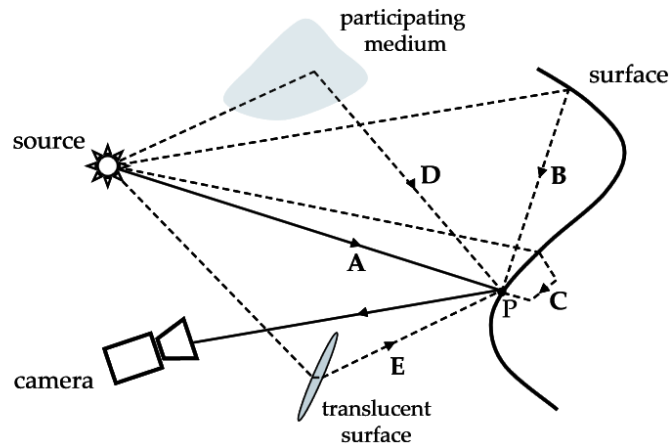


Figure 2-4 Illustration of direct illumination and global illumination from other light sources in the scene [73].

### 2.2.3 AMBIGUITY PROBLEM

All FPP systems which employ periodic fringe patterns, i.e., the FTP and PSP method, will suffer from the so-called ambiguity problem that only the wrapped phase information is retrieved. Phase unwrapping algorithms are thus adopted to help resolving the ambiguity problem. Most phase unwrapping algorithms are based on the Itoh condition [50] as mentioned in Section 2.1.2. To obtain the true phase, it is shown in (2-18) that a pre-defined reference point  $\phi(0)$  is needed. To obtain this reference point, an additional tiny marker is commonly used to put on the surface of the object, for instance, PSP with a dot marker [38], PSP with a strip marker [79], and FTP with a cross marker [46], etc. These approaches, although simple, suffer from a few difficulties in practice. First, some of these approaches are invasive (that require a real marker putting on the object surface) or require human effort (manually marking on the fringe images). Second, for complex scenes that contain multiple objects, one marker is required for each object in the scene. Finally, if there is discontinuity in the fringe image, a marker is needed for each disconnected region.

The last problem is particularly difficult to solve since the number and position of the disconnected regions are usually unknown during the system setup.

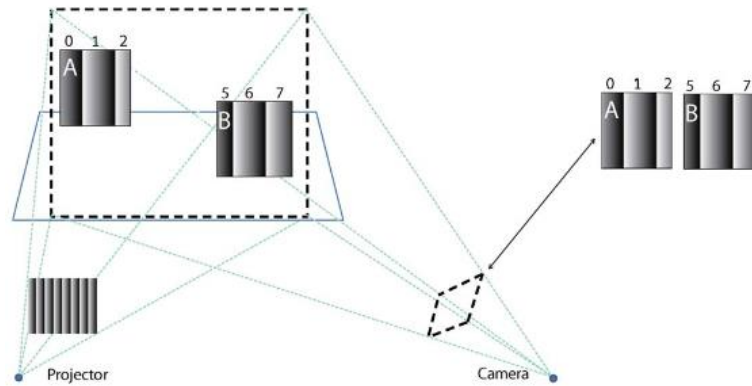


Figure 2-5 Illustration of the ambiguity problem due to isolated multiple objects [36].

To illustrate the above, Figure 2-5 shows a scene consisting of two objects positioned at different distance from the camera. As shown in the figure, the distance of the two fringes becomes closer in the fringe image although the period order (the number in the figure) is significantly different. So the fringes are discontinuous and each object needs to have its own marker (or reference point). To simplify the need of putting markers on the objects, several pattern codification strategies have been proposed to solve the ambiguity problem by embedding the period order information (the number above the fringes in Figure 2-5) into the fringe pattern in the form of, e.g. multi-wavelength [80], random speckles [39], multi-colors [79], dual frequencies [35, 81], and additional extra patterns or extra gray code patterns [5, 82-84]. However the approaches in [5, 82-84] need additional projections whereas the approaches in [35, 39, 79, 81] can reduce the accuracy of the final reconstructed 3D model.

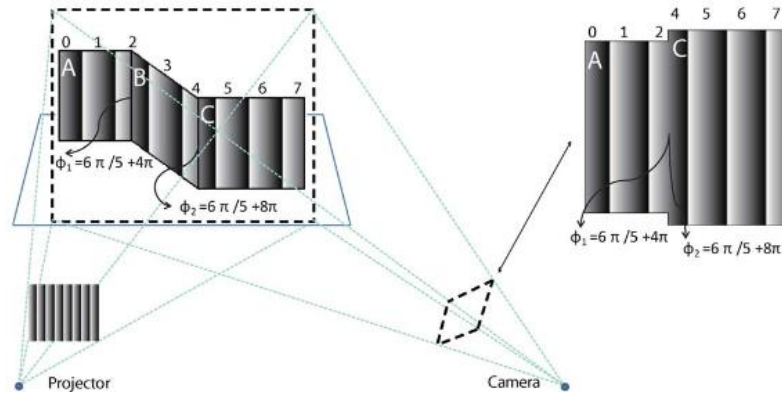


Figure 2-6 Illustration of the ambiguity problem due to occlusions [36].

Furthermore, the presence of occlusions in the scene also contributes to the severe ambiguity problem. As shown in Figure 2-6, the continuity of the fringes seems preserved but in fact the fringes in region B (period number 2-4) are missing in the camera's view (right). Any conventional phase unwrapping algorithms based on the Itoh condition will fail in recovering the true phase. To solve this problem, different period order encoding strategies have been proposed [35, 36, 39, 40, 85]. However all these approaches reduce the accuracy of the final 3D model of the objects since the additional period order information introduces noise to the fringe images and can seriously affect the accuracy of the measurement. Moreover, the approaches in [35, 36, 85] require more than the theoretical three fringe images. For example, [35] employs six fringe images for embedding the additional period order information to assist the phase unwrapping procedure whereas [36] employs at least four fringe images; and [85] proposes a phase-coding method which needs additional three coded phase-shifted images. Further research is needed to develop a truly robust FPP scheme that can get around with the various problems in practical working environments.

### 2.3 DTCWT FPP FRAMEWORK

It has been proved in [67] and [69] that the DTCWT is an effective and efficient tool for denoising and removing the bias of fringe images. This research can be considered as a continuation of our previous studies in DTCWT based FPP systems with particular emphasis on the applications in practical working environments. For this reason, let us first briefly review some background about the conventional DTCWT FPP methods.

Based on the wavelet theory, a fringe image  $G_y(x)$  in (2-1) can be synthesized based on the wavelet functions  $\psi$  and the scaling function  $\zeta$  as follows [67]:

$$G_y(x) = \sum_{n=-\infty}^{\infty} s_y(n)\zeta_y(x-n) + \sum_{j=-\infty}^{\infty} \sum_{n=-\infty}^{\infty} w_y(j,n)2^{\frac{j}{2}}\psi_y(2^jx-n) \quad (2-19)$$

where  $j$  is the scale factor. The scaling coefficients  $s_y(n)$  and the wavelet coefficients  $w_y(j,n)$  are given by,

$$s_y(n) = 2^{\frac{j}{2}} \int_{-\infty}^{\infty} G_y(x)\zeta_y(2^jx-n)dx \quad (2-20)$$

and

$$w_y(j,n) = 2^{j/2} \int_{-\infty}^{\infty} G_y(x)\psi_y(2^jx-n)dx. \quad (2-21)$$

In case the wavelet function is analytic (i.e. having zero negative frequency components) and has compact support, it has been proven in [67] that the magnitude response when applying such analytic wavelet transform to a fringe image is piecewise smooth. This feature greatly facilitates the design of denoising and bias-removal operators in the analytic wavelet domain, since such special magnitude response allows the wavelet coefficients of fringes to be more distinguishable from both noises and bias.

Due to these advantages, our research team has developed a DTCWT based FPP framework as illustrated in Figure 2-7. As shown in the figure, both the fringe denoising and bias removal operation are performed in the DTCWT domain. Once finished, the wavelet coefficients are transformed back to the spatial domain and the phase unwrapping algorithm is used to recover the absolute phase information.

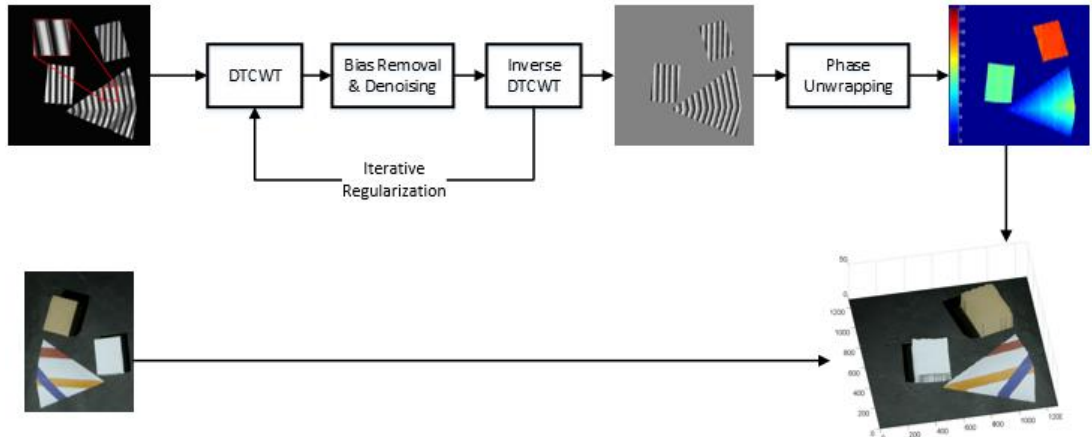


Figure 2-7. The conventional DTCWT FPP framework (adopted from [67, 69])

In our DTCWT FPP framework, the 2D-DTCWT is realized by using two pairs of 2D discrete wavelet transform (DWT) trees as illustrated in Figure 2-8. Each pair has an approximately analytic wavelet function.

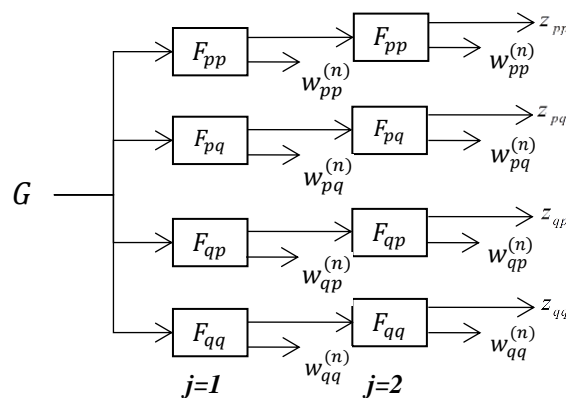


Figure 2-8. Realization of the 2D DTCWT using four DWT trees ( $J=2$ )

As shown in Figure 2-8, each level of the wavelet transform gives two sets of oriented complex wavelet coefficients  $w_{pp}^{(n)} + jw_{qq}^{(n)}$  and  $w_{pq}^{(n)} + jw_{qp}^{(n)}$  with three orientations  $n \in \{H, V, D\}$ : vertical ( $V$ ), horizontal ( $H$ ), and diagonal ( $D$ ). Thus at each level  $j$ , we have a set of  $w_j$  denoted as,

$$\begin{aligned} w_j &= \{w_j^{15^\circ}, w_j^{45^\circ}, w_j^{75^\circ}, w_j^{105^\circ}, w_j^{135^\circ}, w_j^{165^\circ}\} \\ &= \{\rho_1 e^{i\theta_1}, \dots, \rho_6 e^{i\theta_6}\} \end{aligned} \quad (2-22)$$

where  $\rho_i$  and  $\theta_i$  correspond to the six magnitudes and orientations ( $15^\circ$ ,  $45^\circ$ ,  $75^\circ$ ,  $105^\circ$ ,  $135^\circ$ , and  $165^\circ$ ), respectively, of the wavelet coefficients. Meanwhile, at the coarse level  $J$  we have the oriented scaling coefficients which have two components:

$$z_1 = z_{pp} + jz_{qq} \quad z_2 = z_{pq} + jz_{qp} \quad (2-23)$$

Although the original DTCWT based FPP method is efficient in handling noise and bias, further work is needed to improve its robustness when dealing with the global illumination and ambiguity problems as mentioned in Sections 2.2.2 and 2.2.3. To tackle these problems, we improve the original DTCWT based FPP framework by introducing *the geometrically guided iterative regularization* block and *the period order detection and estimation* block as shown in Figure 2-9.

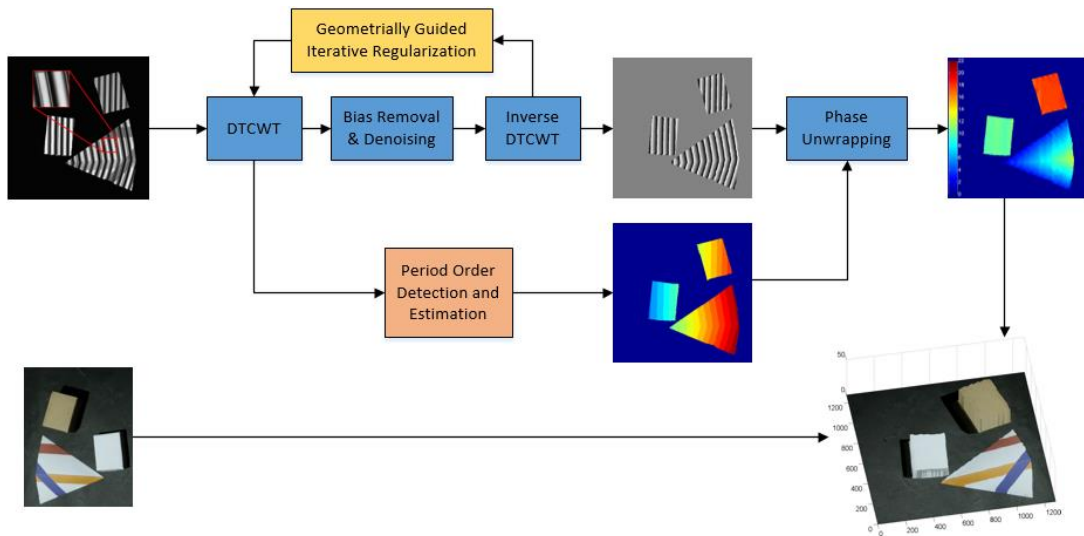


Figure 2-9. Enhanced DTCWT based FPP Framework

The new functional blocks of enhanced DTCWT based FPP framework can be summarized as follows:

1. *Geometrically Guided Iterative Regularization* block. As shown in the figure, this block is in fact the original iterative regularization with additional automatic highlight detection and geometric structure initialization functionalities. It targets at recovering the missing fringes, if any, due to the global illumination problem. More specifically, the block first detects automatically the location of the regions with missing fringes. Then the geometric structure of the fringes in these regions is estimated to give a good initialization for an iterative inpainting process to regenerate the missing fringes. The operation of this new function block will be further explained in Chapter 3.
2. *Period Order Detection and Estimation* block. In the enhanced framework, we employ a new strategy that embeds the period order information into the fringe pattern. Two approaches are proposed in this research. The first approach employs a marker encoded fringe pattern, which has the period order number encoded based on the relative position of the markers and the fringes. Then using the DTCWT, the marker cue information can be extracted from the fringe image and is used to estimate the period order information. In the second approach, the period order information is encoded based on the shape of some textural patterns and embedded to the fringe patterns. On the decoder side, the morphological component analysis (MCA) is used to separate the textural pattern and the original fringe pattern. Then a sparse dictionary is learned and used to identify the textural pattern and estimate the period order number of the fringes. They are used to facilitate the phase

unwrapping procedure to obtain the true phase. The operation of this new function block will be further explained in Chapter 5.

# CHAPTER 3

## INPAINTING FRINGE PATTERN USING GEOMETRICALLY GUIDED ITERATIVE REGULARIZATION

Fringe projection profilometry (FPP) is well known as a phase imaging system that can obtain the 3-dimensional (3D) model of objects accurately and efficiently. As successful as it has been proved on simple objects, FPP with a single fringe image produces less satisfactory results when measuring an object if the captured fringe image is distorted by strong global illumination such as highlights. As mentioned in Chapter 2, it is due to the mistaken assumption made by the traditional FPP systems that all the light captured by the camera is from the projector. Due to the strong global illumination, some of the fringes might be washed out by the highlights and the resulting 3D model reconstructed will be distorted in the affected regions. In this chapter, we propose a sparse representation based iterative regularization inpainting algorithm to regenerate the missing fringes washed out by the highlights. The algorithm can detect the affected regions automatically and inpaint the missing fringes accurately. The proposed algorithm greatly improves the measurement result compared with the conventional FPP methods when working in an environment with strong global illumination.

This chapter is organized as follows. Section 3.1 presents a brief review on some recent related research works. Section 3.2 introduces the general framework of the proposed sparse representation based iterative inpainting regularization using the 2D-DTCWT. Section 3.3 presents the highlight detection algorithm using the 2D-DTCWT. Section 3.4 presents the geometric sketching algorithm for guiding the inpainting process. Section 3.5 shows the simulation and experimental results. Section 3.6 summaries this chapter. The content of this chapter is extracted from our paper published in *IEEE Transactions on Image Processing* [86].

### 3.1 RELATED WORKS

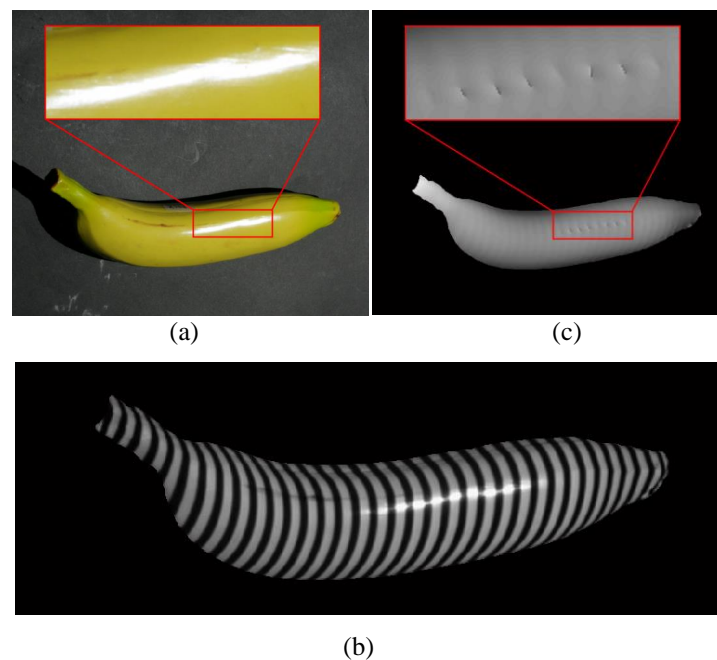


Figure 3-1 (a) The texture image of a plastic banana; (b) the fringe image captured using an FPP system; and (c) the 3D model (depth map) evaluated from the fringe image in (b).

In the last decade, significant achievements in the area of FPP have been reported. By using FPP, real time 3D measurements [33, 36] and highly accurate 3D scanning [5, 7] can be achieved. However, it is necessary to point out that all existing FPP

techniques assume the deformed fringe pattern is available for all parts of the object. It is indeed not true particularly when the target object is made of materials with high reflectivity of light, such as metal, porcelain or even plastic, etc. The fringe image captured by the camera is often affected by nearby strong light sources that some parts of the fringe image are masked by the reflected light. They form the so-called “highlight” regions on the fringe image. They corrupt the fringe pattern and thus affect the 3D model measurement result. Figure 3-1 (a) and (b) show an example of the highlight in a fringe image. The measured 3D model is distorted in the highlight region as shown in Figure 3-1(c).

In the presence of highlights, 3D scanning based on FPP is a challenging task and has been an active research area recently. One solution is to capture several fringe images from various viewpoints either by using an active stereo technique [76], a moving camera or a moving scene [87], a sliding projector [78], or polarization filters [10, 88], etc. Although these techniques are effective to remove the highlights, they require additional hardware and complicated calibration procedures in the hardware setup. Another approach is by using multiple fringe images of different fringe patterns. For instance, the methods in [9, 10, 48, 73, 77, 89] employ the phase shifting method with high frequency patterns for 3D reconstruction of translucent objects. The methods in [9] and [5] employ special discrete fringe patterns to mitigate both the indirect illumination problem and subsurface scattering. These techniques are more cost efficient than the special hardware solutions but they suffer from the drawback of requiring many fringe images taken in sequence. It thus further limits their application to only absolutely static objects. These approaches are also computationally expensive. Based on the spatial method, [89] employs an unstructured light pattern that is specifically designed to reduce the global

illumination. Although this method requires only a single pattern, the resulting 3D model can only have low resolution and the method is also computationally expensive.

Indeed for general texture images, there have been many works on recovering the missing texture of the image due to the highlights [90-95]. The method in [95] requires a spectral image and thus a special camera is required. The methods in [91-94] are based on Shafer's dichromatic reflection model [96] that works only on RGB images. These approaches are thus inapplicable to FPP since a fringe image is a gray scale image that contains non-stationary sinusoids.

There are some other approaches which are based on the inpainting technique [90, 97]. The method in [90] requires the illumination information for guiding the inpainting procedure and the method in [97] requires two images captured with different exposure times based on the color line projection techniques. Compared to the conventional methods, these approaches provide better result in recovering the surface texture and shading intensities. In particular, [90] requires only a single image that makes it applicable to dynamic scenes. However, the illumination information of these approaches is again obtained based on the chromaticity analysis of RGB images and is thus not suitable to the fringe images used in FPP.

For FPP, various fringe enhancement techniques have been developed to improve the quality of the fringe images [54, 67, 69, 98-101]. For instance, the methods in [98-100] extrapolate the missing fringes at the border of the measured fringe patterns by applying a specifically designed filter in the Fourier domain. The methods in [67, 69] employ an iterative regularization method based on a complex wavelet analysis to enhance the fringe pattern distorted by bias and noise. However all of these fringe

enhancement approaches cannot regenerate the missing fringes due to the highlights since they do not consider the continuity of the structure within the measured fringe pattern. Besides, the approaches in [98-100] work only when the spatial variations, i.e., object's color, texture, are minimum. Meanwhile, the exemplar based inpainting approach [102] is employed to fill the missing area of the coded fringe image [101] or the wrapped phase map [99]. However, it will generate additional residues in the measured fringe pattern.

In this chapter, we introduce a novel inpainting algorithm for the restoration of the fringe patterns due to the highlights in the fringe image. Different from the previous approaches, the proposed algorithm does not require special hardware and works only on a single fringe image. The new algorithm first detects the highlight regions of a fringe image based on a Gaussian mixture model. Then a sparse representation based image inpainting method similar to [103-107] is applied to recover the corrupted fringe patterns. Unlike the conventional inpainting methods such as [103-107] which assume no information about the highlight regions, the proposed algorithm first detects the missing fringe area and estimates the geometrical structure of the fringe patterns in order to guide the iterative inpainting procedure. The restored fringe image is then used in the conventional FPP to measure the 3D model of the object.

### 3.2 SPARSE REPRESENTATION BASED INPAINTING

Due to the presence of highlights, the total radiance measured at the camera sensor consists of both the direct and global illuminations as follows:

$$G(x, y) = \begin{cases} G^d(x, y) & (x, y) \in R \setminus \Omega \\ G^g(x, y) & (x, y) \in \Omega \end{cases} \quad (3-1)$$

where  $G(x, y)$  is the captured fringe image;  $G^g(x, y)$  is the degradation of the original fringe image caused by the highlight in  $(x, y) \in \Omega$  as shown in Figure 3-2; and  $G^d(x, y)$  is the unaffected region.

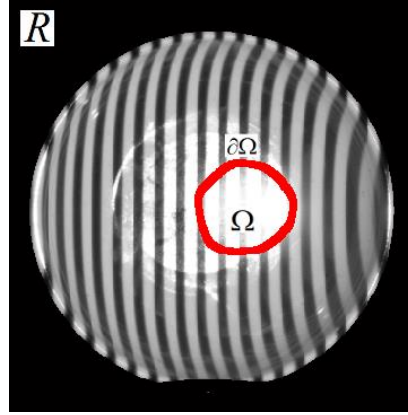


Figure 3-2 A fringe pattern with highlight. The entire fringe image is denoted by  $R$ ; the highlight region and its contour are denoted by  $\Omega$  and  $\partial\Omega$ , respectively.

The problem can be viewed as a classical inpainting problem such that the original fringe image in the highlight region  $\Omega$  can be estimated by minimizing the following cost function [105],

$$\min_{G, w} \frac{1}{2} \|P(G - F)\|_2^2 + \frac{\lambda}{2} \|\Psi w\|_p \quad (3-2)$$

where  $F$  is the original image,  $\Psi \in \mathbb{R}^{M \times N}$  is the transform matrix of some operator;  $P \in \mathbb{Z}^{M \times N}$  is a diagonal matrix with entries 1 in  $R \setminus \Omega$  and 0 otherwise;  $\lambda$  is a penalizing factor;  $w$  is transform coefficients, and  $\|\cdot\|_p$  denotes the  $\ell_p$  norm. Given a  $\ell_1$  norm using a tight frame transform  $\Psi$ , such as DCT [103, 108], wavelet [109], curvelet [110], framelet [107], i.e.,  $\Psi^T \Psi = I$ , a close form solution for (3-2) can be obtained as follows:

$$G^{(t+1)} = PF + (I - P)\Psi^*S_\lambda(\Psi G^{(t)}) \quad (3-3)$$

where

$$S_\lambda(a) = \text{sgn}(a)\max(|a| - \lambda, 0) \quad (3-4)$$

is the soft thresholding operator [111]. For the selection of  $\Psi$ , we adopt the 2D-DTCWT [112]. It is based on the fact that the 2D-DTCWT has nearly shift-invariant and minimum aliasing properties. They allow the fringe image to be sparsely represented by only one or two levels of wavelet coefficients. Besides, it is shown in [67] that the magnitude response of the 2D-DTCWT of a fringe image is piecewise smooth. It enables different efficient denoising and bias removal algorithms [67, 69, 113]. In fact, as mentioned in Chapter 2, the proposed inpainting algorithm is included in one of the subsystems of the 2D-DTCWT based FPP framework described in [67].

Although the abovementioned inpainting strategy is effective, its general application is hindered by the following two problems:

1. As shown in (3-2), the mask  $P$  needs to be known in order to implement the equation. It means that the highlight region  $\Omega$  needs to be determined prior to the inpainting procedure.
2. For most iterative minimization algorithms, a good initial guess can significantly reduce the number of iterations and ensure the iterations to converge to the global minimum. Unlike normal texture images, fringe images are highly structural. They are formed by stripes with orientation following the 3D shape of the object. Any initial guess of the corrupted fringe pattern should have a stripe-like structure with orientation close to the original fringe pattern or it is highly unlikely the iterative process can converge to such structural pattern.

In order to estimate the missing fringe pattern due to the highlights, the proposed algorithm is performed in three stages: *highlight region detection*, *geometric sketching of fringe pattern* and *inpainting with sparse regularization*. In the highlight region detection phase, we analyze the histogram of the fringe image using a Gaussian mixture model so that a threshold is determined to identify the highlight pixels in the image. Thus the matrix  $P$  in (3-2) is obtained. The details are shown in next section. In the second phase, the geometric structure of the fringe pattern is estimated and forms the initial guess of the iterative inpainting process. The procedure is explained in Section 3.4. Lastly, the inpainting based on the iterative regularization method in (3-2) is performed using the 2D-DTCWT, as described earlier in this section.

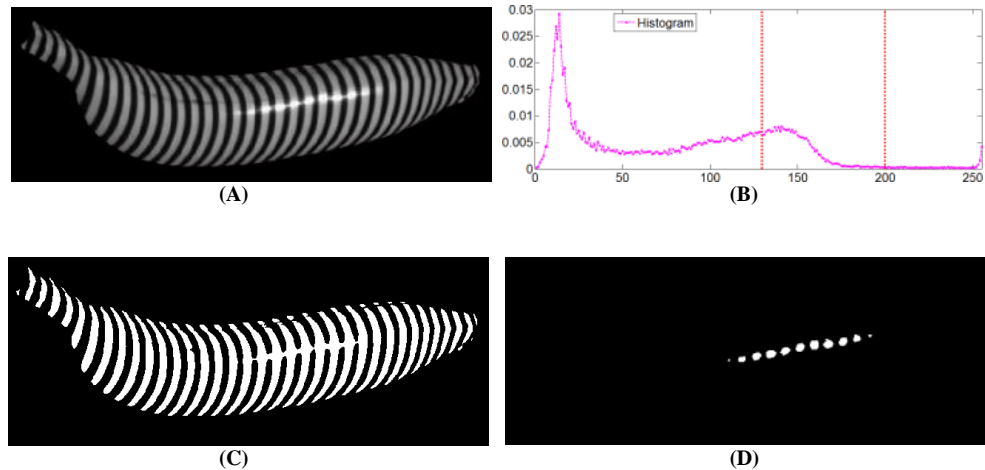


Figure 3-3 (a) The fringe image of a plastic banana; (b) histogram of the fringe pattern, dash lines are the threshold obtained by the Otsu method [114] (left) and the minimum error method [115] (right); (c) the result using the Otsu method; and (d) the result of the minimum error method.

### 3.3 HIGHLIGHT DETECTION

Although the highlights have a rather distinctive appearance in a fringe image, automatically locating them is not as straightforward as it seems to be. Standard operators such as the Otsu method [1] or the minimum error thresholding method [2]

make use of the intensity information of the image to form a histogram for determining a threshold. Then image pixels having intensity higher than the threshold will be considered as the highlight. However, difficulty arises when applying these standard approaches to fringe images. Since a fringe image is formed by dark and bright stripes, they have a sharp contrast similar to the effect of the highlights. They influence the standard approaches when determining the threshold value. An example is shown in Figure 3-3. It can be seen that the resulting detected regions of the Otsu method are the bright regions of the whole image; and the ones detected by the minimum error method are the bright regions within the highlight. The problem is further complicated if the texture of the object also contains sharp contrast in intensity.

In the next subsections, two approaches based on the 2D-DTCWT will be introduced in detail. In the first approach, the 2D-DTCWT coefficients of the fringe image are used to determine the highlight regions directly and the threshold is estimated based on the statistic information, i.e. means and variance, of the coefficients. To improve the accuracy of the detection, the fringe pattern is first smoothed in the 2D-DTCWT domain and the threshold is estimated using a Gaussian mixture model (GMM).

### 3.3.1 HIGHLIGHT DETECTION USING INTERPOLATED 2D-DTCWT COEFFICIENTS

To facilitate the inpainting process, we first detect the highlight regions in the captured fringe image. Traditional methods to detect a highlight area in an image is often based on the chromaticity of the color image, such as [91, 93]. However, these approaches cannot be applied to our problem since they work only on color RGB images rather than fringe images. In our study, it is observed that the highlights in a fringe image can be characterized by structures with low frequency information but high intensity value. Hence they can be detected by a simple thresholding operation

applied to the magnitude response of their coarse level DTCWT coefficients. To achieve this, we first extract the coarse level DTCWT coefficients of the fringe image and compute their magnitude response. Then we use an interpolation function  $\mathcal{F}(\cdot)$  to expand their size to be the same as the original image. Based on the nearly shift invariant property of the DTCWT, it is safe to assume that the highlight regions detected in the DTCWT domain should be very close to those in the spatial domain. To facilitate the thresholding operation, we take the product of the magnitude of the two coarse level subbands before performing the interpolation as follows:

$$H^g = \mathcal{F}(|z_1| \times |z_2|) \quad (3-5)$$

where  $|z_1|$  and  $|z_2|$  are the magnitudes of the wavelet coefficients at the coarsest scale defined in (2-23) and the highlight region is determined by,

$$\bar{\mathcal{P}} = \begin{cases} 1 & \text{if } H^g > \lambda_{Hg} \\ 0 & \text{otherwise} \end{cases} \quad (3-6)$$

where  $\bar{\mathcal{P}}$  denotes the domain of the highlight regions; and  $\lambda_{Hg}$  is the threshold value. As it is mentioned in Chapter 2, the 2D-DTCWT magnitude response of a fringe image is piecewise smooth. Hence,  $H$  is smooth and has a low variance value in the absence of highlights. If it is assumed that the total area of highlights is only a small part of the fringe image, the mean and the standard deviation of  $H$  are approximately equal to the average value and the standard variation of the direct light (defined as  $\mu_{L^d}$  and  $\sigma_{L^d}$  respectively). Here we assume that the global illumination has a far lower value than the direct light. In this case, the threshold value can be determined by,

$$\lambda_{Hg} = \mu_{L^d} + 2\sigma_{L^d} + \varepsilon \quad (3-7)$$

where  $\varepsilon$  is a small constant to determine the sensitivity to the highlights. In our experiment  $\varepsilon$  is set to be zero. Figures 3-4 (a) and 3-4 (b) show the fringe pattern and the texture image of a ceramic plate respectively. It can be seen that due to the global illumination and the material of the object, a specular highlight region is found at the

upper right part of the ceramic plate. By using the approach as mentioned above, the magnitude response of the 2D-DTCWT of the fringe image at the coarse scale is interpolated and the result is shown in Figure 3-4 (c). It can be seen that the detected highlight region has a significantly higher magnitude than the surrounding non highlight region. Thus, as shown in Figure 3-4, the highlight region can be detected accurately using the threshold value defined in (3-7). Note that the proposed iterative regularization algorithm will fill the missing area accurately even when the detected highlight region is slightly larger than the actual missing area because the algorithm will eventually converge to the actual size of the missing area.

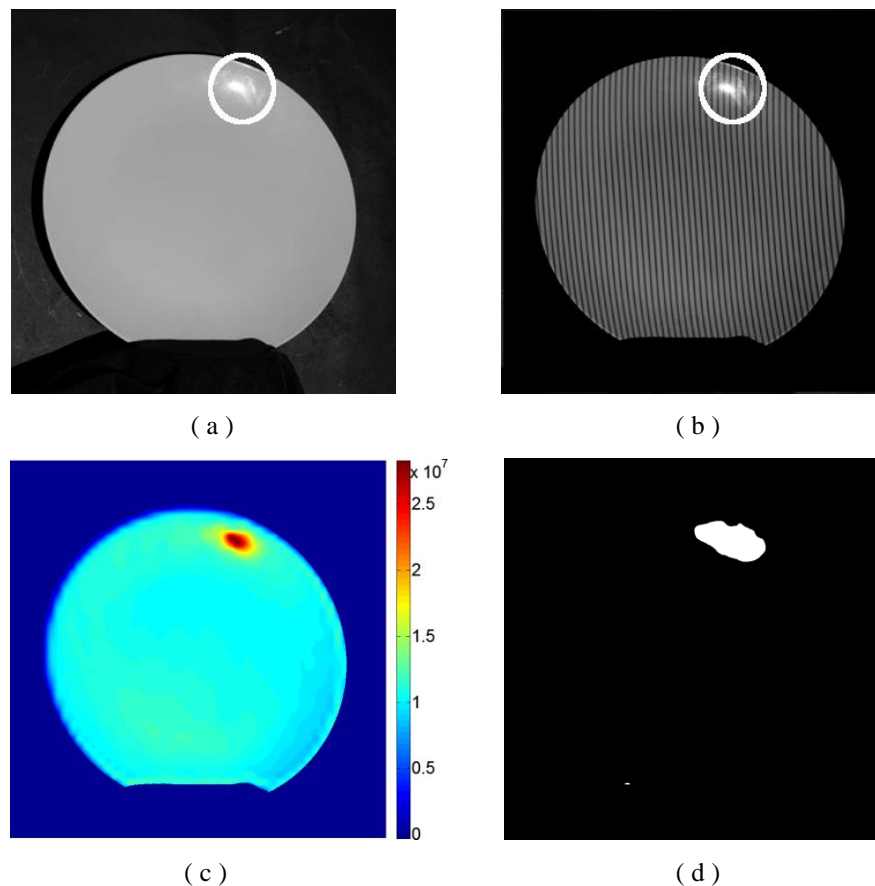


Figure 3-4 (a) The texture image of a ceramic plate with a highlight region; and (b) the fringe image of the plate with the highlight region. (c) Interpolated magnitude of complex wavelet coefficients at the coarse level; and (d) the estimated highlight region (white).

### 3.3.2 HIGHLIGHT DETECTION USING GMM SMOOTHED FRINGE IMAGE

Although the above method can estimate the highlight region with reasonably good accuracy, it will become less effective if the texture of the object contains large contrast in intensity, which can be wrongly classified as highlights. To solve this problem, we suggest to first blur the fringe image with a smoothing operator and then use a Gaussian mixture model (GMM) [116] to determine the threshold for highlight detection. More specifically, a smoothed fringe image can be obtained using a multiscale analysis based on the 2D-DTCWT as follows:

$$\hat{G} = \Psi^T \wp(\Psi G) \quad (3-8)$$

where  $\wp(\cdot)$  is a smoothing operator in the transform domain similar to [74];  $\hat{G}$  is the resulting smoothed fringe image;  $\Psi^T$  and  $\Psi$  are the analysis and synthesis 2D-DTCWT operator, respectively. The 2D-DTCWT is chosen since the highlight detection is carried out within the 2D-DTCWT based FPP framework as described in Section 2.3. Besides, smoothing the fringe image in the 2D-DTCWT domain can introduce less distortion due to the nearly shift-invariant and minimum aliasing properties of the 2D-DTCWT. By smoothing the fringe pattern, its average intensity will be lower than the highlight. An example is shown in Figure 3-5, which gives the histogram of the fringe image in Figure 3-3(a) after the smoothing operation. Comparing with Figure 3-3(b), the peak for the highlight can now be clearly identified. It greatly simplifies the determination of the threshold (vertical dash line).

For automatically determining the threshold, a good mathematical model of the histogram of  $\hat{G}$  needs to be obtained. Let us denote  $P_{\hat{G}}(u)$  as the probability density function (*pdf*) of the image  $\hat{G}$ . It can be modeled as the following mixture model,

$$P_{\hat{G}}(u) = \sum_{k=1}^{N_k} P_k(u)P(C_k) \quad (3-9)$$

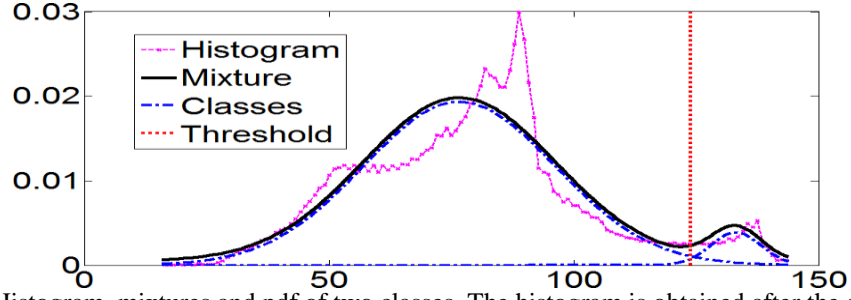


Figure 3-5 Histogram, mixtures and pdf of two classes. The histogram is obtained after the smoothing operation. The dash line is the optimum threshold.

where  $P_k(u)$  is the *pdf* of the class  $C_k$  for gray level  $u$  and  $P(C_k)$  is the *a-priori* probability of class  $C_k$  of  $\hat{G}$ . We can approximate  $P_{\hat{G}}(u)$  using the histogram of  $\hat{G}$ . However the  $P_k(u)$  of each class as well as  $P(C_k)$  are not available in practice. The number of classes,  $K$ , is also unknown. To simplify the problem, we assume the *pdf* of all classes is Gaussian distributed with mean  $\mu_1 < \dots < \mu_{N_k}$  and variance  $\sigma_1, \dots, \sigma_{N_k}$ . More specifically, we approximate  $P_{\hat{G}}(u)$  by a Gaussian mixture model  $f^{\mathcal{N}}(u, N_k)$  as follows:

$$P_{\hat{G}}(u) \approx f^{\mathcal{N}}(u, N_k) = \sum_{k=1}^{N_k} f_k^{\mathcal{N}}(u, N_k; \theta_k) \quad (3-10)$$

and

$$f_k^{\mathcal{N}}(u, N_k; \theta_k) = P_k \mathcal{N}(u; \mu_k, \sigma_k) \quad (3-11)$$

where  $P_k$  is a mixing probability of the mixtures and  $\mathcal{N}(u; \mu_k, \sigma_k)$  is a Gaussian function with parameter  $\theta_k$  consisting of the mean  $\mu_k$  and the variance  $\sigma_k$ . As to the number of classes  $K$ , intuitively we can estimate it by solving the following constrained minimization problem:

$$\arg \min_{j \in \{2, \dots, j_{max}\}} j \quad s. t. \quad \frac{1}{N_{bin}} |p_{\hat{G}}(u) - f^{\mathcal{N}}(u, j)| < \lambda_{EM} \quad (3-12)$$

where  $N_{bin}$  is the total number of bins for the histogram,  $j$  is the estimated number of classes, and  $j_{max}$  is predetermined maximum number of classes in our estimation.

Given a threshold  $\tau$ , the above minimization problem (i.e., (3-10) and (3-11)) can be realized using an iterative Expectation Maximization (EM) algorithm [117].

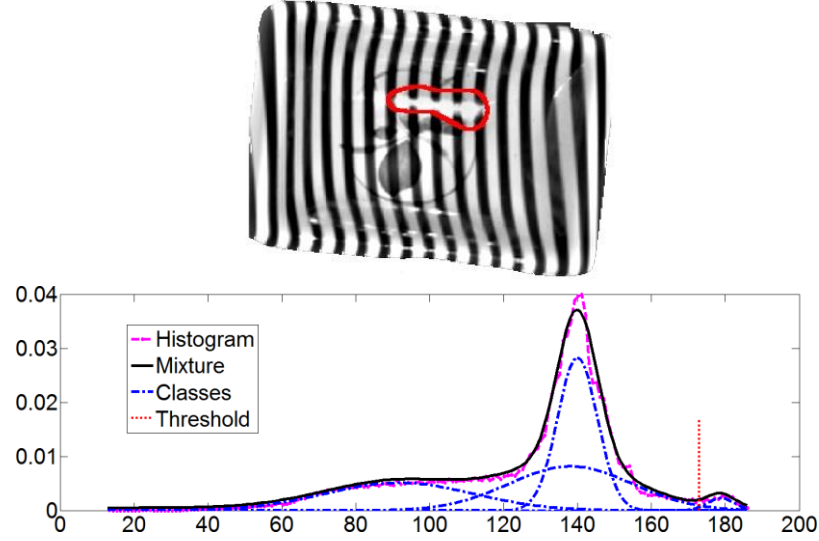


Figure 3-6 The object and its highlight area obtained by thresholding the histogram with the optimum threshold (see solid red line) obtained from the proposed multi-classes GMM approach.

Since highlights are characterized by pixels of high intensity values, we assume them to be the members of the class with the largest mean value  $\mu_{N_k}$ . Thus the threshold  $\lambda_{HEM}$  for highlight detection can be chosen as the intersection point of the final two classes. Mathematically, it can be expressed as follows:

$$\lambda_{HEM} = \arg \min_{u \in N} |f^N(u, N_k) - f^N(u, N_k - 1)| \quad (3-13)$$

The main advantage of the proposed GMM framework is its ability to provide a good approximation in a tractable way from the histogram. It is robust such that it can work well even when the fringe image is noisy or has other fluctuation in intensity. Figure 3-6 (top) shows a fringe image with a highlight region with is accurately detected (red line) by using the proposed GMM framework. Figure 3-6 (bottom) shows the histogram of the fringe image (solid line), and the optimal threshold obtained using the proposed GMM framework (red dot line).

### 3.4 GEOMETRIC SKETCHING OF FRINGE PATTERN

As mentioned above, the highlight will corrupt the fringe pattern in the affected region. In the worst case, the highlight region can be blown out such that all the fringes within the region will disappear. Without the fringes, the FPP reconstruction basically cannot be carried out. While the inpainting method as described in Section 3.2 can regenerate the fringe pattern in the highlight region, it is effective only when the region is small. If the region is large, the iterative regularization process may converge to any local minimum that can be far from the desired fringe pattern. In this case, the process will be robust only when a good initial guess of the fringe pattern is available. To obtain a good initial guess, we propose in this chapter to construct a geometric sketch of the missing fringe pattern in the highlight region and use it to guide the regularization process. An example is shown in Figure 3-12(a). Before explaining the procedure, let us assume that the fringe image has gone through the denoising and debiasing processes of the 2D-DTCWT based FPP framework [67] as described in Section 2.3. We denote the resulting fringe image as  $\dot{G}$ . Hence we assume  $\dot{G}$  is noise-free (or have the noise power, if any, significantly reduced) and has zero  $dc$  component.

#### 3.4.1 T-JUNCTION POINT DETECTION

To build an accurate geometric sketch, let us first introduce the T-junctions of the highlight region where fringes are missing. More specifically, let us denote  $p = \{p_k | p_k \in \partial\Omega\}$  be the points at the contour of the highlight region  $\Omega$ , where  $k \in 1, 2, \dots, N$ ; and  $N$  is the total number of points on  $\partial\Omega$ . Then we define the T-junctions to be the local extrema within  $p$  as follows:

$$\dot{p} = \{p_k | \dot{G}'(p_k) = 0 \wedge p_k \in p\} \quad (3-14)$$

for  $k \in 1, 2, \dots, \dot{N}$  where  $\dot{N} < N$ . Two types of T-junction  $\dot{p}_k$  are considered:

- 1) The maxima T-junction which is indicated by  $\dot{G}''(\dot{p}_k) < 0$ ,  $g''p_k < 0$  and
- 2) the minima T-junction which is indicated by  $\dot{G}''(\dot{p}_k) > 0$ .

Note that our definition of T-junction is different from [118] and [119] which define T-junctions as the points having a common vertex and the same gray levels. There are two major reasons why we define T-junctions based on the local extrema. First, it is to ensure the consistency of the T-junction detection because of the possible fluctuations in the pixel magnitude. Second, it is due to the fact that a gradually increasing or decreasing function exists between two consecutive local extrema. This property simplifies not only the T-junction detection but also the geometric sketching required for the iterative regularization at the later stage.

Let us further define three types of cue that characterize a T-junction  $\dot{p}_k$ :

- a. Amplitude  $m_k$
- b. Direction vector  $r_k$
- c. Flow degree  $s_k$

For a T-Junction point  $\dot{p}_k$ , its amplitude  $A_k$  is defined as,

$$m_k = S(\dot{G}(v_k)) \text{ for } k = 1, \dots, \dot{N} \quad (3-15)$$

where  $v_k$  is the neighbor points of T-junction  $\dot{p}_k$  and  $S(\cdot)$  is a statistical function such as median or mean. The use of the statistical function is to minimize the influence of the noise surrounding the T-junction and hence the resulting amplitude is more accurate. Figure 3-7a shows the T-junctions  $\dot{p}_k$  and their magnitude  $m_k$ . To simplify the presentation, all negative  $m_k$  are shown in blue (local minima) and all positive  $m_k$  are shown in red (local maxima).

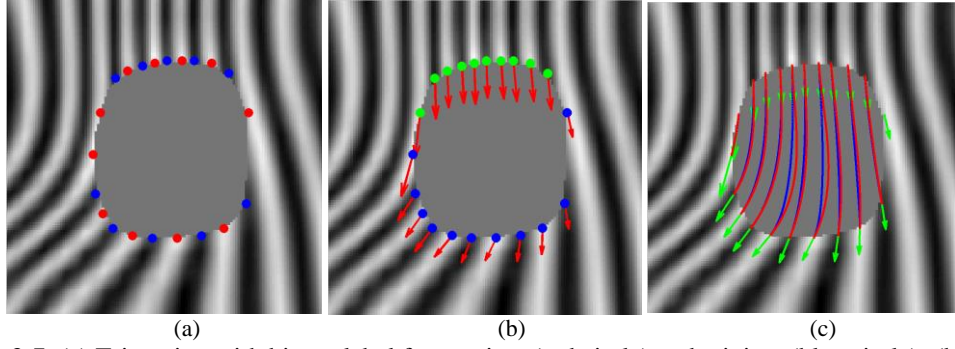


Figure 3-7 (a) T-junction with binary label for maxima (red circle) and minima (blue circle); (b) the orientation of T-junction with labels: the leaving T-junctions are green in color; and (c) the curve generated between pairwise compatible T-junction using the Bezier curve (blue curve) and the Clothoid (red curve).

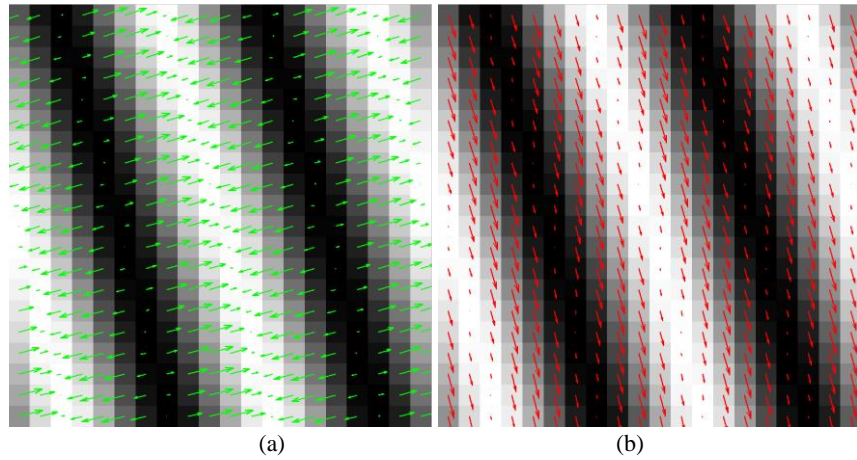


Figure 3-8 (a) Gradient of the fringe pattern; (b) direction of the fringe pattern

The direction vector  $r_k$  is basically the direction of the fringe pattern at the T-junction  $p_k$ . It is defined by,

$$r_k = S(\theta(v_k)) \text{ for } k = 1, \dots, \dot{N} \quad (3-16)$$

where  $\theta$  is the direction of the fringe pattern defined as:

$$\theta(\cdot) = \mathcal{W} \left\{ \angle \nabla (\dot{G}(\cdot))^\perp \right\} \text{ for } k = 1, \dots, \dot{N} \quad (3-17)$$

where  $\mathcal{W}$  is the wrapping operator to change the orientation angle to the first/second quadrant and  $\angle \nabla (\dot{G}(\cdot))^\perp$  is the normal of the gradient of  $\dot{G}(\cdot)$ . Figure 3-8 shows the difference between the gradient  $\dot{g}$  and the direction of the fringe pattern  $\theta$ . It can be seen that unlike the gradient of the image, the direction of T-junction is consistent to

the structure of the fringe pattern. Figure 3-7b shows the direction of the T-junction obtained from (3-15) and (3-16).

Lastly, the flow degree  $s_k$  is defined by,

$$s_k = S(\mathcal{M}(\dot{p}_k^r)) \text{ for } k = 1, \dots, \dot{N} \quad (3-18)$$

where  $\mathcal{M}(\cdot)$  is a mask with size the same as the image. It has the value of -1 in the highlight region and 1 otherwise. It is obtained from the highlight region detection algorithm as mentioned in Section 3.3. In (3-18),  $\dot{p}_k^r$  is a set of points in the neighborhood of the point  $\dot{p}_k + r_k$ , where  $r_k$  is obtained from (3-16). The flow degree  $s_k \in [-1,1]$  denotes whether the fringe at that T-junction point is going outward to the highlight region or going inward from the highlight region. For instance, if  $s_k$  is positive and larger than a threshold,  $\dot{p}_k$  is an outward T-junction. And if  $s_k$  is negative and smaller than a threshold,  $\dot{p}_k$  is an inward T-junction. Finally, if  $|s_k|$  is smaller than a small threshold, we dub such  $\dot{p}_k$  as the transition T-junction. An example of these T-junctions is shown in Figure 3-9. Note that the selection of the thresholds as mentioned above is not critical as shown in our experiments.

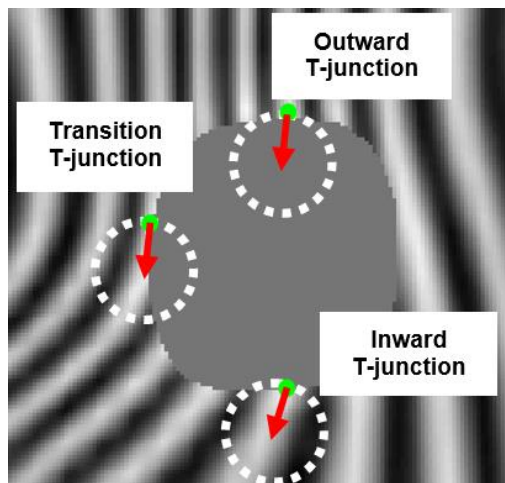


Figure 3-9 The flow of T-junction: inward, outward, and transition

### 3.4.2 FINDING POSSIBLE CONFIGURATIONS

Given a set of T-junctions  $\dot{p}$ , the next step is to build a configuration, which is defined as a set of pairwise compatible T-junctions. It is known that each outward T-junction should connect to an inward T-junction. They form a compatible pair. By determining all the compatible pairs, we can sketch the geometric structure of the missing fringe pattern in the highlight region. However, matching up the T-junctions using an exhaustive search approach can be very time consuming. To speed up the process, we utilize the transition T-junctions. As mentioned above, a transition T-junction is any T-junction that has an absolute flow degree  $|s_k|$  smaller than a threshold. When  $|s_k| \approx 0$ , the transition T-junction is in fact having the orientation nearly parallel to the tangent of the highlight region boundary. This notion does not only imply the boundary is in the direction as the fringe pattern, it also indicates that a compatible pair of T-junctions is near to that T-junction (as shown in Figure 3-9). Hence the transition T-junctions can be chosen as the initial point for searching the compatible pairs.

More specifically, let us first define a cost function given a pair of T-junctions  $\dot{p}_1$  and  $\dot{p}_2$  as follows:

$$C(\dot{p}_1, \dot{p}_2) = c_a C^a(\dot{p}_1, \dot{p}_2) + c_b C^b(\dot{p}_1, \dot{p}_2) \quad (3-19)$$

and

$$C^a(\dot{p}_1, \dot{p}_2) = \frac{|m_1 - m_2|}{2\|m\|_\infty}, \quad C^b(\dot{p}_1, \dot{p}_2) = \frac{|s_1 + s_2|}{2} \quad (3-20)$$

where  $c_a$  and  $c_b$  are the weights for the normalized cost  $C^a(\dot{p}_1, \dot{p}_2) \in [0,1]$  and  $C^b(\dot{p}_1, \dot{p}_2) \in [0,1]$ . If  $\dot{p}_1$  and  $\dot{p}_2$  are a compatible pair of T-junctions, their flow degree  $s_k$  should have opposite sign. Hence  $C^b(\dot{p}_1, \dot{p}_2)$  should be small. And since  $\dot{p}_1$  and  $\dot{p}_2$  should belong to the same fringe if they are a compatible pair, their

amplitude  $m_k$  should be similar. Thus  $C^a(\dot{p}_1, \dot{p}_2)$  will also be small. As a whole,  $C(\dot{p}_1, \dot{p}_2)$  will be small if  $\dot{p}_1$  and  $\dot{p}_2$  are a compatible pair of T-junctions. This cost function helps us match the T-junctions.

---



---

**Algorithm 1. Finding possible configurations**

---

**Inputs:** A set of T-junction points  $\dot{p} = \{\dot{p}_1, \dot{p}_2, \dots, \dot{p}_N\}$  and its magnitude  $m$ , direction vector  $r$ , and flow degree  $s$ .

**Output:** A set of possible configurations  $Z = \{\Pi_1, \Pi_2, \dots, \Pi_n\}$ .

---

1. **Let**  $i = 1$
  2. **For each** transition T-junction  $\vec{p}_i$ :
    - (a) Initialize a configuration  $\Pi_i = \emptyset$  and a list of temporary T-junctions  $\dot{p}_{temp} = \dot{p}$ .
    - (b) Let  $j = 1$  and start from the transition T-junction  $\vec{p}_i$ .
      - (i) Find an outward T-junction  $\dot{p}_1$  in clockwise direction from  $\vec{p}_i$  by selecting the first T-junction in  $\dot{p}_{temp}$ .
      - (ii) Find a compatible inward T-junction  $\dot{p}_2$  by walking counter-clockwise from  $\vec{p}_i \vec{p}_1$  and selecting the T-junction from  $\dot{p}_{temp}$  that minimizes (3-19). A pairwise compatible T-junction  $\varpi_j = (\dot{p}_1, \dot{p}_2)$  is thus formed.
      - (iii)  $\Pi_i \leftarrow \Pi_i \cup \varpi_j$  and remove  $\dot{p}_1$  and  $\dot{p}_2$  from the list  $\dot{p}_{temp}$ ;  $j = j + 1$ .
      - (iv) If no more outward T-junction is found in the list  $\dot{p}_{temp}$ , stop; else go to step (i).
    - (c)  $i = i + 1$ ; go to step (a) if  $i \leq n$ .
  3.  $Z = \{\Pi_1, \Pi_2, \dots, \Pi_n\}$ .
- 
- 

Now we are ready to introduce Algorithm 1. This algorithm suffices to obtain a set of configurations that realizes the connections without crossings each other. The algorithm makes use of the observation as mentioned above that there must be a compatible pair of T-junctions near a transition T-junction. Hence for each transition T-junction, we search the nearest outward and inward T-junctions to form a pair.

Then the next nearest outward and inward T-junctions are searched until all T-junctions are exhausted.

Note that for Algorithm 1, one configuration will be generated for each transition T-junction. Hence at the end, a set of  $n$  configurations is resulted from Algorithm 1, where  $n$  is the number of transition T-junctions. In the later step, the criteria for further selecting the optimal configuration from the set will be defined.

### 3.4.3 CURVE COMPLETION

Assuming the best configuration is obtained, we can then sketch the curves between the compatible T-junction pairs. They will be used as the initial guess of the missing fringes in the highlight region. Given two compatible T-junctions  $\varpi_j = (\dot{p}_1, \dot{p}_2)$  and their directions  $\varpi_j^r = (r_1, r_2)$ , we can sketch a curve to connect them by using the following approach. First we check if a straight line can connect the two points. If not, we apply a curve completion. Two kinds of curves are considered: the *C-shape* curves and *S-shape* curves as shown in Figure 3-10. A *S-shape* curve is used to connect the two T-junction pairs if their directions, i.e.  $r_1$  and  $r_2$ , are in the same  $90^\circ$  quadrant; otherwise a *C-shape* curve is applied. A *C-shape* curve can be generated by the quadratic Bezier function using an additional control point  $p_0$  as shown in Figure 3-10 (left).  $p_0$  can be obtained by drawing two straight lines from  $\dot{p}_1$  and  $\dot{p}_2$  following their direction  $r_1$  and  $r_2$ . The intersection point of the two lines is  $p_0$  for a *C-shape* curve. Meanwhile a *S-shape* curve can be generated by using a cubic Bezier curve but needs two additional control points,  $\dot{p}_a$  and  $\dot{p}_b$ , as depicted in Figure 3-10 (right). They can be obtained as follows: first, we draw two straight lines from  $\dot{p}_a$  and  $\dot{p}_b$  following their direction  $r_1$  and  $r_2$ . We draw another straight line to connect up  $\dot{p}_1$  and  $\dot{p}_2$ . Then the fourth straight line (green line in Figure 3-10 (right)) is drawn

that cuts the above three straight lines. The fourth straight line should be drawn based on the condition that the following cost function  $(90 - \alpha_a)^2 + (90 - \alpha_b)^2$  is minimized, where  $\alpha_a$  and  $\alpha_b$  are defined as in Figure 3-10 (right). With all the control points available, we can sketch a curve  $v$  that connects  $\dot{p}_1$  and  $\dot{p}_2$  using the following formulations [120]:

$$v(t) = \dot{p}_1(1-t)^2 + p_0 \cdot 2(1-t)t + \dot{p}_2 t^2 \quad (3-21)$$

for *C-shape* curves and

$$v(t) = \dot{p}_1(1-t)^3 + p_a \cdot 3(1-t)^2 t + p_b \cdot 3(1-t)t^2 + \dot{p}_2 t^3 \quad (3-22)$$

for *S-shape* curves. Note that  $t \in [0,1]$  in (3-21) and (3-22) denotes the normalized curve segment between the starting and ending control points. We can also employ the Euler spiral curve known as clothoids. To generate a clothoid, the algorithm in [121] can be used. In our implementation we found that both approaches gave similar results.

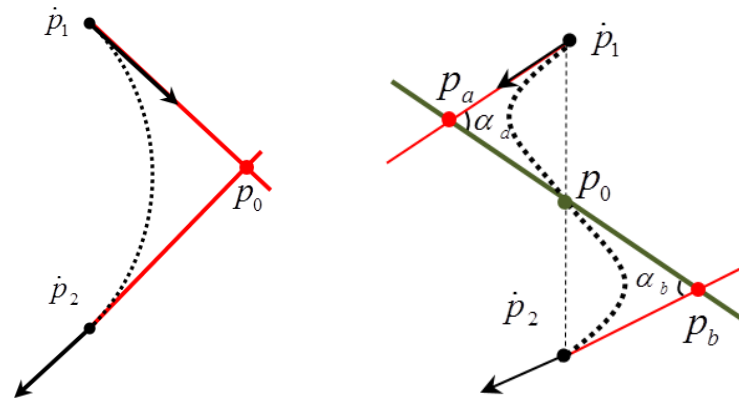


Figure 3-10 Curves generated by the Bezier functions. A *C-shape* curve (left) and a *S-shape* curve (right).

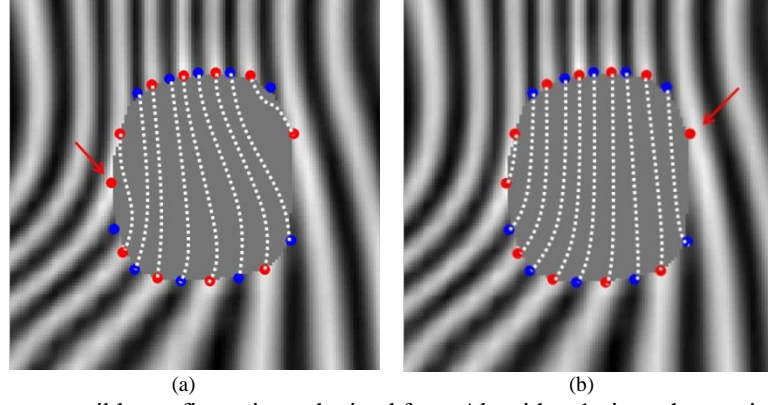


Figure 3-11 Some possible configurations obtained from Algorithm 1 given the starting transition T-junctions (red arrow). (a) Non-optimal configuration; and (b) the optimal configuration.

#### 3.4.4 SELECTING THE BEST CONFIGURATION

As shown in Figure 3-11, different configuration can be generated by Algorithm 1 when different starting transition T-junction is chosen. For a non-optimal configuration, the average curve total length is often larger than the optimal one because the orientations of the connected T-junctions often have larger variations than those of the optimal configuration. They end up with longer curves as illustrated in Figure 3-11 (a) and (b). Hence given a set of configurations  $Z$ , we suggest to select the best one based on the total length of the connections between its compatible T-junction pairs. Besides, the connections in such configuration must not be crossing each other and must be within the highlight region  $\Omega$ . The procedure to find the best configuration is described in Algorithm 2 below. Given a configuration  $\Pi_i$  and its curve set  $Y$ , where  $i = \{1, \dots, n\}$ , we first define the average total length of the connections between its compatible T-junction pairs as,

$$C(\Pi_i) = \sum_j \frac{L(v_i^j)}{N_v} \quad (3-23)$$

where  $L(v_i^j)$  is the length of the curve  $v_i^j$ ; and  $N_v$  is the total number of curves in the configuration. Based on  $L(v_i^j)$ , Algorithm 2 is summarized as follows:

---

**Algorithm 2. Selecting the best configuration**

---

**Inputs:** A set of configurations  $Z = \{\Pi_1, \Pi_2, \dots, \Pi_n\}$ .

**Output:** The best configuration  $\Pi_i$  and curve set  $Y_i$ .

---

1. **Let**  $i = 1$
  2. **For each** configuration  $\Pi_i \in Z$ 
    - (a) For each compatible T-junction pair  $\varpi = \{\varpi_1, \varpi_2, \dots, \varpi_{N_\varpi}\}$  where  $N_\varpi$  is the total number of pairs in the configuration  $\Pi_i$  and let  $j = 1$  and  $Y_i \leftarrow \emptyset$ .
      - (i) build a curve  $v_i^j$  by linking the compatible T-junction pair in  $\varpi_j$  using (3-21), (3-22), or [121]. The curve should be within  $\Omega$  and does not cross other curves.
      - (ii)  $Y_i = Y_i \cup v_i^j$ ;  $j = j + 1$ ; get back to (i) if  $j \leq M$ .
    - (b) Calculate  $C(\Pi_i)$  using (3-23).
    - (c)  $i = i + 1$  and get back to (a) if  $i \leq n$ .
  3. **Return** a configuration  $\Pi_i$  and  $Y_i$  such that  $C(\Pi_i)$  is the minimum.
- 

After the best configuration  $\Pi_i$  and its set of curves  $Y_i$  are obtained, the final step is to estimate the magnitude of the curves. It can be achieved by interpolating the curves using any linear function based on the magnitude of the T-junction pairs. Recall that for a compatible T-junction pair  $(\dot{p}_1, \dot{p}_2)$  with extrema magnitude  $(m_1, m_2)$ , the curve connecting between them is defined as  $v(t)$ , where  $t \in [0, 1]$  is a normalized index indicates the distance along the line  $v(t)$  from the starting point  $\dot{p}_1$ . Then the magnitude of the curve can be linear interpolated as follows:

$$m(t) = m_1 + t(m_2 - m_1) \quad (3-24)$$

It should be noted that the exact magnitude in fact is not important to the later reconstruction process since only the phase shift of the fringes will be considered. However, any disruption in the fringe magnitude will introduce distortion to the final reconstructed model. Hence an interpolation process like (3-24) is still useful to smooth the curves.

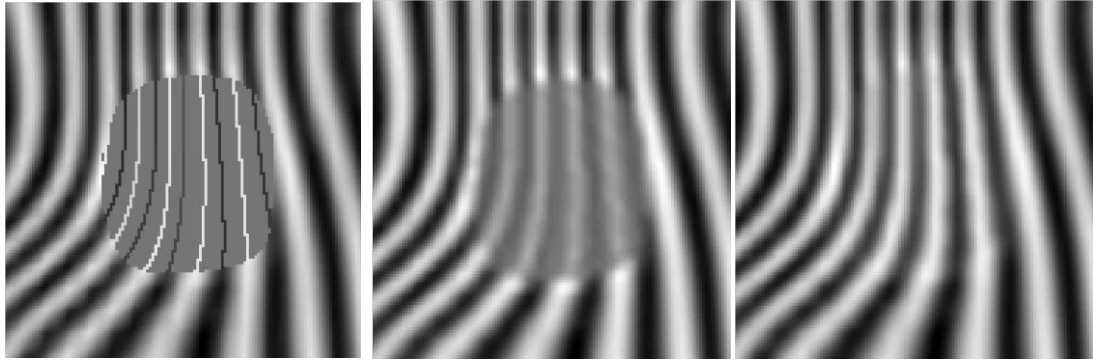


Figure 3-12. The 2D-DTCWT regularization on a fringe pattern. (a) Original fringe pattern after the curve interpolation. Note that the rest missing area is initialized to zero; (b) and (c) the regularization results after several iterations

Based on the approach as mentioned above, a geometric sketch of the missing fringes in the highlight region can be obtained. Figure 3-12 (left) shows the final geometric sketching result. It can be seen that all compatible T-junction pairs are correctly connected together. Note that the rest of the highlight region is initialized to zero. Based on this initial guess, the iterative regularization in (3-3) and (3-4) is applied to obtain the final inpainting result. Figure 3-12 (middle) and Figure 3-12 (right) show the results after the first iteration and when the iteration converges. The missing fringes in the highlight region are regenerated. In practice, the regularization can usually converge in a few iterations. Hence the whole inpainting process is rather fast.

### 3.5 SIMULATION AND EXPERIMENT

To evaluate the performance of the proposed algorithm, we first perform a simulation using computer generated fringe patterns. The shapes of the objects, i.e., “cone” and “peak”, and their fringe images are depicted in Figure 3-13(a)-(b) and Figure 3-14(a)-(b), respectively. These objects also serve as the ground truth for the evaluation of our proposed algorithm. To simulate the inpainting process in real working environments, two synthetic masks of oval and circle shape are used to generate the missing area and Gaussian noise is added to the fringe image as shown in Figure 3-13(c)-(d) and Figure 3-14(c)-(d). The size of the oval shape mask and the

circle shape mask are about 1,998 pixels and 2,728 pixels respectively. Meanwhile, the resolution of the fringe image is  $512 \times 512$ .

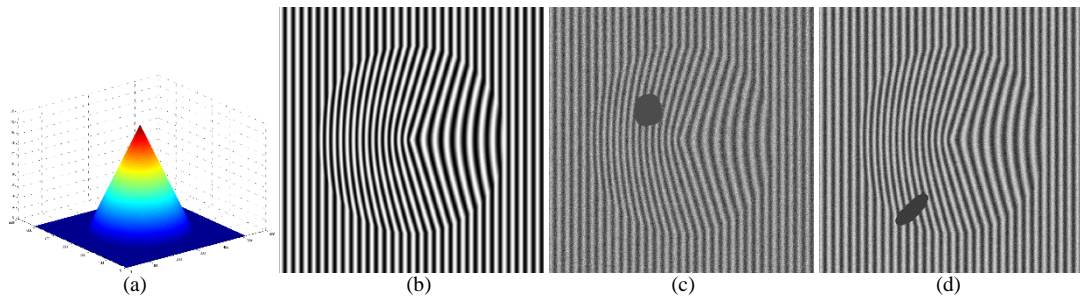


Figure 3-13. The object used in the simulation. (a) A computer generated 3D object “peak” (ground truth); (b) the deformed fringe pattern; (c) the deformed fringe pattern with noise and the circle shape mask added; (d) the deformed fringe pattern with noise and the oval shape mask added;

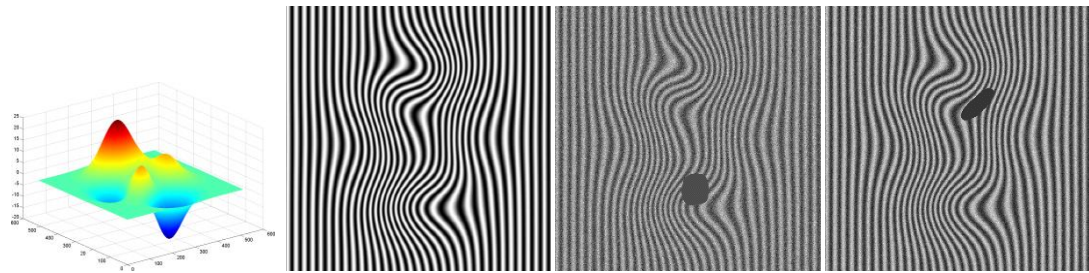


Figure 3-14. The object used in the simulation. (a) A computer generated 3D object “peak” (ground truth); (b) the deformed fringe pattern; (c) the deformed fringe pattern with noise and the mask added; (d) the deformed fringe pattern with noise and the oval shape mask added;

The proposed algorithm is then compared with the conventional iterative regularization method (2D-DTCWT), the exemplar based inpainting (EI) [102, 122], the wrapped phase image inpainting (WP-II) [54], the vector-valued image regularization with PDEs (VVIR-PDE) [123], the adaptive inpainting algorithm based on DCT induced wavelet regularization (AI-DCT-WR) [106], and an image inpainting approach using spatially adaptive iterative singular-value thresholding algorithm (SAIST) [124]. The conventional iterative regularization method actually is the proposed approach but without the proposed initial guess as the geometrical guidance. Note that all simulation codes are written in MATLAB running on a personal computer at 3.4 GHz except VVIR-PDE which is written in C++. For fair

comparison, the execution time of VVIR-PDE implemented with C++ is assumed, as it is claimed by [125], to be 10 times faster than that implemented with MATLAB. Table 3-1 and Table 3-2 show the average signal-to-noise ratio (SNR) when comparing with the ground truth of the object “cone” and “peak” respectively. Given  $h_{ori}$  as the depth of the ground truth and  $h$  as the depth after the inpainting procedure, SNR can be calculated by,

$$SNR = 10 \log_{10} \left( \frac{MAX_{gt}}{MSE} \right) \quad (3-25)$$

where  $MAX_{gt} = \sum_{i=0}^m \sum_{j=0}^n h_{ori}(i, j)^2$  and  $MSE = \sum_{i=0}^m \sum_{j=0}^n (h_{ori}(i, j) - h(i, j))^2$  and both  $m$  and  $n$  are set to be 512. The average of SNR is calculated by repeating 100 times for each algorithm at different noise levels, different masks, and different locations of the missing area. The location of the highlight area is randomly selected for each simulation. It can be seen in Table 3-1 and Table 3-2 that the proposed algorithm gives the highest SNR in all noise levels. Besides, the proposed initial guess is extremely important to the quality of the restored fringe image and to speed up the optimization process as shown in the comparison of execution time in Table 3-3. Significant distortion is noted if just implementing the iterative regularization without the proposed initial guess.

Table 3-1 Comparison of inpainting results on the object “cone” with an oval shape mask and a circle shape mask respectively

Noise Level	SNR						
	2D-DTCWT	EI	WP-II	VVIR-PDE	AI-DCT-IWR	SAIST	Proposed
Oval shape mask							
0	18.01	34.02	32.25	22.71	7.78	29.54	<b>37.64</b>
0.2	15.86	33.10	31.46	21.53	9.53	29.06	<b>36.40</b>
0.4	15.42	30.89	29.63	21.58	10.03	28.49	<b>33.01</b>
0.6	12.91	29.02	27.76	20.89	8.45	25.37	<b>30.05</b>
0.8	11.67	27.24	26.26	19.11	8.98	22.90	<b>28.81</b>
Circle shape mask							
0	11.53	32.09	30.15	22.47	15.12	14.81	<b>35.46</b>
0.2	12.12	32.01	30.66	21.89	14.98	15.82	<b>34.56</b>
0.4	9.88	30.12	29.16	21.89	14.47	14.96	<b>31.72</b>
0.6	10.75	28.13	26.18	21.19	13.14	14.60	<b>28.27</b>
0.8	10.09	27.54	26.98	18.85	11.63	14.88	<b>27.80</b>

Table 3-2 Comparison of inpainting results on the object “peak” with an oval shape mask and a circle shape mask respectively

Noise Level	SNR						
	2D-DTCWT	EI	WP-II	VVIR-PDE	AI-DCT-IWR	SAIST	Proposed
Oval shape mask							
0	15.82	30.52	24.83	23.36	12.58	28.71	<b>33.69</b>
0.2	14.65	28.40	25.04	22.85	12.86	28.31	<b>33.18</b>
0.4	14.43	26.02	23.15	21.82	11.88	26.12	<b>30.81</b>
0.6	14.67	25.16	23.28	20.92	11.87	23.36	<b>28.56</b>
0.8	14.59	24.57	22.85	20.05	12.21	23.49	<b>25.81</b>
Circle shape mask							
0	13.01	23.76	22.85	22.51	14.81	15.49	<b>31.23</b>
0.2	13.21	25.30	22.64	23.02	15.07	16.18	<b>30.78</b>
0.4	11.71	24.41	23.41	21.98	14.80	16.14	<b>30.60</b>
0.6	11.36	23.13	20.96	20.22	13.45	14.10	<b>27.03</b>
0.8	11.82	21.47	20.15	19.56	13.75	15.52	<b>25.27</b>

Table 3-3 Comparison of execution time

Methods	2D-DTCWT	EI	WP-II	VVIR-PDE	AI-DCT-IWR	SAIST	Proposed
Time (seconds)	2.47	3.81	5.05	37.47	20.99	293.26	1.09

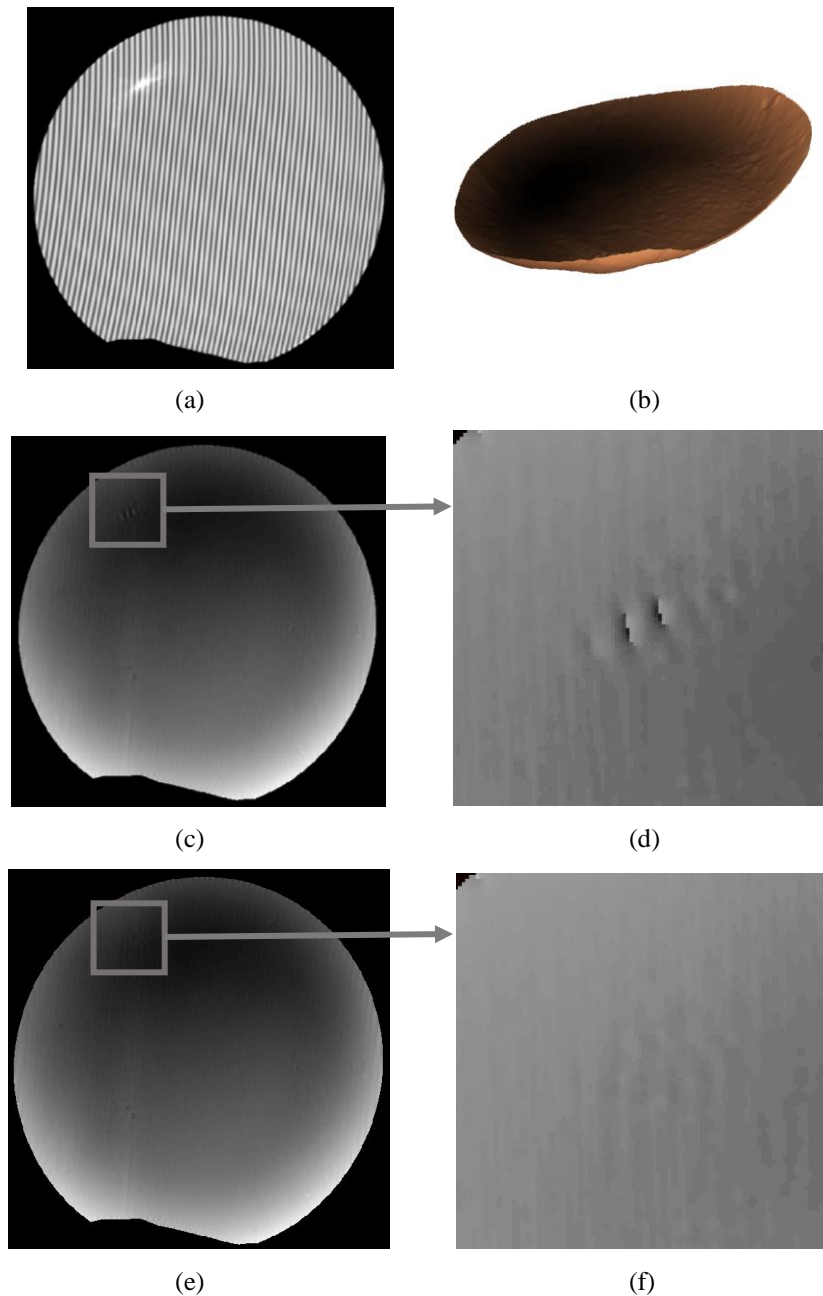


Figure 3-15. Experiment with a ceramic plate with highlight. (a) The fringe image; (b) the reconstructed 3D model; (c) the generated depth image using the conventional approach; (d) the blow up of the highlight region in (c); (e) The generated depth image using the proposed approach; and (f) the blow up of the highlight region in (e).

To evaluate the performance of the proposed algorithm in real working environments, we conducted a series of experiments using real objects. The proposed algorithm is implemented using a system consisting of a computer with a 3.4GHz CPU and 16GB RAM. It is connected to a video projector and a digital camera. The projector has a

light output of 3300 ANSI lumens and 2000:1 contrast ratio and the camera has a 22.2 x 14.8mm CMOS sensor and a 17-50mm lens. They are placed at a distance approximately 700mm from the object. Figure 3-15 shows a large ceramic plate with a small highlight region. Due to the highlight, some of the fringes are missing (Figure 3-15 (a)), resulting in a loss of the depth information. Using the conventional regularization method [103, 104], the missing area can be minimized but some distortion is introduced to the depth image (Figure 3-15 (c) and (d)). The proposed method improves the conventional regularization method and results in a better reconstruction as illustrated in Figure 3-15 (e) and (f) respectively. The resulting 3D model is depicted in Figure 3-15 (b).

Next we consider fringe images with larger highlight regions. Figure 3-16 shows the fringe image of a rectangular melamine plate with a long highlight region and Figure 3-17 shows a circular melamine plate with a big oval shape highlight at the center. In both cases, the highlight masks out some fringe patterns. We compare several inpainting methods: the conventional iterative regularization method (2D-DTCWT); the exemplar based inpainting (EI) [102, 122]; the wrapped phase image inpainting (WP-II) [54]; the vector-valued image regularization with PDEs (VVIR-PDE) [123]; the adaptive inpainting algorithm based on DCT induced wavelet regularization (AI-DCT-WR) [106]; and an image inpainting approach using spatially adaptive iterative singular-value thresholding algorithm (SAIST) [124]. As shown in Figure 3-16, if the highlight area is not big, some methods (except WP-II, AI-DCT-WR, and SAIST) can reconstruct the depth image reasonably well. As the highlight area getting bigger (as shown in Figure 3-17), the conventional regularization methods result in significant errors in the reconstructed depth image. The proposed method on the other hand can make a correct estimation of the missing area. Indeed the result is

expected since the regularization procedure of the proposed method is guided by the geometrical structure based on the fringe pattern on the boundary of the highlight region.

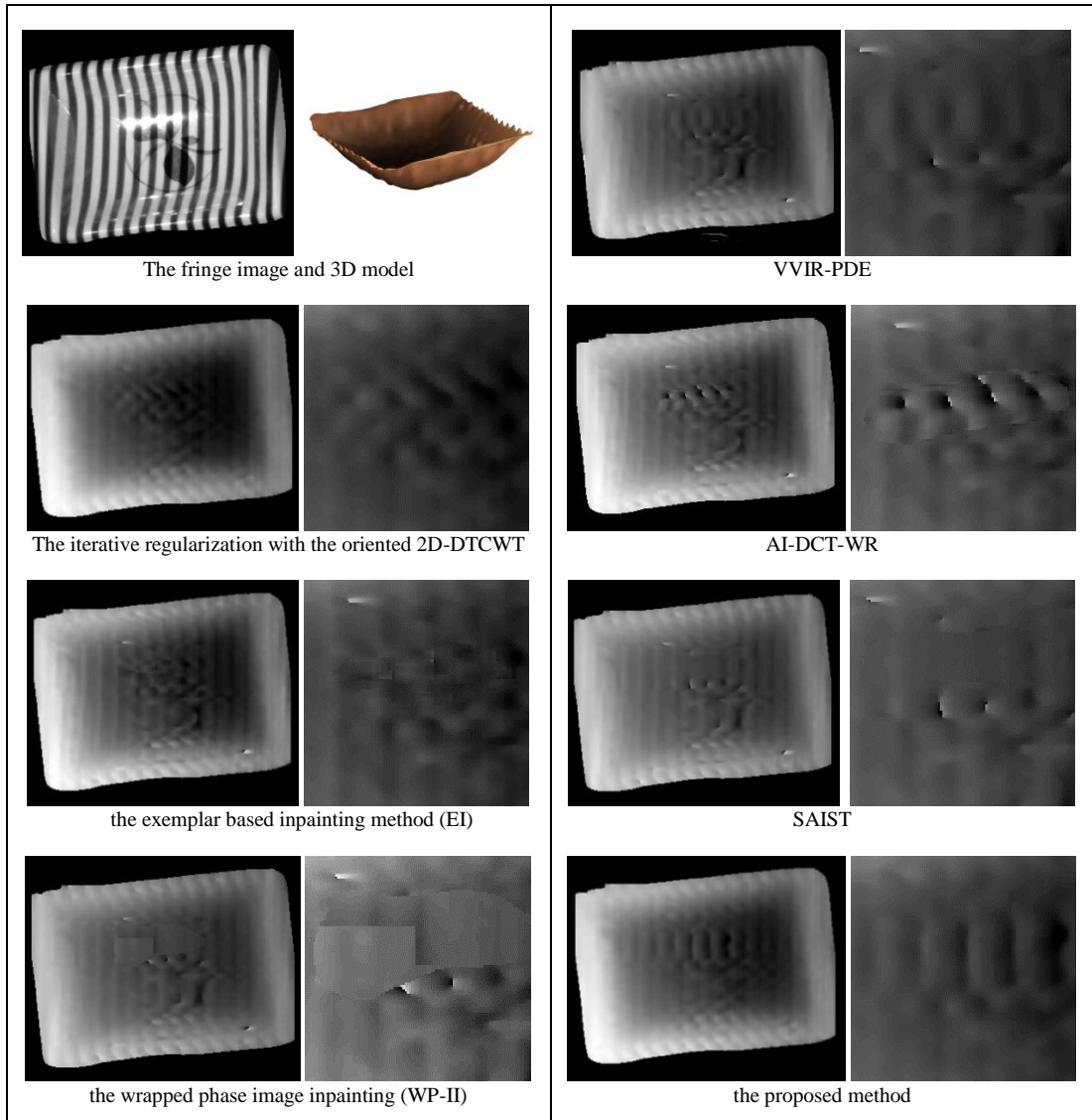


Figure 3-16. Comparison with other inpainting methods on a rectangular melamine plate with long highlight. **The 1<sup>st</sup> column:** (1<sup>st</sup> row) The fringe image with highlights and the 3D model reconstructed using the proposed method; (2<sup>nd</sup> row) iterative regularization with the oriented 2D-DTCWT; (3<sup>rd</sup> row) the exemplar based inpainting method [102, 122]; (4<sup>th</sup> row) the wrapped phase image inpainting (WP-II) [54]; **The 2<sup>nd</sup> column:** (1<sup>st</sup> row) the vector-valued image regularization with PDEs (VVIR-PDE) [123]; (2<sup>nd</sup> row) the adaptive inpainting algorithm based on DCT induced wavelet regularization (AI-DCT-WR) [106]; (3<sup>rd</sup> row) the image inpainting approach using spatially adaptive iterative singular-value thresholding algorithm (SAIST) [124]; (4<sup>th</sup> row) the proposed method

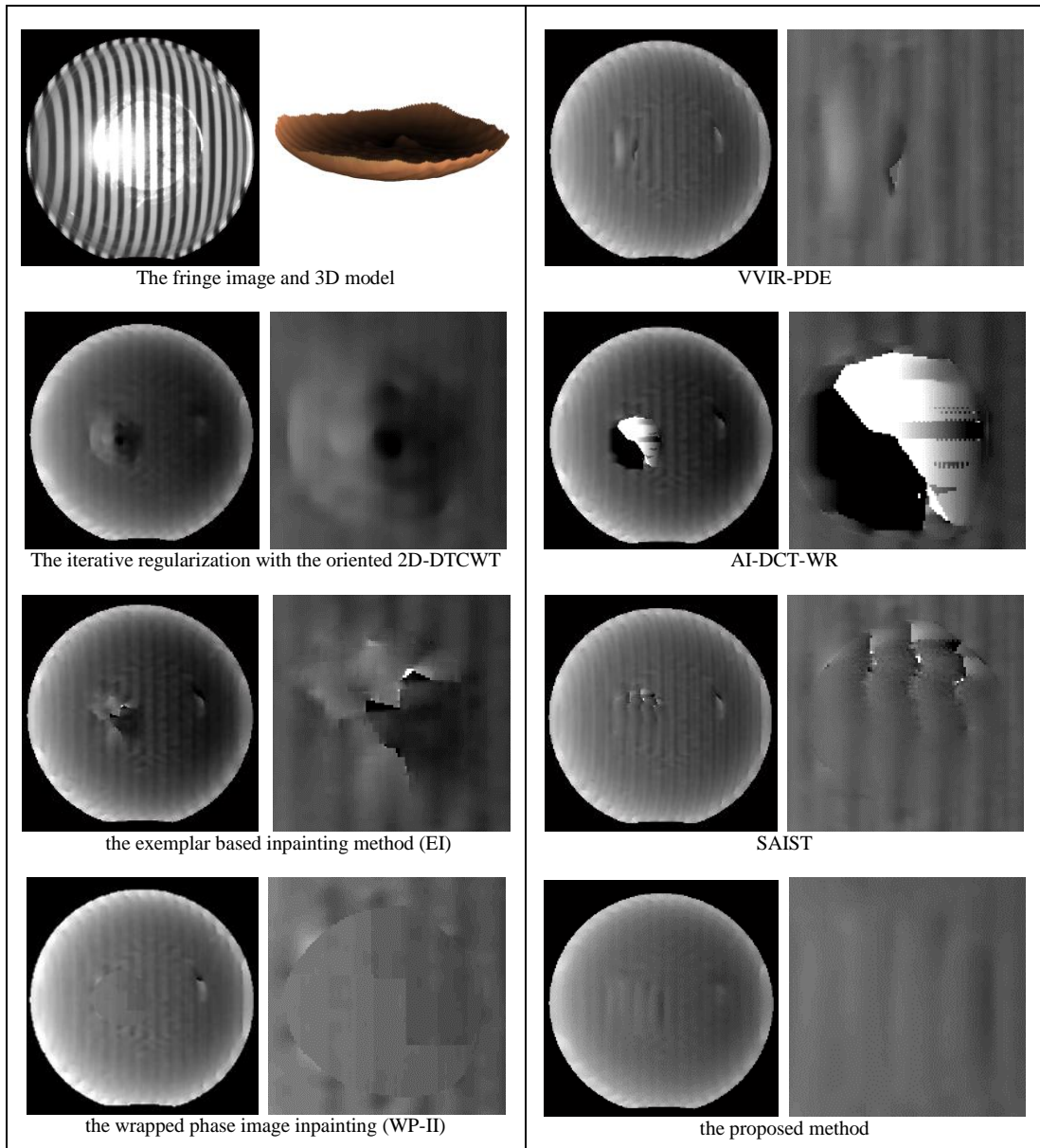


Figure 3-17. Comparison with other inpainting methods on a melamine plate with large highlights. **The 1<sup>st</sup> column:** (1<sup>st</sup> row) The fringe image with highlights and the 3D model reconstructed using the proposed method; (2<sup>nd</sup> row) iterative regularization with the oriented 2D-DTCWT; (3<sup>rd</sup> row) the exemplar based inpainting method [102, 122]; (4<sup>th</sup> row) the wrapped phase image inpainting (WP-II) [54]; **The 2<sup>nd</sup> column:** (1<sup>st</sup> row) the vector-valued image regularization with PDEs (VVIR-PDE) [123]; (2<sup>nd</sup> row) the adaptive inpainting algorithm based on DCT induced wavelet regularization (AI-DCT-WR) [106]; (3<sup>rd</sup> row) the image inpainting approach using spatially adaptive iterative singular-value thresholding algorithm (SAIST) [124]; (4<sup>th</sup> row) the proposed method

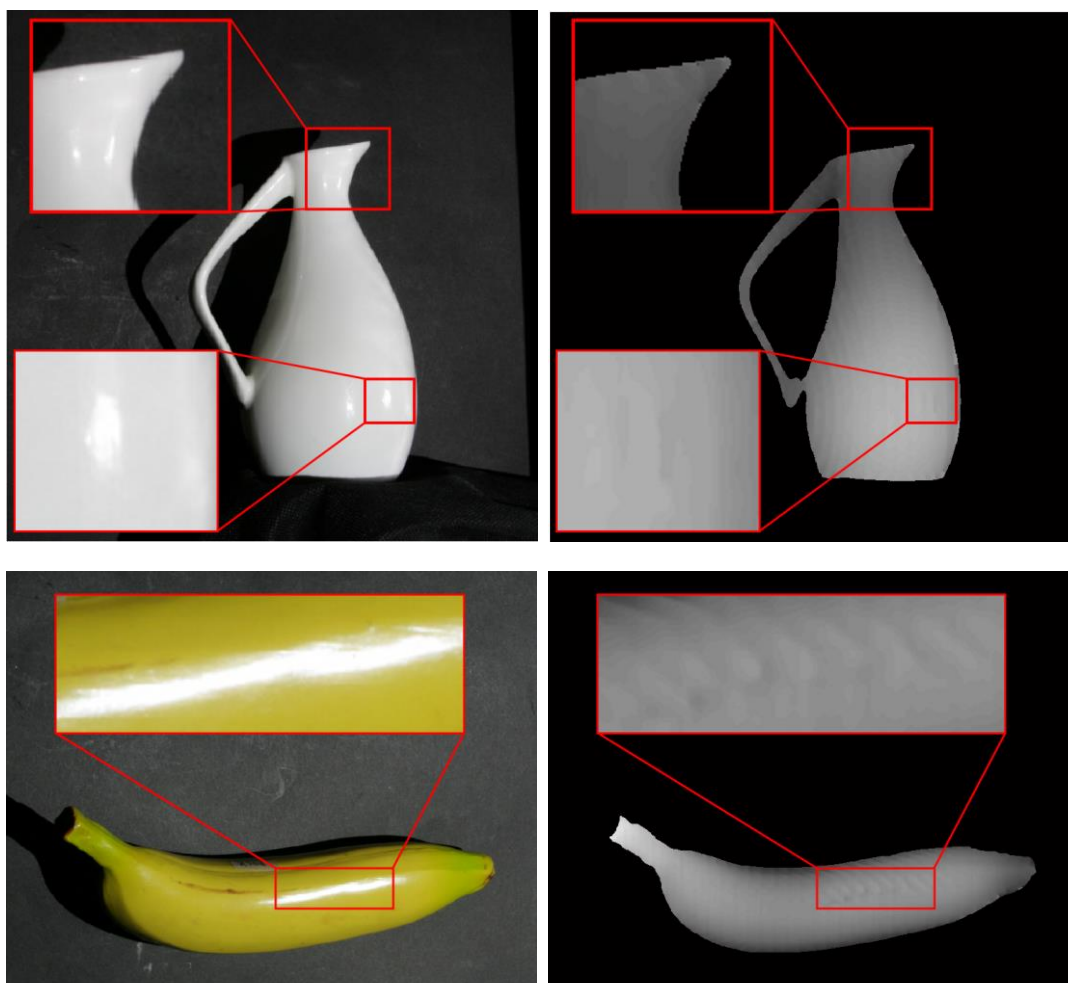


Figure 3-18. Performance of the proposed method for objects with complex shape and strong color variation.

Finally, we show in Figure 3-18 the performance of the proposed method for objects with complex shape (a ceramic jug) and strong color variation (a plastic banana). It can be seen that the proposed method performs equally well. It shows the robustness of the proposed method.

### 3.6 SUMMARY

In this chapter, a novel method for inpainting fringe images in the presence of highlights is proposed. The proposed method can detect the highlight regions in a fringe image and regenerate the fringes that are masked by the highlights. The algorithm is based on an iterative regularization procedure with additional geometrical sketching of the fringe pattern in the highlight regions. It serves as the

initial guess and guides the iterative regularization process to converge to the desirable result. Simulation and experimental results show that the proposed algorithm is able to accurately estimate the missing fringe patterns due to the highlights and thus correct the errors in the reconstructed 3D model which can be found when using the traditional methods.

# CHAPTER 4

## PERIOD ORDER ENCODED COMPLEX WAVELET TRANSFORM PROFILOMETRY

In the previous chapter, we have shown that DTCWT is an effective tool not only for denoising and removing bias of fringe images, but also for regenerating the missing fringes due to the presence of highlights. However, the problem of FPP is not only about highlights; the ambiguity problem as mentioned in Chapter 1 can also lead to severe distortions to the final reconstructed 3D model. Recall that the ambiguity problem is introduced due to the phase analysis process of FPP which gives only the wrapped phase data. The same is applied to the FPP systems using DTCWT. In this chapter, we propose a new marker encoding and detection algorithm which can estimate the period order information of the fringes. It is then used to assist the phase unwrapping procedure in solving the ambiguity problem. The proposed algorithm is robust in obtaining the 3D model with fringe images having complex scene, such as containing multiple objects. Besides, it is computationally efficient.

This chapter is organized as follows. Section 4.1 presents a brief review on some recent related research works to solve the ambiguity problem in FPP. Section 4.2 describes the proposed marker encoded fringe pattern that carries the period order information. Section 4.3 presents the proposed period order estimation algorithm.

Section 4.4 shows the simulation and experimental results and section 4.5 summarizes this chapter. The content of this chapter is extracted from our paper published in *Applied Optics* [126].

## 4.1 RELATED WORKS

As mentioned earlier, any phase imaging system including FPP gives only a modulo- $2\pi$  wrapped phase in its phase analysis process. Hence conventionally a phase unwrapping procedure is performed to recover the absolute (true) phase. Many phase unwrapping algorithms have been proposed to estimate the true phase shift by integrating the wrapped phase differences [3]–[6]. However, due to the various artifacts in the fringe images, some of the wrapped phase data can be missing. The same can also happen when the target object has a sharp change in height. Directly carrying out the unwrapping process with such erroneous data will lead to severe distortion to the final reconstructed 3D model. Recent quality-guided phase unwrapping methods, such as [5], will also fail particularly when the fringes have phase discontinuity along the object boundary with respect to the reference background. It is the case when the object does not have a direct contact with the reference background or the object itself has a curvature (such as a bowl) such that some parts of it cannot be seen from the angle of the camera.

In fact, the above problem stems from Itoh's assumption [3] that assumes the absolute phase can be estimated by integrating the wrapped phase difference. The estimated true phase shift will thus have much error if some of the phase data are missing. To solve this problem, recent approaches try to embed the period order information in the projected fringe patterns. By period order, we refer to the number of  $2\pi$  jumps in the phase angle that is hidden in the wrapped phase data. If the period

order is known, phase unwrapping can be achieved even when some of the wrapped phase data are missing. Traditional approaches embed the period order information to the fringe patterns using, for instance, multiple cameras [2, 7], multi-wavelength fringe pattern [80], fringe pattern with additional information, such as colors [79], speckles [40], and markers [38, 49, 127], multiple frequencies [81], multiple patterns [82, 83], and gray coded fringe patterns [5, 84], etc. However, the approaches in [2], [7], and [80] require additional hardware systems. The performance of the approach in [49, 79, 81] can be seriously affected by the color pattern of the object, whereas the approaches in [38] and [127] can only be applied to fringe images having a simple scene (e.g., a single object). The approaches in [5, 84], [82], and [83] require additional fringe projections, hence are not suitable to dynamic applications. In addition to the above approaches, it was recently reported in [35] that a dual frequency scheme can be used to embed the period order information to the fringe patterns in a phase measurement profilometry process (PMP-DF). In such method, high frequency fringe patterns are generated to encode the object's height information similar to the traditional phase shifting profilometry (PSP) approaches [34]. And low frequency signals are added to the fringe patterns to encode the period order information. Similar to other PSP methods, it requires at least 5 fringe patterns to obtain both the wrapped phase data and the period order information. Hence it is also not suitable to dynamic applications. Besides, our experiment shows that the method is highly sensitive to the quality of the fringe images. It will be exemplified in Section 4.4.

In this chapter, a new period order encoding and detection algorithm is proposed. The new algorithm encodes the period order information based on the spatial distribution of some strip markers which are carefully embedded in the fringe pattern.

After projecting the fringe pattern onto the object, the markers are detected from the fringe image to assist the phase unwrapping process. Similar to the inpainting algorithm as described in Chapter 3, the proposed algorithm is included as a subsystem of the DTCWT FPP framework as explained in Chapter 2. Hence the proposed approach is applicable to objects with color texture. Furthermore, the proposed algorithm is applicable to scenes which contain several objects with sudden jumps in height. And unlike the approaches that use multiple frame patterns, the proposed scheme is applicable to dynamic applications because it requires only a single fringe pattern for the entire operation. Finally, the algorithm is not sensitive to the quality of the fringe image. As different from PMP-DF, the period order information can be detected accurately with noisy fringe images or images with abnormal brightness. With the period order information, we can reconstruct the 3D model of the object even when some of the fringe data are missing due to the artifacts of the fringe image or the irregularity of the object shape.

## 4.2 PROPOSED MARKER CODING FOR CONSISTENT PHASE

### UNWRAPPING

Instead of using (2-18) which is based on the Itoh condition, the relationship between the absolute phase  $\phi_y(x)$  and the wrapped phase  $\hat{\phi}_y(x)$  can be written as follows [50]:

$$\phi_y(x) = \hat{\phi}_y(x) + k_y(x)2\pi \quad (4-1)$$

where  $k_y(x) \in \mathbb{Z}$  is the so-called period order that determines the number of  $2\pi$  jumps required to unwrap the wrapped phase. If  $k_y(x)$  is known,  $\phi_y(x)$  can always be computed even if some of the wrapped phase information is missing. In this chapter, we propose to embed a set of structured markers into the projected fringe

pattern to facilitate the estimation of the period order  $k_y(x)$  from the fringe image.

The marker encoded fringe pattern is defined as follows:

$$G_y^{marker}(x) = G_y(x) + m_y(x) \quad (4-2)$$

where  $G_y(x)$  is the original sinusoidal fringe pattern and  $m_y(x)$  is the marker signal added to the fringe pattern as illustrated in Figure 4-1.

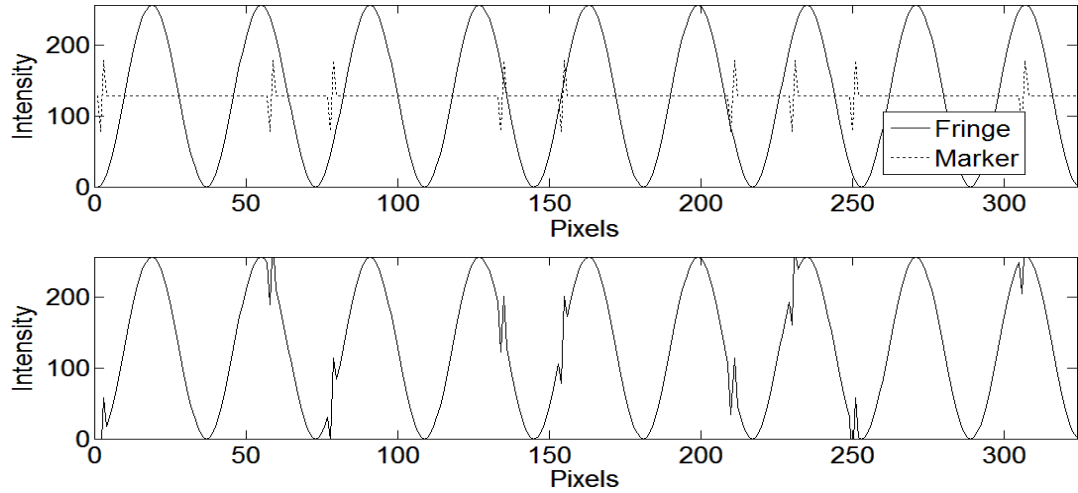


Figure 4-1. The original sinusoidal fringe pattern (for a particular row) and the markers (top). Resulting fringe pattern with markers embedded (bottom).

As shown in the figure, the markers are realized as a sequence of impulses (dash line) added to the original sinusoidal fringe pattern (solid line) at different phase angles. These phase angles are carefully selected such that they encode the order number of the sinusoidal period. Ideally, for every sinusoidal period in  $G_y$  with period order number  $k_y$ , a marker should be added to it at phase angle  $\theta_y(k_y) = M(k_y)$ , where  $M(\cdot)$  is a unique mapping function. It is however difficult to achieve in practice since each sinusoidal period is represented by a limited number of pixels of the fringe pattern. It is not possible to have many different  $\theta_y(k_y)$ . That is, there can only be a limited number of unique markers. Suppose that every sinusoidal period is represented by  $T_o$  pixels of the fringe pattern and every marker has a size of  $T_m$  pixels. Then at most  $N_m = T_o/T_m$  unique markers can be made. Here we assume  $T_o$  is an

integer multiple of  $T_m$ . In this case, a marker will be added to a sinusoidal period at phase angle  $\theta_y(k_y) = M(\langle k_y \rangle_{N_m})$ , where  $\langle a \rangle_b$  refers to  $a$  modulo  $b$ . In our experiment, we choose  $T_o = 36$  and  $T_m = 4$ . Hence, 9 unique markers can be inserted into 9 different sinusoidal periods respectively. The set of markers will be repeated for the next 9 sinusoidal periods. Such arrangement allows phase unwrapping using (4-1) when up to 8 consecutive sinusoidal fringe periods are missing due to whatever reasons. This resolvability is sufficient in normal applications of FPP.

To facilitate the detection of the markers, the mapping function  $M(\cdot)$  should be designed to maximize the difference of  $\theta_y(k_y)$  between two neighboring markers. A natural choice is as follows:

$$\begin{aligned} \theta_y(k_y) &= M(\langle k_y \rangle_{N_m}) \\ &= \left\langle \langle k_y \rangle_{N_m} \cdot \frac{N_m + 1}{2} \right\rangle_{N_m} \cdot \frac{2\pi}{N_m} \\ &= \left\langle k_y \cdot \frac{N_m + 1}{2} \right\rangle_{N_m} \cdot \frac{2\pi}{N_m} \end{aligned} \quad (4-3)$$

Here we assume  $N_m$  is an odd number. It is shown in Appendix A that the mapping function in (4-3) ensures neighboring markers will have a difference in  $\theta_y(k_y)$  with value at least  $\frac{(N_m-1)\pi}{N_m}$ , which is about the maximum possible value (i.e.  $\pi$ ).

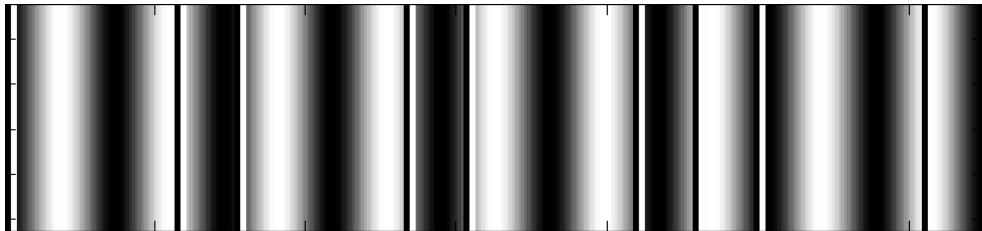


Figure 4-2. A fringe pattern with markers located at different phase angles of the sinusoidal fringes.

An example of the marker encoded fringe pattern is shown in Figure 4-2. In the figure, the thick black and white columns are the sinusoidal fringe projection pattern.

The markers are characterized by the sharp black and white lines. As mentioned above, we select  $N_m = 9$  in our experiment. Following (4-3), 9 markers are inserted into 9 consecutive sinusoidal periods at 9 different phase angles  $\{0, 5\xi, 1\xi, 6\xi, 2\xi, 7\xi, 3\xi, 8\xi, 4\xi\}$ , where  $\xi = 2\pi/9$ , respectively. With this arrangement, any 2 neighboring markers are separated by at least  $4\xi$ . Such arrangement maximizes the difference in  $\theta_y(k_y)$  of neighboring markers. It will improve the performance of the later marker detection process. Based on (4-3), we can also define  $m_y(x)$  of (4-2) as follows:

$$m_y(x) = \sum_{k_y} (f_{k_y}(x) * \delta) \quad (4-4)$$

where

$$f_{k_y}(x) = \begin{cases} 1 & x = T_m \cdot \left\langle \frac{k_y(N_m + 1)}{2} \right\rangle_{N_m} + T_o \cdot (k_y - 1) \\ 0 & \text{otherwise} \end{cases} \quad (4-5)$$

In (4-4) the symbol  $*$  denotes linear convolution and  $\delta$  can be any short support impulsive function. In our experiment, we set  $\delta$  to be the first derivative of an impulse function. Each marker is represented by 4 pixels in the projected fringe pattern as mentioned above.

### 4.3 PERIOD ORDER ESTIMATION ALGORITHM

In this section, we discuss how the embedded markers and in turn the period order information are obtained from the fringe image captured by the camera. The captured fringe image with markers embedded will be processed based on the DTCWT FPP framework as shown in Figure 2-9. Then the wavelet coefficients of 6 orientations at different levels will be generated. Recall that the markers are signals of sharp changes in magnitude. They induce strong wavelet coefficients particularly in the

first few levels. On the other hand, normal fringe patterns usually do not have high frequency contents. Hence their wavelet coefficients can often be found in higher levels of the wavelet transform. For the proposed algorithm, we examine the first 2 levels of the wavelet transform to detect the positions of the markers. Note also that the markers are added row-wise to the fringe pattern, they will not introduce wavelet coefficients of all 6 orientations. To be specific, only the subbands of  $45^\circ$ ,  $75^\circ$ ,  $105^\circ$ , and  $135^\circ$  will contain significant wavelet coefficients of the markers.

Those wavelet coefficients will be sent to the Period Order Estimation function block as shown in Figure 2-9. Denote the wavelet coefficients at level  $j$  and orientation subband  $m$  as  $d(j, m)$ . The marker cue information  $Q$  is first computed in the Period Order Estimation function block using the following formulation,

$$Q = \sum_{j=1}^2 \mathcal{F}_j \left( \alpha^j \left[ \sum_{m=\{45^\circ, 75^\circ, 105^\circ, 135^\circ\}} |w_j^m| \right] \right)^\beta \quad (4-6)$$

where  $|w_j^m|$  is the magnitude of the complex wavelet coefficients. Parameters  $\alpha$  and  $\beta$  are used to control the contribution of the wavelet coefficients to the marker cue function. We empirically select  $\alpha = 1$  and  $\beta = 1$ , as our experiments show that the final result is not sensitive to their selection. In (4-6), function  $\mathcal{F}_j(\cdot)$  is an interpolation function (e.g., bilinear interpolation) applied to the accumulation results of each level such that they have the same size as the original fringe image. Due to the shift invariance property of the DTCWT [128], the singularities that characterize the markers in the fringe image will generate strong coefficients at similar positions at all levels in the DTCWT domain. The Gaussian-like magnitude response of the wavelet functions [128] will also ensure that each marker will have only one

maximum of  $Q$ . Thus the position of the maxima in  $Q$  is strongly related to the position of the markers

However, the first two levels of the wavelet transform are also swamped by the coefficients of noises. It means that the maxima in  $Q$  can also be contributed by noises. Hence in practical setting, detecting markers by using only the maxima of  $Q$  will get false detection results, as illustrated in Figure 4-3.

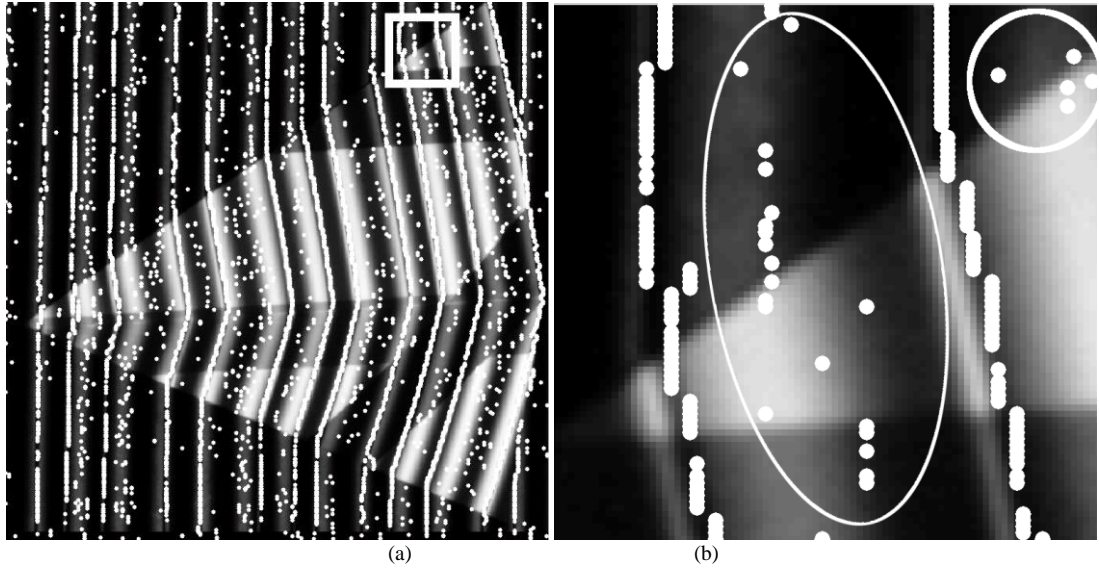


Figure 4-3. Marker detection results: (a) using only the maxima of  $Q$ ; (b) the zoom in version which shows many falsely detected markers (circled).

To identify the maxima of the markers, we threshold both the magnitude and phase of the complex wavelet coefficients at the positions where the maxima of  $Q$  are found. The magnitude of the markers' wavelet coefficients in general should be much higher than that of noises. So a thresholding operation to the magnitude of the wavelet coefficients can be performed first to remove the maxima contributed by noises of small magnitude. Given the wavelet coefficients  $w_j^m$  at  $j = 1$  and  $2$  and  $m = \{45^\circ, 75^\circ, 105^\circ, \text{ and } 135^\circ\}$ , the following operation is carried out:

$$w_j^m|_{x,y} = \begin{cases} w_j^m|_{x,y} & \text{if } |w_j^m|_{x,y}| > \lambda_{j,m}^{univ} \\ 0 & \text{Otherwise} \end{cases} \quad (4-7)$$

where  $w_j^m|_{x,y}$  is the  $w_j^m$  at position  $\{x, y\}$  and  $\lambda^{univ}$  is the so-called universal threshold that is commonly used in many wavelet denoising applications [111, 129, 130]. It is defined as follows:

$$\lambda_{j,m}^{univ} = \sigma_{j,m}^n \sqrt{2 \log N_{j,m}} \quad (4-8)$$

where  $N_{j,m}$  denotes the number of coefficients at level  $j$  and orientation subband  $m$ ;  $\sigma^n$  is the standard deviation of noise which is estimated using the robust statistics [131] by  $\sigma_{j,m}^n \approx \text{median}\{|w_j^m|\}/0.6745$ .

To further improve the detection of the maxima of the markers, we consider the local relative phase of the complex wavelet coefficients [132-134]. By definition, the local relative phase  $\angle w_j^m$  of the complex wavelet coefficients  $w_j^m$  is given by [132, 133],

$$\angle w_j^m = \angle w_j^m|_{x,y} - \angle w_j^m|_{x+1,y} \quad (4-9)$$

where  $\angle w_j^m|_{x,y}$  is the local phase angle at position  $\{x, y\}$ . While the local phase of the complex wavelet is known to be arbitrary irrespective to the structure of the image, there is a strong relationship between the local relative phase and the orientation of the edges in natural images [133]. Our experiment shows that it also provides a good description of the markers. Since all markers have the same structure, they incur complex wavelet coefficients of similar local relative phase. It however is not case for those of noises. An example is shown in Figure 4-4.

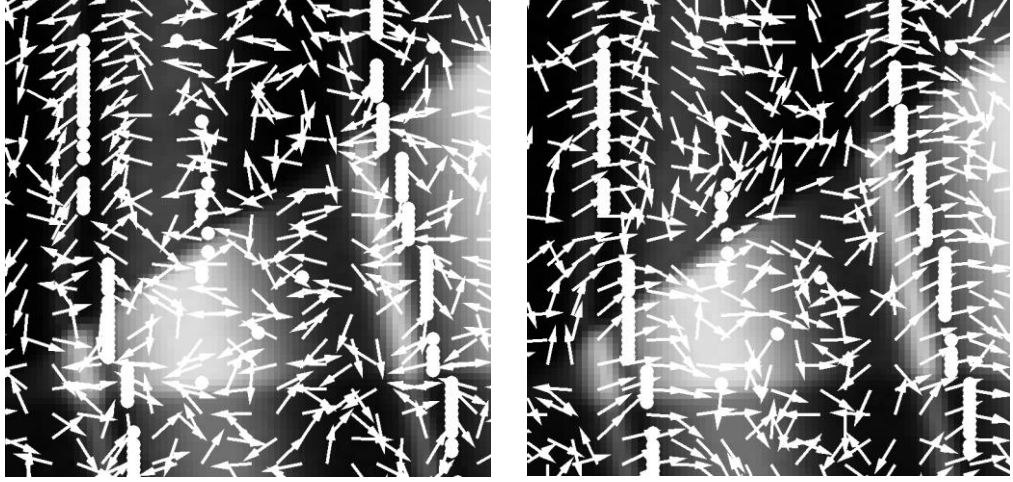


Figure 4-4. A comparison of local phase and local relative phase: (left) local phase; (right) local relative phase.

As it is seen in Figure 4-4 (left), the local phases (arrows) around the markers' maxima have unpredictable directions. However, the local relative phases (arrows) as shown in Figure 4-4 (right) around the markers' maxima have a similar horizontal direction, while it is not the case for those of noises. For the proposed algorithm, we first compute the mean relative phase of the complex wavelet coefficients. More specifically, we apply a 2D rectangular mask of 3x3 centered at every complex wavelet coefficient  $w_j^m$ . Then the mean of the relative phase  $\overline{\angle w}$  from the set  $\angle w(i)$  for index  $i \in 1, \dots, n$  is computed by,

$$\overline{\angle w} = \arctan \left( \frac{\sum_{i=1}^{N_{\angle w}} \cos \angle w(i)}{\sum_{i=1}^{N_{\angle w}} \sin \angle w(i)} \right) \quad (4-10)$$

where  $N_{\angle w}$  is the number of maxima point in a particular mask. Finally the following thresholding procedure with respect to the relative phase mean  $\overline{\angle w}$  is performed as,

$$w_j^m|_{x,y} = \begin{cases} w_j^m|_{x,y} & \text{if } \overline{\angle w_j^m}|_{x,y} - \pi < \varepsilon \\ 0 & \text{otherwise} \end{cases} \quad (4-11)$$

where  $\overline{\angle w_j^m}|_{x,y}$  is the mean relative phase at level  $j$  and orientation subband  $m$  at position  $\{x, y\}$ ; and  $\varepsilon$  is a very small real number.

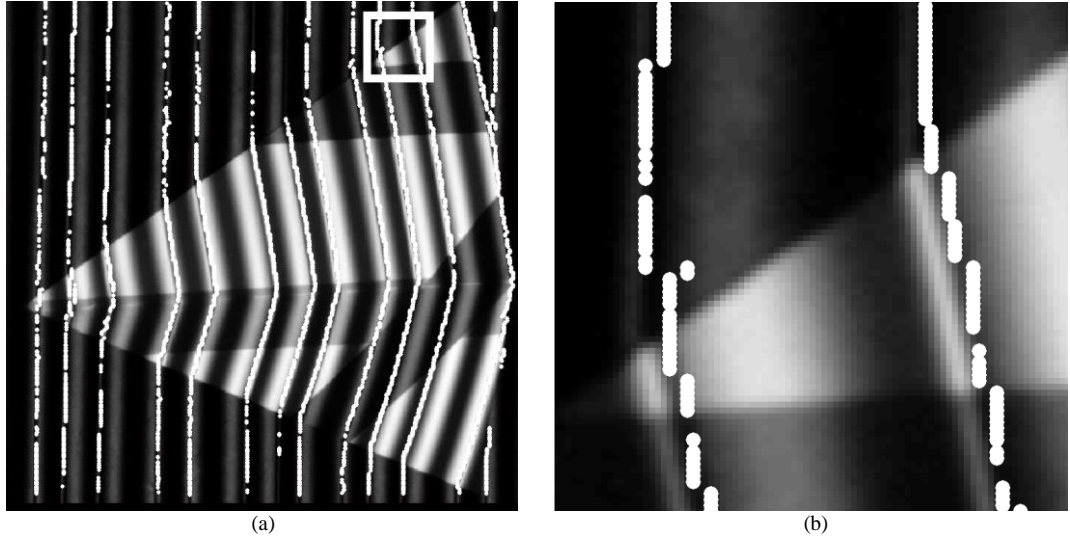


Figure 4-5. (a) Marker detection results after using the proposed thresholding method; (b) the zoom in version.

The thresholded wavelet coefficients are then used in (4-6) for computing the marker information cue  $Q$  and in turn detecting the position of the markers. The detection accuracy is greatly improved by using the abovementioned thresholding techniques based on the magnitude and relative phase of the complex wavelet coefficients. An example of the end result is shown in Figure 4-5. It can be seen that almost all maxima of noises are removed. The maxima retained clearly show the positions of the markers in the fringe image.

When the maxima of the markers are identified, the next step is to determine the period order  $k_y$  of each marker by identifying  $\theta_y$  of the marker from the fringe image (see (4-3) for the relationship between  $k_y$  and  $\theta_y$ ). To do so, we first use the flood fill algorithm [120] to find the regions in the wrapped phase map where the phase difference is bounded by  $2\pi$ . Hence within the region, the period order should be the same. Let us define  $Y_j$  to be the set of all vertical coordinate index  $y$  in such regions with  $j$  as the region index. An exhaustive search is then performed to estimate the period order  $k_y$  based on the maxima detected in region  $j$  as follows:

$$i = \min_{i'} \frac{1}{N_j} \sum_{y \in Y_j} |\tilde{\theta}_y - i' \xi| \quad (4-12)$$

$$k_{y \in Y_j} = M^{-1}\{i\xi\}$$

where  $\xi$  is defined in Section 3;  $N_j$  is the total number of maxima that can be detected in region  $j$ ; and  $\tilde{\theta}_y$  is the phase angle of the maxima in row  $y$ , which is obtained directly by inspecting the fringe image based on the maxima position indicated in  $Q$ . However, due to the various artifacts in the fringe image, the  $\tilde{\theta}_y$  obtained is always slightly different from the true  $\theta_y$ . (4-12) thus helps to identify the correct  $i$  based on  $\tilde{\theta}_y$ . Another problem when implementing (4-12) is that the flood fill algorithm may accidentally include the maxima from neighboring regions into the computation. It is particularly the case when the fringe image is of low quality. Recall that when embedding the markers, arrangement has been made to maximize the difference in  $\theta_y$  of neighboring markers. So in practice before implementing (4-12), we first carry out a screening process to all  $\tilde{\theta}_y$  such that those having large difference from the rest will be ignored. Once we get the period order  $k_y$  from (4-12), the phase unwrapping problem can be solved using (4-1) and the 3D model of the object can be readily reconstructed.

#### 4.4 SIMULATION AND EXPERIMENT RESULT

To evaluate the computational efficiency and accuracy of the proposed algorithm, a simulation using a computer generated fringe pattern was first carried out. Figure 4-6 (left) and (right) show a computer generated cone object and the deformed marker encoded fringe pattern, respectively, which were used in the simulation. They serve as the ground truth for the evaluation. To simulate the real working environment,

white Gaussian noise (variance 1.0) is added to the fringe pattern. The simulation code is written in MATLAB running on a personal computer at 3.4 GHz.

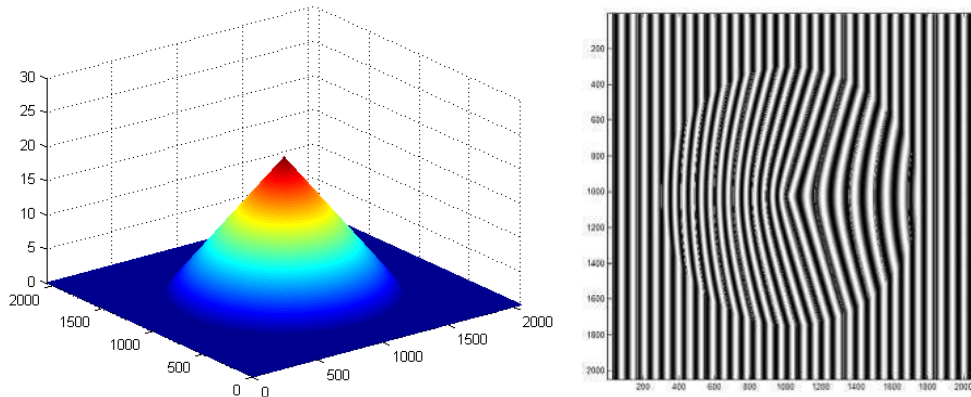


Figure 4-6. The object used in the simulation. (left) A computer generated 3D cone (ground truth); (right) the deformed fringe pattern

We compare the proposed algorithm with the traditional Window Fourier Filtering (WFF) method [62, 63] and the DTCWT method without markers embedded [67, 69]. For DTCWT, we use the filter coefficient proposed in [135]. For both approaches, the phase unwrapping is done by using the Goldstein algorithm [52]. All algorithms are implemented in MATLAB. Table 4-1 shows the comparison results in terms of the execution time and SNR at different noise levels. As shown in the table, the proposed algorithm is faster by approximately 10 times than the WFF+Goldstein method with similar, if not better, SNR. Compared to the DTCWT+Goldstein method (without markers), the proposed algorithm gives a similar performance both in the execution time and SNR. They show that the use of markers does not introduce much burden to the computation of the algorithm.

The real advantage of using markers is that it allows correct phase unwrapping even when some of the phase information is seriously corrupted or even missing. To demonstrate it, we conducted a series of experiments using real objects. More specifically, we implemented our proposed algorithm with an FPP hardware setup

that contains a DLP projector and a digital SLR camera. The projector has a 2000:1 contrast ratio with light output of 3300 ANSI lumens and the camera has a 22.2 x 14.8mm CMOS sensor and a 17-50mm lens. Both devices are connected to the computer with a 3.4GHz CPU and 16GB RAM for image processing. They are placed at a distance of 700mm-1200mm from the object.

Table 4-1. Comparison between the proposed method, the conventional DTCWT+Goldstein method, and the WFF+Goldstein method in terms of execution time and SNR

$\sigma$	Proposed		Conventional DTCWT		WFF	
	Time (s)	SNR	Time (s)	SNR	Time (s)	SNR
0.2	2.27	39.55	2.13	39.37	33.39	<b>43.12</b>
0.4	2.26	<b>38.40</b>	2.12	38.22	33.14	38.13
0.6	2.27	<b>36.95</b>	2.12	36.79	33.11	34.84
0.8	2.28	<b>35.49</b>	2.13	35.35	33.53	32.32
1	2.28	33.86	2.12	<b>33.99</b>	33.42	30.29

In our experiment, a marker encoded fringe pattern at the resolution of 1280×1024 is generated and projected onto the target object. The fringe pattern consists of about 35 sinusoids in  $x$ -direction; each has a length of 36 pixels. A marker is embedded to each sinusoid with 4 pixels width. There are 9 unique markers and repeated in every 9 sinusoids.

In the first experiment, we compare the performance of the proposed algorithm (using markers) with the conventional DTCWT+Goldstein method (without markers) in the situation that there are phase jumps in the fringe image. To create such testing environment, a paper plane and two small boxes of different height are used, as illustrated in Figure 4-7a. Basically, no fringe patterns can be found on the edges of the boxes, as shown in Figure 4-7b. Thus phase jumps are introduced to the fringe images. As shown in Figure 4-7c-f, both approaches can correctly reconstruct the

paper plane since they both use the DTCWT FPP framework as shown in Figure 2-7. However, only the proposed method can make a correct estimation of the height of the boxes. It is expected since the period order information obtained from the markers allows us to restore the unwrapped phase even when there are phase jumps in the fringe image.

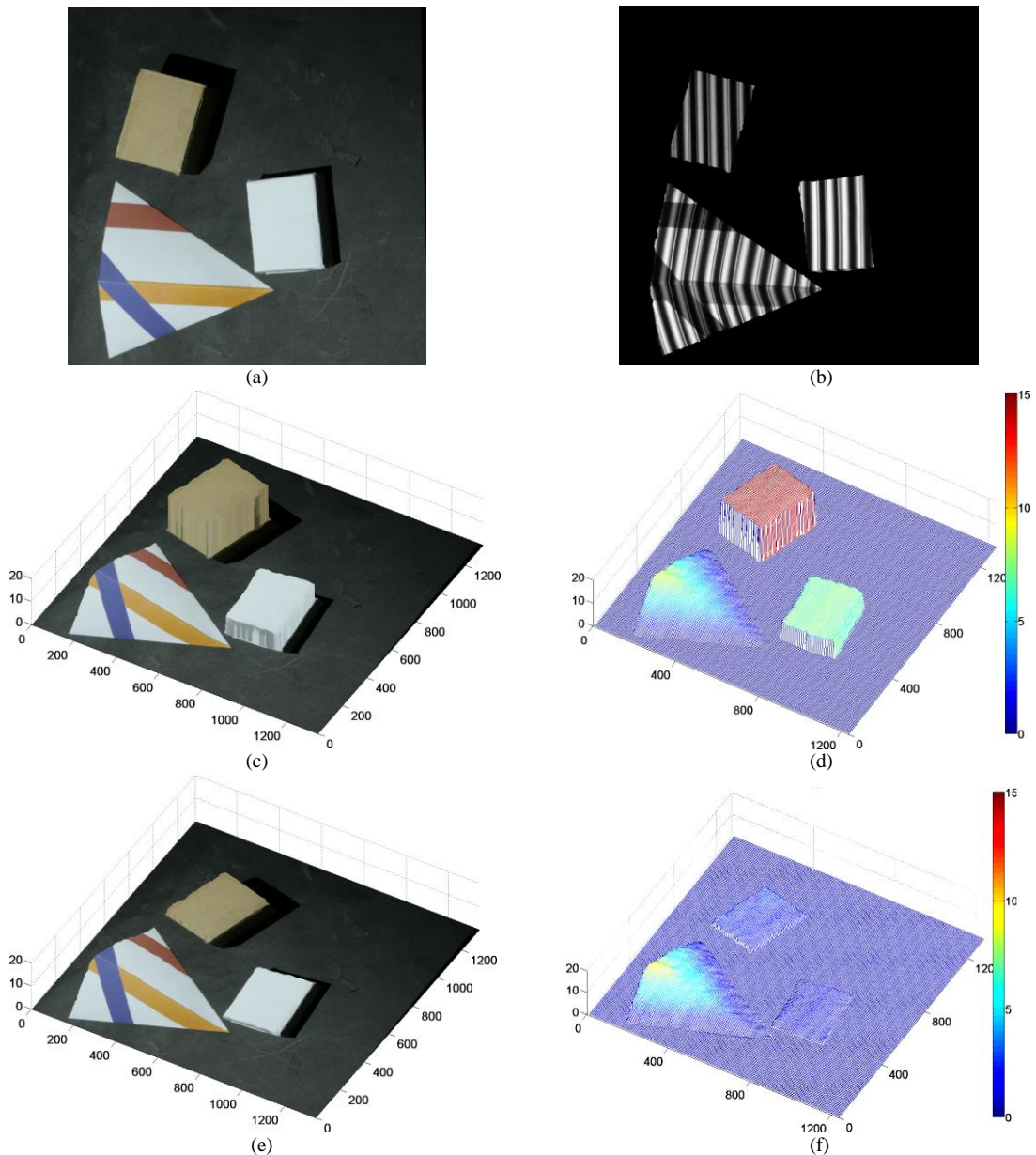


Figure 4-7. Comparison of the proposed algorithm and the traditional phase unwrapping method. (a) texture image; (b) fringe pattern illumination; (c) reconstructed 3D shape with texture using the proposed method; (d) reconstructed 3D shape with height profile using the proposed method; (e) reconstructed 3D shape with texture using the traditional DTCWT+Goldstein; and (f) reconstructed 3D shape with height profile using the traditional DTCWT+Goldstein

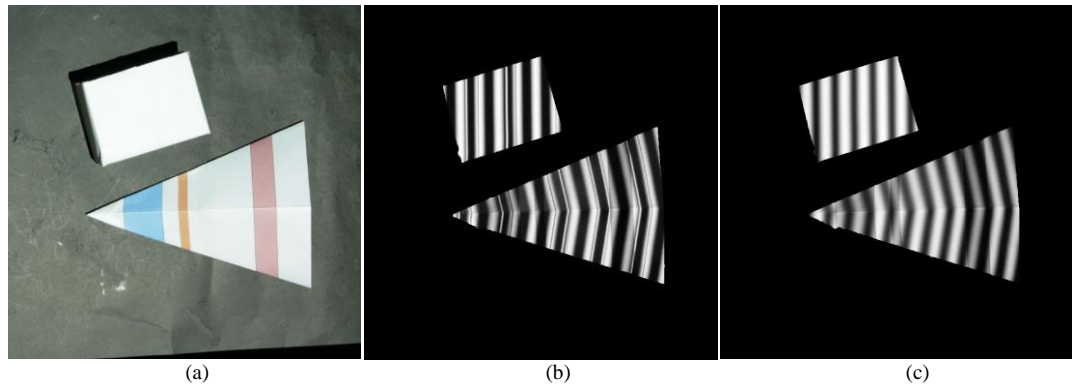


Figure 4-8. (a) Texture images (b) markers encoded fringe image; (c) one of the PMP-DF fringe images.

In the second experiment, we compare the proposed algorithm with a similar method PMP-DF [35]. The PMP-DF method uses a low frequency signal added to the high frequency fringes for embedding period order information. Thus it serves similar to the markers of the proposed algorithm. As required by PMP-DF, 6 frames of image with phase shifted sinusoidal fringes are used for the reconstruction of one 3D model. It is in contrast to the proposed algorithm which requires only 1 fringe image due to the use of the DTCWT FPP framework. Figure 4-8 shows the image of a paper plane and a box, the marker encoded fringe image used in the proposed algorithm and one of the fringe images used in PMP-DF. In this experiment, we try to test the robustness of the algorithms by changing the brightness of the fringe images. To do so, we take the fringe images using different settings of ISO and shutter speeds: low ISO (100) with shutter speed 1/15s and 1/30s, respectively; and high ISO (1600) with shutter speed, 1/80s and 1/125s, respectively. The texture images captured using high ISO setting and low ISO setting are illustrated in Figure 4-9 and Figure 4-11 respectively.

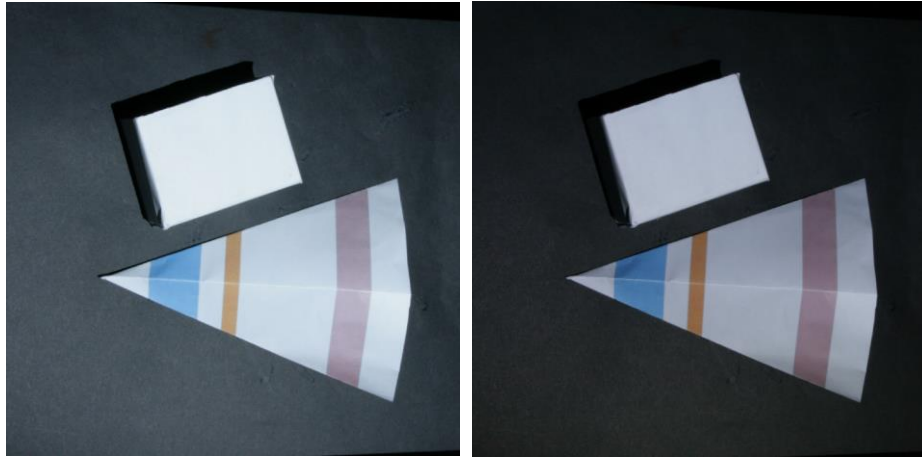


Figure 4-9. Texture images captured at low ISO (100) and different shutter speeds: (left) shutter speed 1/15s and (right) shutter speed 1/30s

At ISO 100, both approaches can generate accurate height profile when the shutter speed is set to 1/15s as shown in Figure 4-10. However when the images become darker by changing the shutter speed to 1/30s, the height profile reconstructed by PMP-DF is seriously distorted.

It is also the case when the ISO value is high (1600) as illustrated in Figure 4-12. For both shutter speeds (1/80s and 1/125s), PMP-DF generates incorrect height profile whereas the proposed method performs as usual. It can be observed that PMP-DF is sensitive to the brightness of the fringe image. When the fringe image is too dark or too bright, the low frequency signal will have its magnitude decreased or distorted. Hence the period order information it carries cannot be accurately recovered.

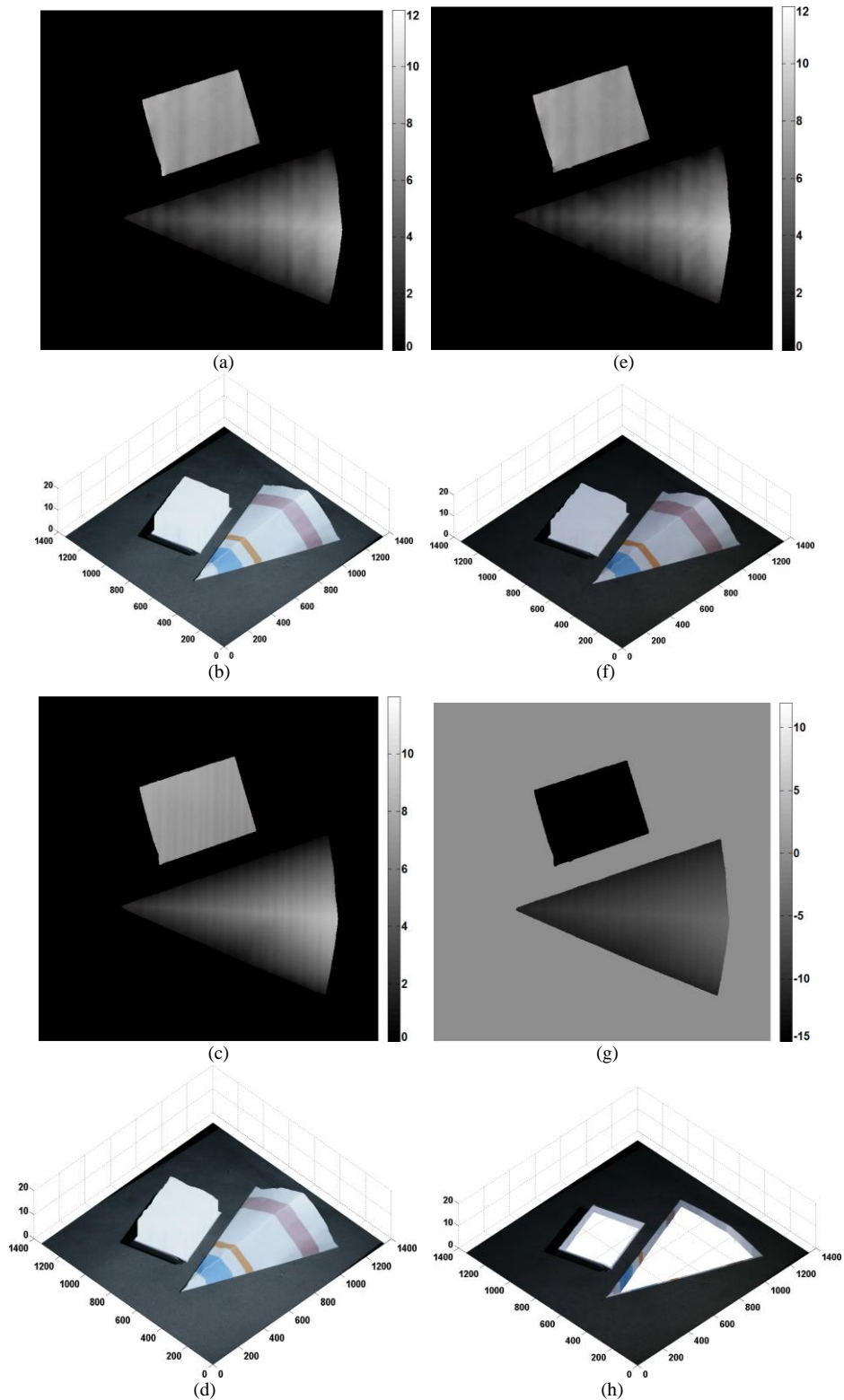


Figure 4-10. (Left column) A comparison of the proposed algorithm and PMP-DF with fringe images captured at ISO 100 and shutter speed 1/15s: (a) the height profile generated by the proposed method, (b) the 3D shape with texture generated by the proposed method, (c) the height profile generated by PMP-DF, (d) the 3D shape with texture generated by PMP-DF. (Right column) A comparison of the proposed method and PMP-DF with fringe images captured at ISO 100 and shutter speed 1/30s: (e) the height profile generated by the proposed method, (f) the 3D shape with texture generated by the proposed method, (g) the height profile generated by PMP-DF, (h) the 3D shape with texture generated by PMP-DF.

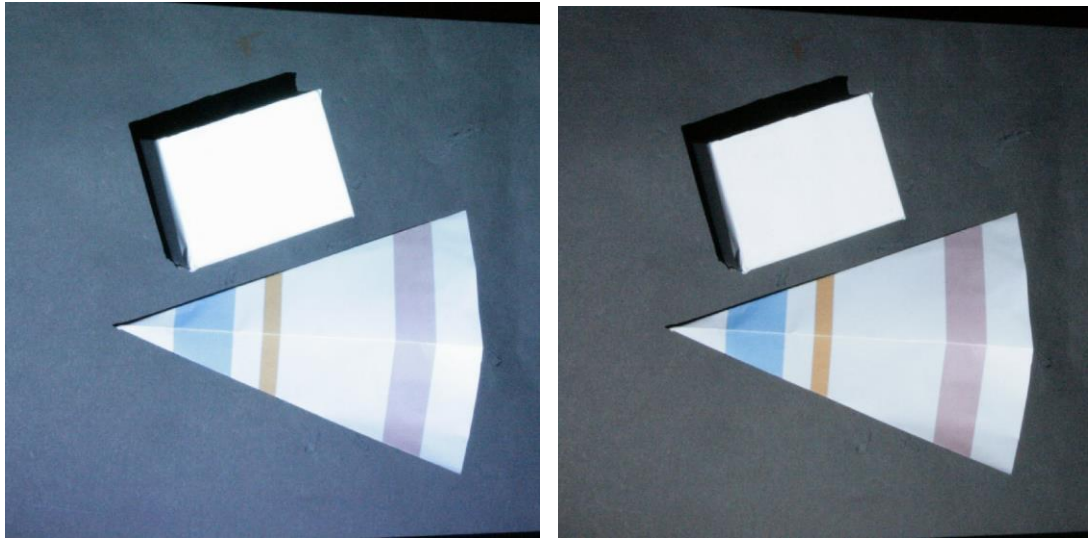


Figure 4-11. Texture images captured at high ISO (1600) and different shutter speeds: (left) shutter speed 1/80s and (right) shutter speed 1/125s.

In the final experiment, we used a free form object, a human hand. Reconstructing the 3D model of free form objects like human hands is very challenging because of the abruptly changing surface and the discontinuity around the edges. Nevertheless the proposed algorithm is able to reconstruct the 3D model satisfactorily (Figure 4-13).

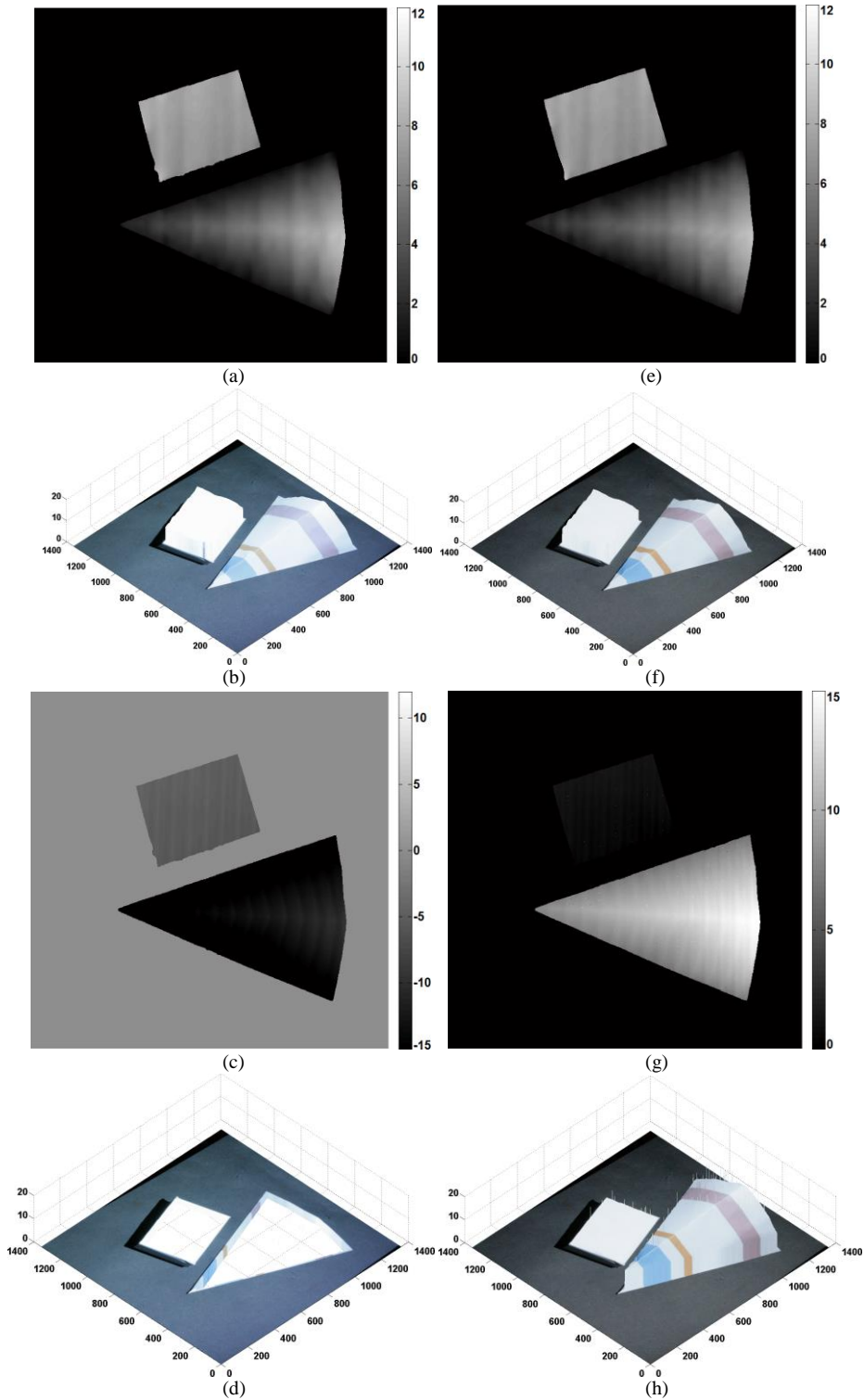


Figure 4-12. (Left column) A comparison of the proposed algorithm and PMP-DF with fringe images captured at ISO 1600 and shutter speed 1/80s: (a) the height profile generated by the proposed method, (b) the 3D shape with texture generated by the proposed method, (c) the height profile generated by PMP-DF, (d) the 3D shape with texture generated by PMP-DF. (Right column) A comparison of the proposed method and PMP-DF with fringe images captured at ISO 1600 and shutter speed 1/125s: (e) the height profile generated by the proposed method, (f) the 3D shape with texture generated by the proposed method, (g) the height profile generated by PMP-DF, (h) the 3D shape with texture generated by PMP-DF.

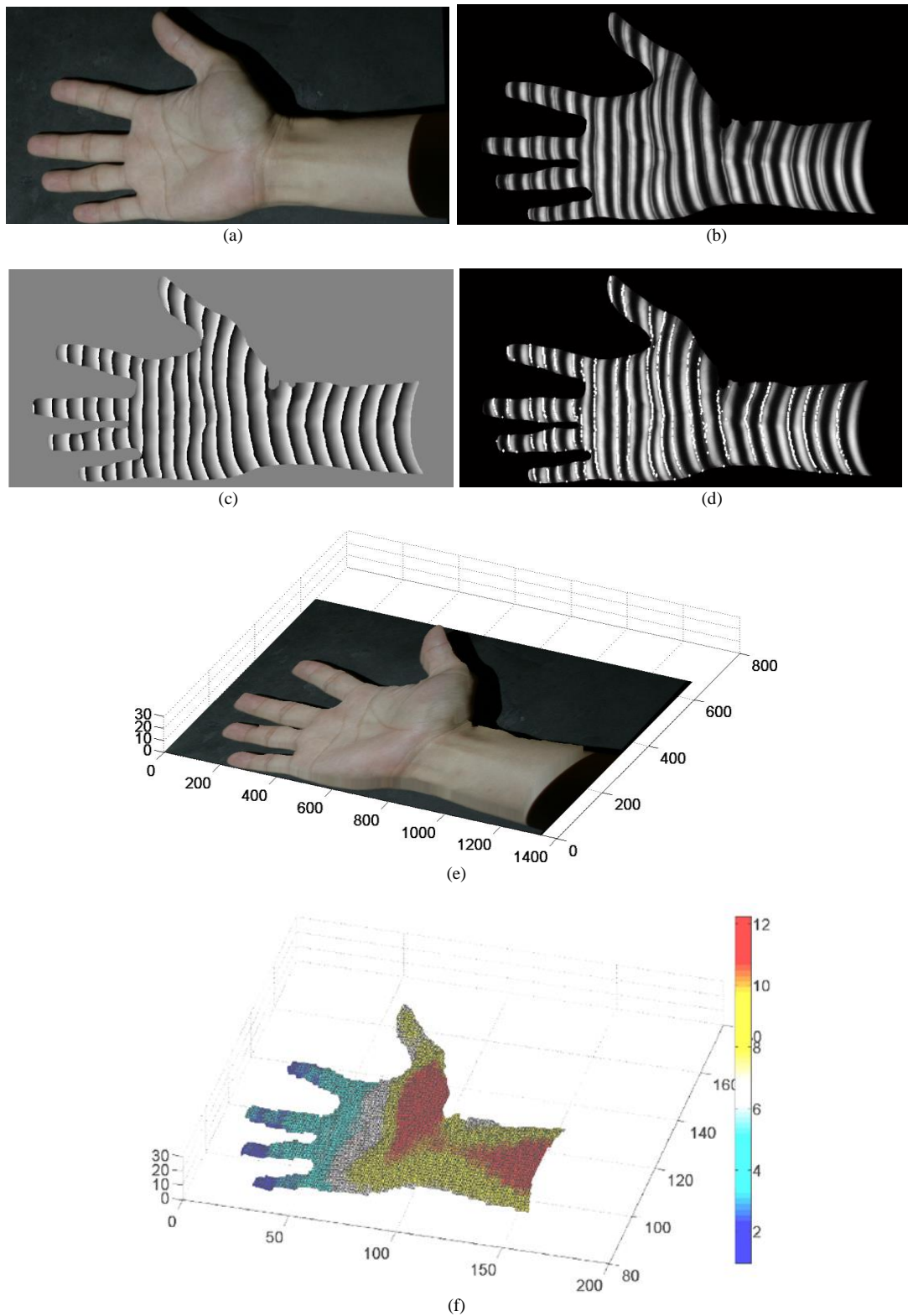


Figure 4-13. 3D model reconstruction of a human hand. (a) Texture image; (b) the fringe image; (c) wrapped phase of the hand; (d) the detected markers; (e) the reconstructed 3D model with texture image; and (f) the reconstructed 3D model.

## 4.5 SUMMARY

In this chapter, a new marker encoding and detection algorithm for the fringe projection profilometry (FPP) is proposed. Based on our previously developed dual tree complex wavelet (DTCWT) FPP framework, the proposed system can reconstruct the 3D model of an object using only one projection fringe image. The system can also handle the bias and noise problem in the image. In this chapter, a marker encoding scheme is developed to embed the period order information to facilitate phase unwrapping even when there are phase jumps in the image. Based on our proposed algorithm, the marker cue information can be extracted and the period order information can be estimated accurately. The system can be built with merely a conventional projector and a camera with no additional hardware requirement. Experimental results show that the proposed algorithm is robust to the quality of the fringe image and does not introduce much burden computationally to the original DTCWT FPP framework. However, the use of markers will in fact accumulate the detection error since the marker is rather restrictive. For instance the width of the fringes is fix and the markers are sensitive to the lens' defocus. When the number of detected markers in a particular region is small and the fringe image is of low quality, the detection error will be large. In the next chapter, the code marker approach is proposed to solve this problem.

# CHAPTER 5

## ROBUST FRINGE PROJECTION PROFILOMETRY VIA SPARSE

### REPRESENTATION

In the previous chapter, we have introduced a marker encoded FPP method which encodes the period order information based on the spatial position of the markers in the fringe pattern. Since the shape of the markers is fixed (the first derivative of an impulse), the number of unique markers that can be embedded into the fringe image is controlled by the width of the fringes. This becomes rather restrictive since the width of the fringes is fixed once the system is set up. In fact, such marker encoding scheme is similar to the time division multiplexing scheme of communication systems. And it is well known that the code division multiplexing method can often outperform the time division one in using the channel capacity. A natural question thus arises if we can borrow the idea of code division multiplexing in communication systems when designing the encoding method. More specifically, can we design a set of markers in the form of code patterns with different shapes such that they can be easily identified at the decoding stage? Such idea has an important engineering implication since in this case the number of unique markers is not solely controlled by the system set up, but also the resolvability of the decoding algorithm. Consequently, we can take advantage of the recent advance in pattern learning and

classification to help in the marker detection task. Based on the above idea, a robust code pattern encoding and decoding algorithm is proposed in this chapter. In the new algorithm, a set of textural code patterns is first designed to encode the period order information of the fringes. They are then embedded into the fringe pattern and projected onto the object. On the decoding side, the code patterns and fringe patterns are separated from the captured fringe image using a modified morphological component analysis (MCA) procedure. The resulting code patterns are then decoded by a sparse classification algorithm with dictionary learnt also via a sparse approach. By using the decoded period order information, the true phase can be obtained using the multi-level quality guided phase unwrapping algorithm. The proposed algorithm greatly improves the robustness of FPP when working with fringe images that have a complex scene, or are affected due to the ambient lighting condition.

The rest of this chapter is organized as follows. In Section 5.1, the concept of the morphological component analysis (MCA), the dictionary learning, and the sparse coding technique is presented. In Section 5.2, the proposed algorithm is discussed in detail. Finally, Section 5.3 and Section 5.4 present the experimental results and the summary of this chapter respectively. The content of this chapter is extracted from our paper published in *IEEE Transactions on Image Processing* [136].

## 5.1 BACKGROUND

We begin by introducing two important concepts that are employed in this chapter. The first concept is the morphological component analysis (MCA) which is used to separate the code patterns and the fringe patterns. The second concept is the dictionary learning and the sparse coding technique that are used to determine the period order of a code pattern.

### 5.1.1 MCA BASED ON VARIABLE SPLITTING USING SALSALSA

Given an observed signal  $G$ , which is formed by the summation of two signals  $G_1$  and  $G_2$ , i.e.  $G = G_1 + G_2$ . Assume that  $G_1$  and  $G_2$  have different morphologies. The goal of MCA is to estimate  $G_1$  and  $G_2$  by solving the following optimization problem:

$$\min_{w_1, w_2} \|G - \Phi_1 w_1 - \Phi_2 w_2\|_2^2 + \lambda_1 \|w_1\|_1 + \lambda_2 \|w_2\|_1 \quad (5-1)$$

where  $\Phi_1$  and  $\Phi_2$  are bases such that  $G_1 = \Phi_1 w_1$  and  $G_2 = \Phi_2 w_2$ . They are designed based on the criterion that both  $w_1$  and  $w_2$  are sparse. In [137],  $\Phi_1$  and  $\Phi_2$  are realized by using the rational-dilation wavelet transform (RADWT) [138] and (5-1) is solved by using an iterative thresholding procedure based on the split augmented Lagrangian shrinkage algorithm (SALSALSA) developed in [139-141]. More specifically, the problem in (5-1) can be formulated as,

$$\arg \min_w f_1(v) + f_2(w) \quad s. t. \quad v = w \quad (5-2)$$

where

$$f_1(v) = \|G - \Phi v\|_2^2, \quad f_2(w) = \lambda_1 \|w_1\|_1 + \lambda_2 \|w_2\|_1 \quad (5-3)$$

with

$$\Phi = [\Phi_1 \quad \Phi_2], \quad v = \begin{bmatrix} v_1 \\ v_2 \end{bmatrix}, \quad w = \begin{bmatrix} w_1 \\ w_2 \end{bmatrix}, \quad \lambda = \begin{bmatrix} \lambda_1 \\ \lambda_2 \end{bmatrix} \quad (5-4)$$

Then  $G_1$  and  $G_2$  can be obtained by iteratively performing the following computation.

Given the initial  $v^0$  and  $\delta^0$ ,

1.  $z^{k+1} = S_\lambda(v^k + d^k) - d^k$
2.  $d^k = \frac{1}{(\mu+2)} \Phi^T (G - \Phi z^{k+1})$
3.  $v^{k+1} = d^{k+1} + z^{k+1}$

where  $z = w - \delta$ ;  $z^{k+1}$  stands for the  $z$  at  $k + 1$  iterations; and  $S_\lambda(a)$  is the standard soft thresholding function described in (3-4). The above computation is repeated until

it is converged. Finally  $G_i = \Phi w_i^{converge}$ , where  $w_i^{converge}$  is the  $w_i$  when converges with  $i = 1, 2$ . It is shown in [137] that the algorithm can achieve the global minimum when converged.

### 5.1.2 DICTIONARY LEARNING

For the traditional dictionary learning methods, a set of training signals  $G = [g_1, g_2, \dots, g_N]$  in  $\mathbb{R}^{M \times N}$  is employed to learn an over-complete dictionary  $D \in \mathbb{R}^{M \times K}$  (hence  $K > M$ ) that can give a sparse representation  $\gamma = [\gamma_1, \dots, \gamma_N] \in \mathbb{R}^{K \times N}$  of  $G$ . The learning process can be compactly written as a minimization problem as follows:

$$\langle D, \gamma \rangle = \arg \min_{D, \gamma} \|G - D\gamma\|_2^2 \quad s.t. \quad \forall i \quad \|\gamma_i\|_0 \leq T_0 \quad (5-5)$$

where  $T_0$  is a threshold; and  $\|\cdot\|_0$  is the pseudo  $l_0$ -norm, which can be implemented by counting the number of non-zero entries. One of the popular approaches to solve the above optimization problem is the K-SVD algorithm [142]. Instead of the  $l_0$ -norm, we can also use the  $l_1$ -norm since both the  $l_0$ -norm and  $l_1$ -norm promote sparsity. When the  $l_1$ -norm is used, methods such as the basis pursuit [143] or *lasso* [144] can be used for online dictionary learning (ODL) [145].

Given a dictionary  $D$ , the sparse representation  $\gamma = [\gamma_1, \dots, \gamma_N] \in \mathbb{R}^{K \times N}$  of a signal  $G = [g_1, g_2, \dots, g_N]$  in  $\mathbb{R}^{M \times N}$  can be obtained through a process known as the sparse coding, which can be expressed as another minimization problem as follows:

$$\arg \min_{\gamma_i} \|g_i - D\gamma_i\|_2^2 \quad s.t. \quad \forall i \quad \|\gamma_i\|_0 \leq T_0 \quad (5-6)$$

(5-6) can be solved by using the orthogonal matching pursuit algorithm (OMP) [146].

Since the sparse codes of a signal can also be considered as its features, recently there are many works trying to use the dictionary learning methods in signal classification applications [147-151]. However, traditional dictionary learning

methods are for signal reconstruction purposes (such as compressive sensing). The discriminative power of the dictionaries needs to be improved for using them in classification applications. To do so, researchers developed several approaches to learn a classification-oriented dictionary in a supervised learning fashion by exploring the class label information. More specifically, denote  $W \in \mathbb{R}^{m \times K}$  to be model parameters of a given classifier which assigns the class label for a given sparse code, where  $m$  denotes the number of classes to be discriminated. Two approaches are commonly used for assigning the class labels, either by minimizing the class-specific residue [152] or by a linear classification [147, 151]. In this research, we employ the later approach.  $W$  can be jointly learned with the dictionary  $D$  based on a cost function as follows:

$$\arg \min_{D, W, \gamma} \|G - D\gamma\|_2^2 + \lambda_1 f(W) + \lambda_2 f(D) \quad s. t. \quad \forall i \quad \|\gamma_i\|_0 \leq T_0 \quad (5-7)$$

$f(D)$  denotes a function that forces the sub-dictionaries in  $D$  for different classes to be as incoherent as possible [147, 152].  $f(W)$  denotes a classifier function, e.g., a linear classifier [151], a label consistent term [147], a logistic function [148], or Fisher discrimination criterion [153]. And  $\{\lambda_i\}_{i=1,2}$  denote the regularization parameters. Comparing with (5-5), it can be seen that additional constraints are added in (5-7) for improving the discriminative power of the learned dictionary. In this work, we use a similar approach to learn a dictionary that can effectively detect the period order information of the fringe images and in turn facilitate the reconstruction of the 3D model of the object.

## 5.2 PROPOSED ALGORITHM

### 5.2.1 ENCODING OF THE PERIOD ORDER INFORMATION

Recall from Section 2.1 that the goal of FPP method is to accurately evaluate the true phase map  $\phi$  from the wrapped phase map  $\hat{\phi}$  computed from the fringe image. Once  $\hat{\phi}$  is obtained, the 3D model of the object at each scene point can be evaluated using (2-4). As mentioned in (4-1), there is a direct relationship between  $\phi$  and  $\hat{\phi}$  as follows [50]:

$$\phi = \hat{\phi} + K2\pi \quad (5-8)$$

where  $K$  is also called the K-Map. It gives the missing period order information (or the *k-value*) of  $\hat{\phi}$ . If it is known, the phase unwrapping problem is solved. The key idea of the proposed method is to encode the K-map with some unique textural patterns. They are then embedded into the fringe patterns and projected onto the object. Thus the captured fringe image can be formulated as,

$$G = G_1 + G_2 \quad (5-9)$$

where  $G_1$  denotes the original sinusoidal fringe pattern (i.e.  $G$  in (2-1)); and  $G_2$  denotes the code pattern that encodes the *k-value* defined by,

$$G_2 = M(K(\phi))$$

$$K: \mathbb{R} \rightarrow \mathbb{Z}^+ \quad (5-10)$$

$$\phi \rightarrow \left\lfloor \frac{\phi + \pi}{2\pi} - \pi \right\rfloor$$

In (5-10),  $M$  is the encoding function for each *k-value* and  $\lfloor \cdot \rfloor$  is the floor function that gives the closest smaller integer number. Hence  $G_2$  is unique for each *k-value*.

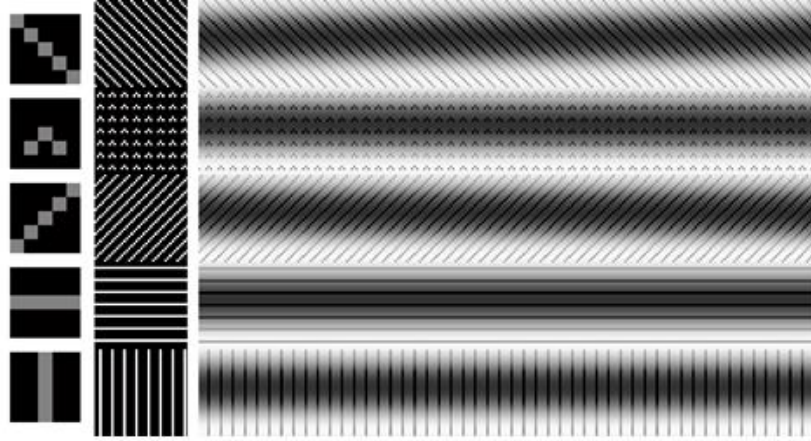


Figure 5-1. 5×5 pixels binary textons (most left), the code pattern generated by textons (second column), and the coded fringe pattern with one unique texture assigned for each  $k$ -value (column three).

When designing the encoding function  $M$ , it is important to ensure that: 1)  $M$  can generate some code patterns  $G_2$  which have different morphological structures from  $G_1$ , e.g., different shape, frequencies, colors, etc.; and 2)  $G_2$  should have a unique feature for each  $k$ -value. In this chapter, we propose to construct the code patterns by a concatenation of image patches (or textons). An example of five unique textons and their corresponding code patterns are shown in Figure 5-1. As can be seen in the figure, each texton has the size of 5x5 pixels and has a unique orientation and scale. It will give a unique response when applying to a 2D band-pass multiresolution transform filter, e.g. the Gabor filter. As shown in column 3 of Figure 5-1, one unique code pattern is assigned to each  $k$ -value of the fringe. We shall discuss in the next few sections how the  $k$ -value can be efficiently decoded by using a dictionary learning method.

### 5.2.2 OVERVIEW OF THE PROPOSED DECODING ALGORITHM

As illustrated in Figure 5-4, the proposed decoding algorithm consists of an offline stage performed during the system calibration and an online stage when the object's 3D model is actually reconstructed. At the offline stage, a large number of training fringe patterns, which have been encoded with different code patterns, are first

applied to a modified MCA procedure so that the fringe patterns and codes patterns are separated. Since the *k-values* that the represented code patterns are known, a supervised label consistent K-SVD (LC-KSVD) training process [147] can be carried out for learning a discriminative dictionary  $D$  and a linear classifier  $W$  which will be used at the online stage. Figure 5-2 illustrates the captured coded fringe pattern of a shiny flat board used for training. It should be noted that in this figure, each texton is used for three consecutive fringes and repeated every five textons. It is due to the limitation of the number of textons when high frequency fringe pattern are used (see Section 5.3 for detail description).

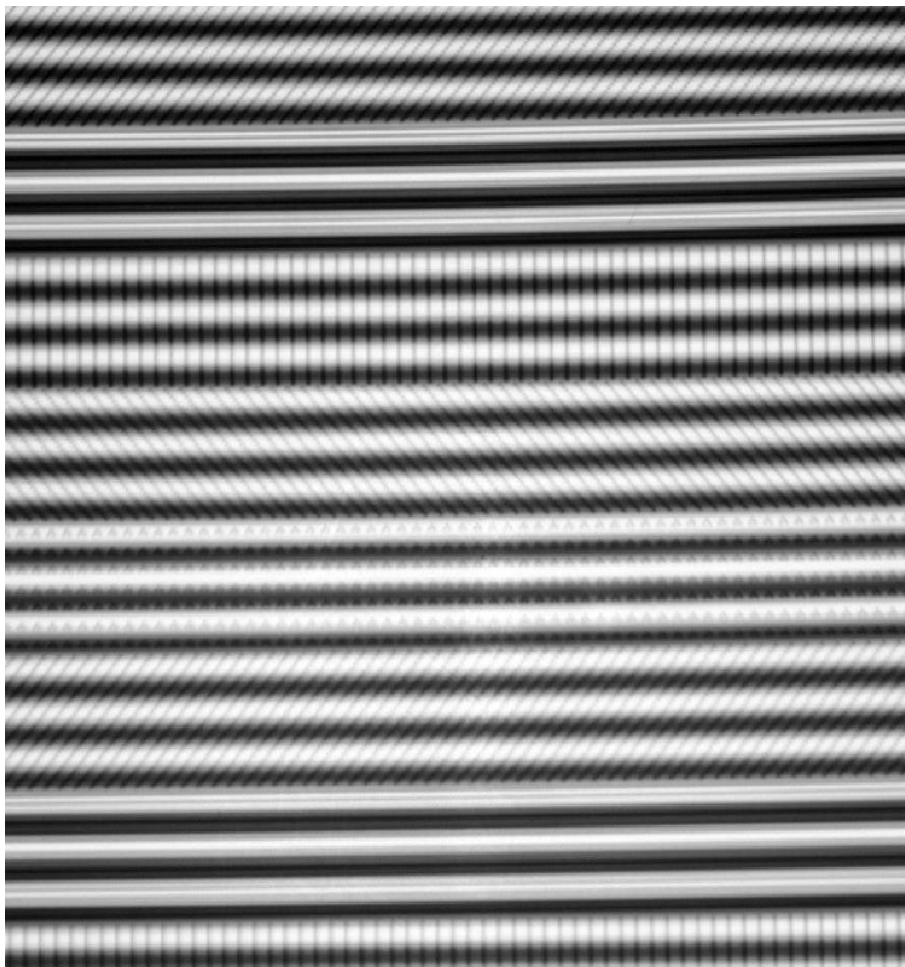


Figure 5-2. The captured coded fringe pattern of a shiny flat board

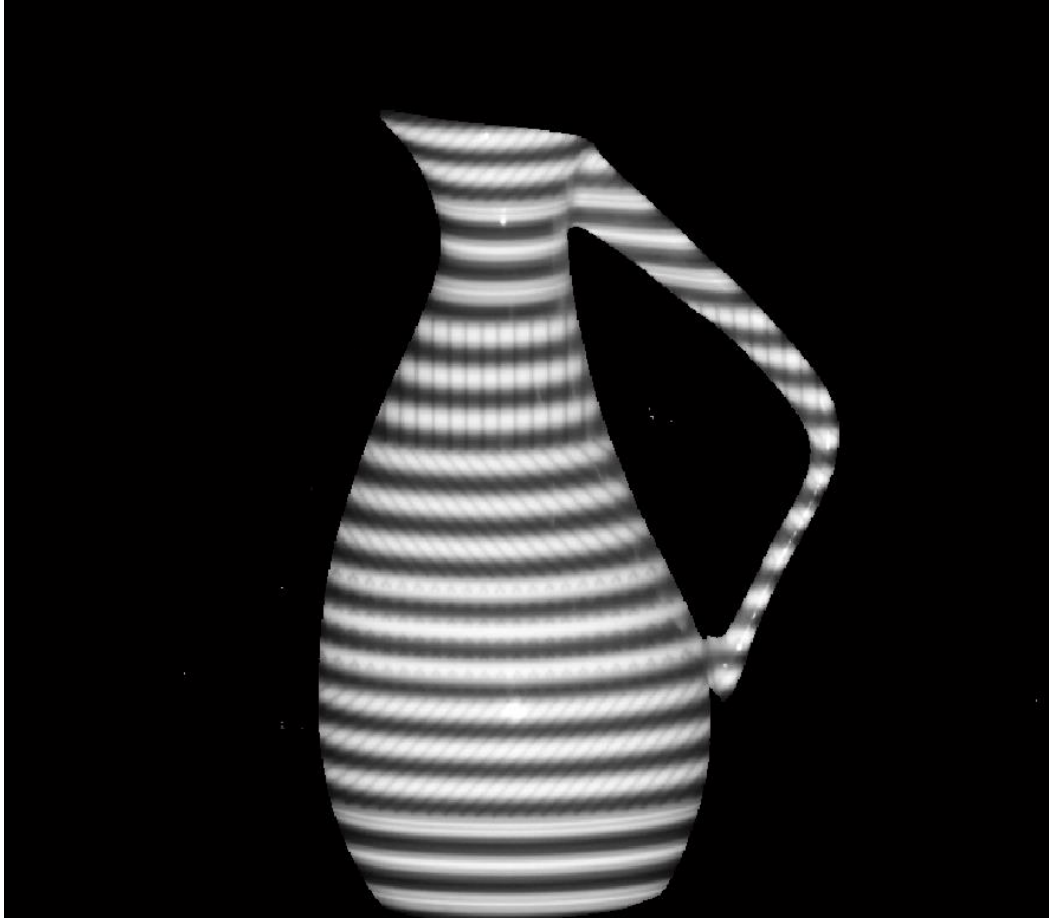


Figure 5-3. The captured coded fringe pattern of a jar

At the online stage, the encoded fringe images of the testing object are fed to a modified MCA procedure to separate the fringe patterns and the code patterns. The wrapped phase map  $\hat{\phi}$  is then computed from the fringe patterns while the *k-values* of  $\hat{\phi}$  are determined by feeding the code patterns to the discriminative dictionary  $D$  and a linear classifier  $W$  learned at the offline stage. These *k-values* thus obtained are used to guide a multilevel phase unwrapping procedure to evaluate the true phase map  $\phi$  and in turn reconstruct the 3D model of the object. Details of the algorithm will be explained in the following subsections. Figure 5-2 illustrates the captured coded fringe pattern of a jar.

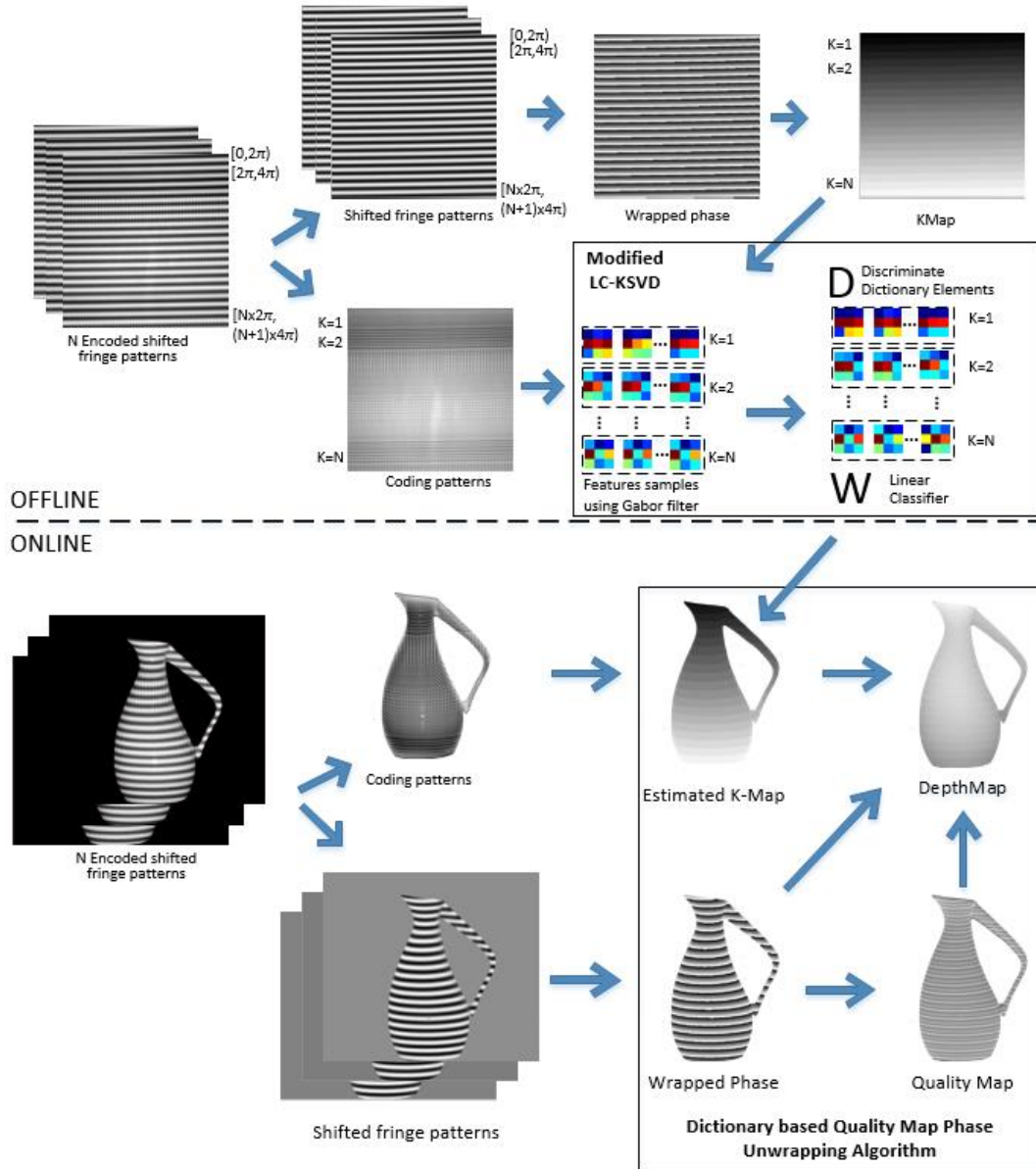


Figure 5-4. Flowchart of the proposed dictionary learning based FPP method for 3D reconstruction

### 5.2.3 THE MODIFIED MCA

For a typical FPP setup, a fringe pattern needs to go through various optical devices before being captured by the camera. Hence the captured fringe images are often noisy and blurred, which can be formulated as,

$$G = \mathcal{K}(G_1 + G_2) + \mathcal{E} \quad (5-11)$$

where  $G$  is the captured image;  $\mathcal{K}$  is the blurring kernel;  $\mathcal{E}$  is the Gaussian white noise of known variance.  $G_1$  and  $G_2$  are defined as in (2-1) and (5-10).  $G$  can be

interpreted as the convolution of the original encoded fringe pattern with the blurring kernel plus the additive Gaussian white noise.

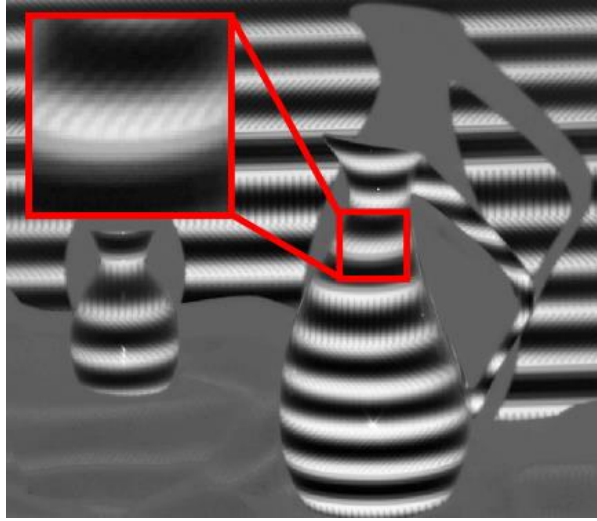


Figure 5-5. Input of the coded fringe pattern.

Given two predefined transform matrices  $\Phi_1$  and  $\Phi_2$ , the problem in (5-11) can be formulated as an optimization problem similar to (5-1) as follows:

$$\arg \min_{\alpha_1, \alpha_2} \|G - \mathcal{K}(\Phi_1 \alpha_1 + \Phi_2 \alpha_2)\|_2^2 + \lambda_1 \|\alpha_1\|_1 + \lambda_2 \|\alpha_2\|_1 \quad (5-12)$$

where  $\alpha_i$  are the sparse representations of  $\{G_i\}_{i=1,2}$  and  $\lambda_i$  are the regularization parameters. (5-12) can still be solved by using the MCA with a slight modification.

First, we employ the tuned-Q wavelet transform (TQWT) similar to that in [137, 154] for the implementation of  $\Phi_1$  and  $\Phi_2$ . They fulfill the mutual incoherence requirement and can efficiently capture the structures of interest (i.e. having sparse  $\alpha_i$ ). For performing the MCA, we first utilize the splitting variable approach. Let,

$$f_1(v) = \|G - \mathcal{K}\Phi v\|_2^2, \quad f_2(\alpha) = \lambda_1 \|\alpha_1\|_1 + \lambda_2 \|\alpha_2\|_1 \quad (5-13)$$

with

$$\Phi = [\Phi_1 \quad \Phi_2], \quad v = \begin{bmatrix} v_1 \\ v_2 \end{bmatrix}, \quad \alpha = \begin{bmatrix} \alpha_1 \\ \alpha_2 \end{bmatrix}. \quad (5-14)$$

(5-13) can be written as the following iterative optimization procedure:

Given the initial  $v^0$  and  $d^0$ ,

$$\begin{aligned}\alpha^{k+1} &= \arg \min_v \lambda_1 \|\alpha_1\|_1 + \lambda_2 \|\alpha_2\|_1 + \frac{\mu}{2} \|\alpha - v^k - d^k\|_2^2 \\ v^{k+1} &= \arg \min_v \|G - \mathcal{K}\Phi v\|_2^2 + \frac{\mu}{2} \|\alpha^{k+1} - v - d^k\|_2^2 \\ d^{k+1} &= d^k - (\alpha^{k+1} - v^{k+1})\end{aligned}\tag{5-15}$$

Since  $\Phi_1$  and  $\Phi_2$  are a tight-framed TQWT and  $\mathcal{K}$  can be assumed to be a circular convolution operation,  $\mathcal{K}$ ,  $\Phi_1$  and  $\Phi_2$  can be factorized as follows,

$$\mathcal{K} = U^T H U, \quad \Phi_i = U^T C_i U \quad \forall i \in 1, 2\tag{5-16}$$

where  $U$  represents the discrete Fourier transform (DFT),  $U^T = U^{-1}$  is its inverse ( $U$  is unitary, i.e.,  $U^T U = U^T U = I$ ) and  $H$  is the diagonal matrix of the DFT coefficients of the convolution operator,  $C$  and  $C^T$  are analysis and synthesis prior performed. As shown in appendix B, (5-15) can be simplified to the following iterative algorithm such that the fringe pattern and the embedded code pattern (i.e.  $G_1$  and  $G_2$  as defined in (5-9) and (5-10)) can be obtained from the observed blurred and noisy fringe image  $Y$ :

#### **Algorithm I: Modified MCA**

Given the initial  $v^0$  and  $d^0$

1.  $z^{(k+1)} = S_\lambda(v^{(k)} + d^{(k)}) - d^{(k)}$
2.  $v^{(k)} = \frac{1}{\mu} (I - U^T F U) (\Phi^T \mathcal{K} G + \mu z^{k+1})$
3.  $d^{(k+1)} = d^{(k+1)} - z^{(k+1)}$

For the algorithm, we assume that  $\Phi$  are in a tight frame, i.e.  $\Phi \Phi^T = 2I$ . The definition of most parameters is the same as in Section 5.1.1, except a new parameter  $F$  is introduced which is defined as follows:

$$F = C^T H^* (\mu + 2|H|^2)^{-1} H C \quad (5-17)$$

where  $H^*$  is the complex conjugate of  $H$ ;  $|H|^2$  is the squared absolute value of  $H$ ; and  $C = [C_1 \ C_2]$ . In (5-17), the expression  $H^* (\mu + 2|H|^2)^{-1} H$  is actually a Wiener filter in the frequency domain. It helps to enhance the blurred and noisy fringe image to facilitate the decomposition.

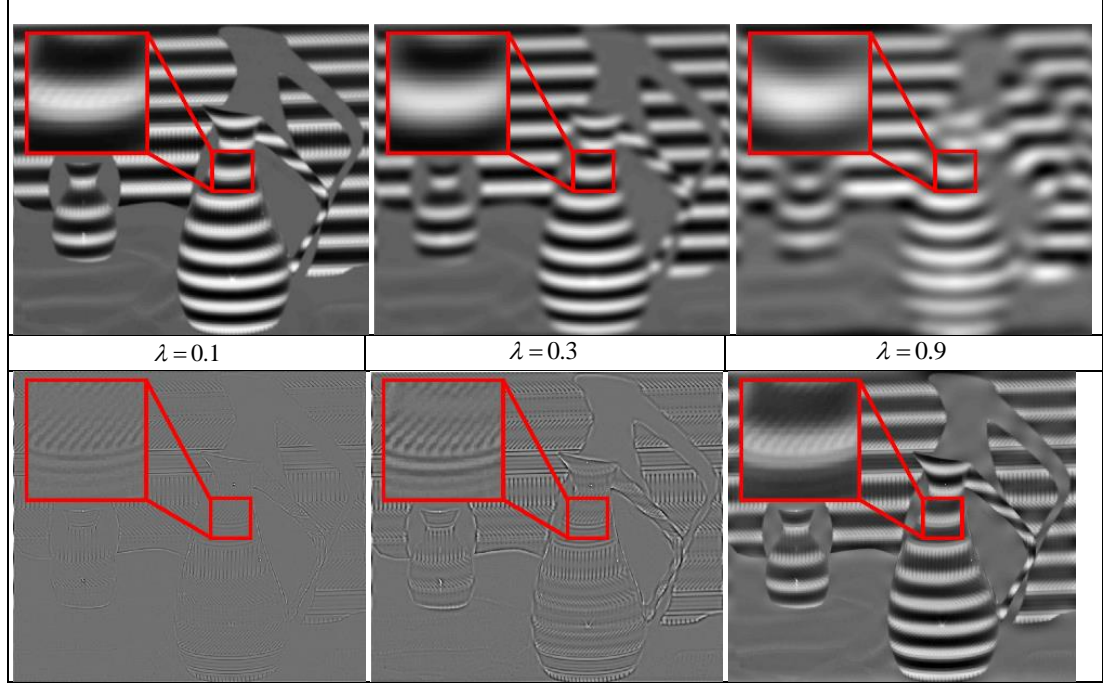


Figure 5-6. the coded fringe pattern decomposition using TQWT with different threshold value. The result of decomposition: the fringe pattern,  $G_1$  (top row) and the code pattern  $G_2$  (bottom row) with its regularization parameter  $\lambda$ .

One of the important features of **Algorithm I** is its fast computation speed. In the algorithm, the term  $\Phi^T \mathcal{K} G$  can be pre-computed before the iteration; and  $F$  can be computed efficiently since it is performed in the Fourier domain. The total computation cost is only  $O(rN \log_2 N)$ , where  $N$  is the total number of pixels of the fringe image and  $r$  is the redundancy factor which is set to 2. Figure 5-6 shows the results of using **Algorithm I** to decompose an encoded fringe image with various regularization parameter  $\lambda$ . As shown in the figure, the fringe pattern  $G_1$  and the

code patterns  $G_2$  can be clearly extracted from the encoded fringe image when  $\lambda$  is set to 0.3 ( $\lambda_1 + \lambda_2 = 1$ ). The parameter  $\lambda$  is set at the offline stage empirically.

#### 5.2.4 DICTIONARY LEARNING

In this section, we present the dictionary learning procedure and how the learned dictionary and the linear classifier are used in the  $k$ -value estimation.

##### 1) Training Set for Dictionary Learning

To construct a reliable and robust dictionary, a large number of high quality image patches is needed for the training process. For the proposed algorithm, the image patches are selected during the offline stage by first projecting the encoded fringe pattern on a flat surface and capturing the resulting fringe image following the standard FPP approach. Since the object is a flat surface, there will not be any phase jump hence all  $k$ -values can be easily determined from the fringe image. They will be used as the ground truth for training the dictionary. As mentioned above, the encoded fringe image will go through the modified MCA such that the fringe patterns and code patterns are separated. For each region  $R^k$  in the separated code pattern (where  $k$  is the  $k$ -value of that region), a set of code pattern patches and their Gabor features can be obtained. Let,

$$P^k = \{p_i^k\}_{i=1, \dots, N^k} \text{ and } \zeta^k = \{\zeta_i | \zeta = \mathcal{G}(p_i^k)\}_{i=1, \dots, N^k} \quad (5-18)$$

where  $P^k$  and  $\zeta^k$  are a patch set and a patch feature set, respectively.  $N^k$  is the number of training patches for each label in set  $P^k$ . In our experiment, we randomly select 256 patches ( $N^k = 256$ ) for each  $k$ . Suppose we have  $K$   $k$ -values, i.e.  $k = 1, \dots, K$ , the total number of training patches is  $N^k K$ .

In (5-18),  $\mathcal{G}(\cdot)$  is a function that extracts the features of a given patch. The Gabor features are obtained by convolving a patch  $p$  with a Gabor kernel of  $J$  scales, i.e.  $j = 1 \dots J$ ; and  $\theta$  orientations, i.e.  $\theta_o = 1, \dots, \theta$ . It results in a complex vector which can be written as,  $\rho_{j,\theta}^k = p^k * G_{j,\theta}$  where ‘\*’ denotes the convolution operator. The final feature set  $\zeta^k$  is formed by taking the mean of the complex vectors  $\rho_{j,\theta}^k$  of different scales and orientations defined as follows:

$$\zeta^k = \left[ \overline{|\rho_{1,1}^k|}, \dots, \overline{|\rho_{1,\theta}^k|}, \dots, \overline{|\rho_{J,1}^k|}, \dots, \overline{|\rho_{J,\theta}^k|} \right] \quad (5-19)$$

where  $\overline{|\rho|}$  is the mean of the magnitude of  $\rho$ . From our experiments, we observe that good results can be obtained by setting  $J = 3$  and  $\theta = 6$ .

## 2) *Discriminative Dictionary Learning and Linear Classifier*

To learn a discriminative dictionary  $D$ , we employ a label consistent K-SVD (version 1) [147] by minimizing the following objective function,

$$\arg \min_{D,A,\Gamma} \|Z - D\gamma\|_2^2 + \|B - A\gamma\|_2^2 \quad s.t. \quad \forall i, \|\gamma_i\|_0 \leq T \quad (5-20)$$

where  $Z = [\zeta^1, \dots, \zeta^K] \in \mathbb{R}^{\theta J \times N^k K}$  is the training feature set. Each column of  $Z$  is a patch feature  $\zeta_i^k = \mathcal{G}(p_i^k)$  with  $p_i^k \in G_2$ . As it is indicated in [147], (5-20) will learn the dictionary  $D \in \mathbb{R}^{\theta J \times L}$  which gives the sparse codes  $\gamma \in \mathbb{R}^{L \times N^k K}$  of  $Z$ . Besides, the second term of (5-20) enhances the discriminability of  $\gamma$  by minimizing the difference between the linear transformation of  $\gamma$  and a discriminative block diagonal binary matrix  $B \in \mathbb{Z}^{N^k K \times N^k K}$  defined as follows:

$$B = \begin{bmatrix} 1_{N^k \times N^k} & 0 & 0 & 0 \\ 0 & 1_{N^k \times N^k} & 0 & 0 \\ 0 & 0 & \ddots & 0 \\ 0 & 0 & 0 & 1_{N^k \times N^k} \end{bmatrix} \quad (5-21)$$

where  $1_{N^k \times N^k}$  is all-ones matrix of size  $N^k \times N^k$ . It forces the code pattern patches of the same period order  $k$  to have very similar sparse representations. It results in good classification performance even using a simple linear classifier as will be discussed below. The matrix  $D$  and  $A$  are initialized using the discrete cosine transform (DCT) basis and updated using the approach in [147].

When a discriminative sparse code of a patch is obtained, we need a classifier to determine the  $k$ -value that the code represents. As mentioned above, it is sufficient to use a linear classifier which can be obtained by solving the following minimization problem:

$$\arg \min_W \|H - W\gamma\|_2^2 + \lambda_w \|W\|^2 \quad (5-22)$$

where  $W$  is the required classifier and  $\gamma$  is obtained from (5-6);  $\lambda_w$  is a constant to control the contribution of the corresponding term; and

$$H = \begin{bmatrix} 1_{1 \times N^k} & 0 & 0 & 0 \\ 0 & 1_{1 \times N^k} & 0 & 0 \\ 0 & 0 & \ddots & 0 \\ 0 & 0 & 0 & 1_{1 \times N^k} \end{bmatrix}. \quad (5-23)$$

(5-22) has a close form solution as follows:

$$W = K\gamma^T(\gamma\gamma^T + \lambda_w I)^{-1}. \quad (5-24)$$

### 5.2.5 APPLYING TO PHASE UNWRAPPING

Both the dictionary  $D$  and the linear classifier  $W$  will be used at the online stage to determine the  $k$ -values of the code patterns. At the online stage, the input encoded fringe image will go through a modified MCA procedure so that the fringe patterns and code patterns are separated as indicated in Figure 5-4. Patches are extracted from the code patterns and their Gabor features are obtained using the same approach as in

(5-19). Given a patch feature vector  $\tilde{\zeta}$ , the following sparse coding method can be used to obtain its sparse code  $\tilde{\gamma}$ :

$$\arg \min_{\tilde{\gamma}} \|\tilde{\zeta} - D\tilde{\gamma}\|_2^2 \quad s. t. \quad \forall i, \|\tilde{\gamma}\|_0 \leq T_0. \quad (5-25)$$

(5-25) can be solved by using the OMP [146]. The  $k$ -value encoded by the code patch can be obtained by,

$$\hat{k} = \max_i(W\tilde{\gamma}) \quad (5-26)$$

where  $\max_i(W\tilde{\gamma})$  returns the index  $i$  of the coefficient in the vector  $W\tilde{\gamma}$  of which the value is the maximum.

The above sparse  $k$ -value classification algorithm can be applied to all code patches to obtain their  $k$ -value; however the process can be time consuming. We propose to apply it together with the traditional multilevel quality guided phase unwrapping algorithm [37] to achieve a higher computational efficiency. The proposed algorithm first randomly chooses a ‘‘good’’ point in the wrapped phase map  $\hat{\phi}$ . To determine if the point is ‘‘good’’, we make use of the approach given in [37] [51] as below,

$$Q_{map}(i, j) = \max\{\max\{|\Delta_{i,j}^x|, |\Delta_{i-1,j}^x|\}, \max\{|\Delta_{i,j}^y|, |\Delta_{i-1,j}^y|\}\} \quad (5-27)$$

where  $\Delta_{i,j}^x = \mathcal{W}(\hat{\phi}(i+1, j) - \hat{\phi}(i, j))$  and  $\Delta_{i,j}^y = \mathcal{W}(\hat{\phi}(i, j+1) - \hat{\phi}(i, j))$  are the wrapped phase differences in the horizontal and vertical directions;  $\mathcal{W}(\cdot)$  is the phase wrapping operator defined in (2-16). In (5-27),  $Q_{map}(i, j) \in [0, 2\pi)$  is called the quality map (or Q-map), which gives the prediction of the quality of each unwrapped phase data. Note that we consider the quality is good if the Q value is low, and vice versa.

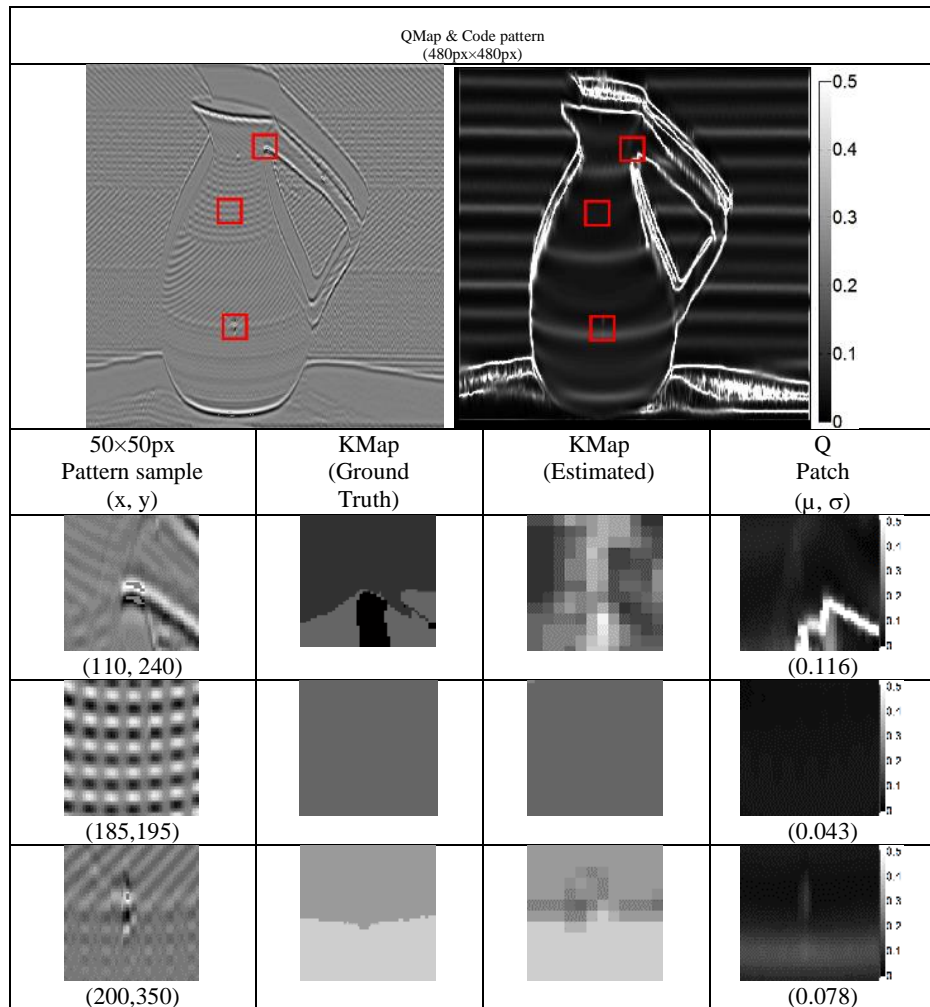


Figure 5-7. Code patterns and Q-map at various locations

Traditionally, the Q-map is used to guide the phase unwrapping process. However, we found that for a particular position where the Q-map indicates the quality is low (e.g. the Q value has a high mean), the result of *k-value* classification at that position also will not be good. An example is shown in Figure 5-7 which depicts the code patterns and Q-map obtained in an FPP experiment of an object. Three code pattern patches and Q-map patches are extracted. The sparse *k-value* classification algorithm as mentioned above is applied to each code pattern patch and the resulting K-maps are shown. For the Q-map patch centered at position  $(x, y)$ , the mean  $\mu = \overline{Q(x, y)}$  of the patches is also evaluated. In the second row, the code pattern patch and Q-map

patch are near the boundary of the object. Hence some of the Q values (fourth column) are rather high which means that they are not suitable for phase unwrapping. It can be seen that the corresponding Q-map patch has a high mean value. One can also see that the K-map estimated in the corresponding location (third column) is quite far away from the ground truth (second column). The same can be seen in the results in the final row. The code pattern patch and Q-map patch are at the location where distortion is found due to the global illumination to the object. It can be seen that the corresponding Q-map patch has a relatively higher mean value. And the K-map estimated in the corresponding location (third column) is also somewhat different from the ground truth (second column). On the contrary, the code pattern patch and Q-map patch in the third row are at the smooth region of the object. The mean of the Q-map patch is low and the K-map estimated is very close to the ground truth. The above observation is expected since for the code pattern patches located at the positions where there are abrupt changes in the fringe pattern, both the MCA and the classification algorithm, which heavily rely on the second order statistics in their optimization process, will have difficulty to obtain statistically stationary data. Hence the estimation is prone to error.

Consequently, the proposed algorithm first chooses a point  $(x, y)$  in the wrapped phase map  $\hat{\phi}$  such that the mean value of the Q-map patch at the same position, i.e.  $\overline{Q(x, y)}$ , is low. The sparse  $k$ -value classification algorithm is then applied to the code patterns to obtain the  $k$ -value at that position. Then starting from that position of the wrapped phase map, the traditional multilevel scanline phase unwrapping algorithm is used to unwrap the phase data. The whole procedure can be summarized as follows:

## Algorithm II

---

**Inputs:** The wrapped phase map  $\hat{\phi}$ , the quality map  $Q$

**Output:** The unwrapped phase map  $\phi$

---

1. **Initialize**  $minQThreshold$  with a small value
  2. **Repeat**
    - (a) Randomly select a point  $(x,y)$  where  $\overline{Q(x,y)} < minQThreshold$
    - (b) If the true phase and  $k$ -value of a neighbor of  $(x,y)$  has been obtained, directly compute  $\phi(x,y)$  and its  $k$ -value based on those of its neighbor.
    - (c) Otherwise, estimate the  $k$ -value using the proposed sparse  $k$ -value classification algorithm (i.e. (5-25) and (5-26)). Then based on the estimated  $k$ -value, compute  $\phi(x,y)$ .
    - (d) Starting from  $(x,y)$ , scan all other pixels of which the  $Q$  value also smaller than  $minQThreshold$ . Repeat step (a), (b) and (c) for all these pixels.
    - (e) If no more pixel whose  $Q$  value has a mean smaller than  $minQThreshold$ , increase the value of  $minQThreshold$  by a fixed amount.
  3. **Until** no more pixel to be unwrapped
- 

Similar to the traditional multi-level scanline phase unwrapping algorithm [37], **Algorithm II** is very simple that can be implemented with real time performance. In addition, it allows true phase estimation even when there are multiple disconnected regions in the wrapped phase map, which is common for fringe images of complex scene. In such situation, traditional algorithms such as [37] will fail since in these regions, their wrapped phase data cannot find any neighbors with known true phase or  $k$ -value hence unwrapping cannot be carried out. And since most traditional algorithms do not have the remedy such as Step 2c of **Algorithm II**, errors cannot be avoided. For **Algorithm II**, the  $k$ -value and hence the true phase in these regions can be obtained based on the sparse  $k$ -value classification algorithm. It allows the algorithm to be applicable for fringe images of complex scene. Some examples will be given in next section to illustrate the performance of the proposed algorithm.

### 5.3 EXPERIMENT

To verify the proposed algorithm, a series of FPP experiments were conducted using different real objects. To implement these experiments, an FPP hardware setup that contains a DLP projector and a digital SLR camera was adopted. The projector has a 2000:1 contrast ratio with light output of 3300 ANSI lumens and the camera has a 22.2 x 14.8mm CMOS sensor and a 17-50mm lens. Both devices were connected to a computer with a 3.4GHz CPU and 16GB RAM for image processing. They were placed at a distance of 700mm-1200mm from the object. The program code was written in MATLAB running on a personal computer at 3.4 GHz. The resolution of the testing fringe images is 728×640 pixels.

In the real working environment, FPP employs high frequency fringe pattern images. By doing so, we can reduce the influence of the global illumination. However since the number of textons is limited, each texton is used to represent several fringes. In our experiment, each texton is used to represent three consecutive fringes. To differentiate between the first, the second, and the third fringe, the phase unwrapping algorithm will check the texton of the previous and the next fringes. Hence we can increase the number of  $k$  by three times. In our experiments, five textons were used and thus 15 fringes could be employed in our FPP. This arrangement also improves the detection because the area for detection a single texton becomes larger.

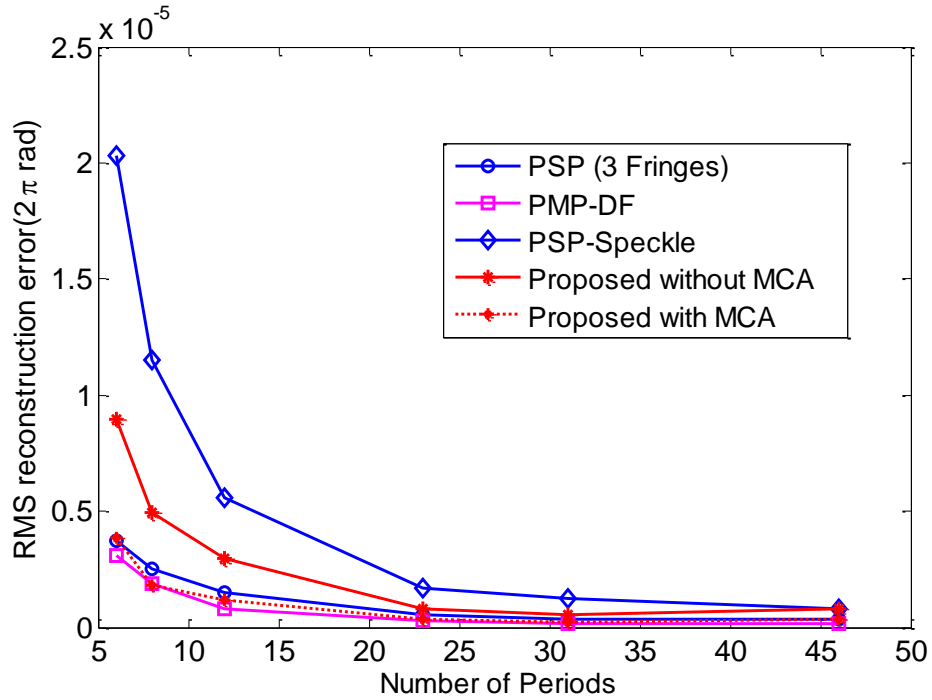


Figure 5-8. Relationship between the root mean square (RMS) reconstruction error (phase error) and the number of periods  $P$ . The number of patterns used by PMP-DF is six whereas the number of patterns used by other methods is three.

The first experiment was to reconstruct the 3D model of a shiny flat board. Since the ground truth of the flat board can be easily measured, it allows us to have an objective comparison of the accuracy of different methods. For this experiment, the size of the board is 500mm×400mm. Different methods were tested including the conventional phase shifting profilometry (PSP) with the Goldstein phase unwrapping algorithm (PSP+Goldstein) [33, 47, 52], the PSP method with speckle-embedded fringe patterns (PSP-Speckle) [39], and the proposed algorithm. All methods use three phase shifted fringe patterns to implement the PSP. While PSP+Goldstein is the conventional approach, PSP-Speckle was recently proposed and indeed similar to the proposal algorithm in the sense that it also embeds code patterns into the fringe patterns to carry the period order information. However, it does not use the MCA method to separate the code patterns and fringe patterns; and it also does not use the dictionary method to decode the code patterns. To understand the importance of the modified MCA in the proposed algorithm, we try to replace it by using the traditional

method as in PSP-Speckle, i.e. simply summing up all frames to remove the fringe pattern and obtain the code patterns. The method is then compared with the proposed algorithm and other conventional approaches. In this experiment, the flat board was scanned for 50 times using those approaches. The total number of reconstructed points is 678,665 by ignoring a few pixels at the boundary which contain some artifacts. The root means square (RMS) of the reconstruction phase error is obtained by averaging the whole surface. The comparison result is shown in Figure 5-8. As it is seen in the figure, the PSP-Speckle method shows low accuracy particularly when the number of periods is small. It is because the embedded speckles introduce distortion to the original fringe patterns that affect the accuracy. Meanwhile the accuracy of the proposed algorithm without the modified MCA only shows a slightly better performance than the PSP-Speckle method but is worse than the conventional PSP. It shows that the embedded code patterns in the proposed algorithm also introduce error to the fringe patterns similar to the PSP-Speckle method. It can affect the final result even using the learned dictionary and linear classifier in the proposed method. However once the modified MCA is applied, the phase error of the proposed algorithm is similar or even slightly better for all period numbers as illustrated in Figure 5-8. It shows that the embedded coded patterns in the proposed algorithm can be separated successfully using the modified MCA. In this experiment, we have shown that the proposed algorithm can give one of the best performances when working on fringe images of simple scene. We shall show in the next experiment that when working on complex scenes, the proposed method can tackle the ambiguity problems while the other methods fail to deliver.

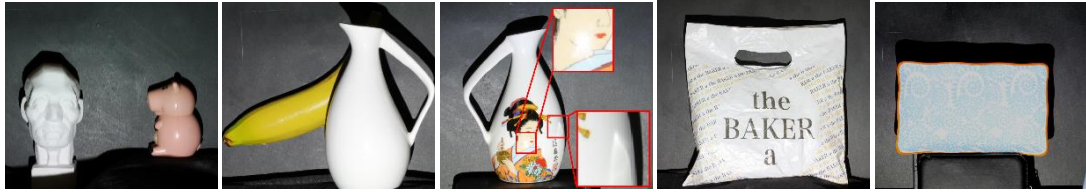


Figure 5-9. Objects that form complex scenes. (a) A head sculpture and a plastic toy; (b) a plastic banana occluded by a jar; (c) a jar with texture and highlights; (d) a plastic bag with regular textual pattern; and (e) a ceramic plate with complex texture cover the whole object.

For qualitative evaluation, objects that form a complex scene as depicted in Figure 5-9 are considered. In these scenes, highlight regions, sudden intensity jump, occlusion, or bias due to the object's texture can be found. To be specific, the first scene consists of a head sculpture and a color plastic toy. The second scene consists of a plastic banana occluded by a jar. The third scene consists of a jar with texture and highlights. The fourth consists of a plastic bag with regular textural pattern. And the last scene consists of a ceramic plate with complex texture covering the whole object.

Similar to the first experiment, we compare the proposed algorithm with the conventional method (PSP+Goldstein) [33, 38, 47, 52] and PSP-Speckle [39]. The result of the comparison is illustrated in Figure 5-10. In the figure, the ground truth is generated by scanning the scenes using 30 fringe pattern images with the period order determined manually. As shown in the figure, the resulting 3D models generated by the PSP+Goldstein method are erroneous for scene 1 and 2. When using the PSP+Goldstein method, it is traditionally assumed that a reference point (usually at the center of the image) is known so that a complete depth map can be grown from this reference point using the Goldstein method. Such assumption is valid only when there is only one object located at that reference point. For scene 1, both objects are not located at the center. And since there is no period order

information provided in the fringe images, there is no way to estimate the absolute depth of the objects. For scene 2, it is noted that the plastic banana is located at the center of the image hence its absolute depth can be obtained from the reference. However, due to the shadow of the jar, the two objects are disconnected as can be seen in the second image in Figure 5-9. Thus the depth estimation of the jar cannot be conducted through the reference at the plastic banana, and leads to the erroneous result. In practice, additional hardware setup is required to give the reference for each disconnected region (such as using some tiny markers as in [38]). Without those reference points, unsatisfactory results will be obtained as in the first two images of the first row in Figure 5-10.

Unlike the conventional PSP methods, both the PSP-Speckle method and the proposed algorithm provide the period order information and are able to obtain the true phase correctly as shown in Figure 5-10 (the second and the third row). However, the PSP-Speckle method can give erroneous results when the scene is complex. As illustrated in Figure 5-10 (the third to the fifth scene), distortion of different extents is found in the reconstructed 3D models using the PSP-Speckle method. Since the PSP-Speckle method does not have measure to remove the speckles from the fringe images, they can appear as noises in the reconstructed 3D model. Such noises may not only affect the smoothness of reconstructed 3D model surface, sometimes they can lead to erroneous reconstruction particularly in the regions where the fringe images have other artifacts, such as highlights (see the results of the third scene in the third column of Figure 5-10).

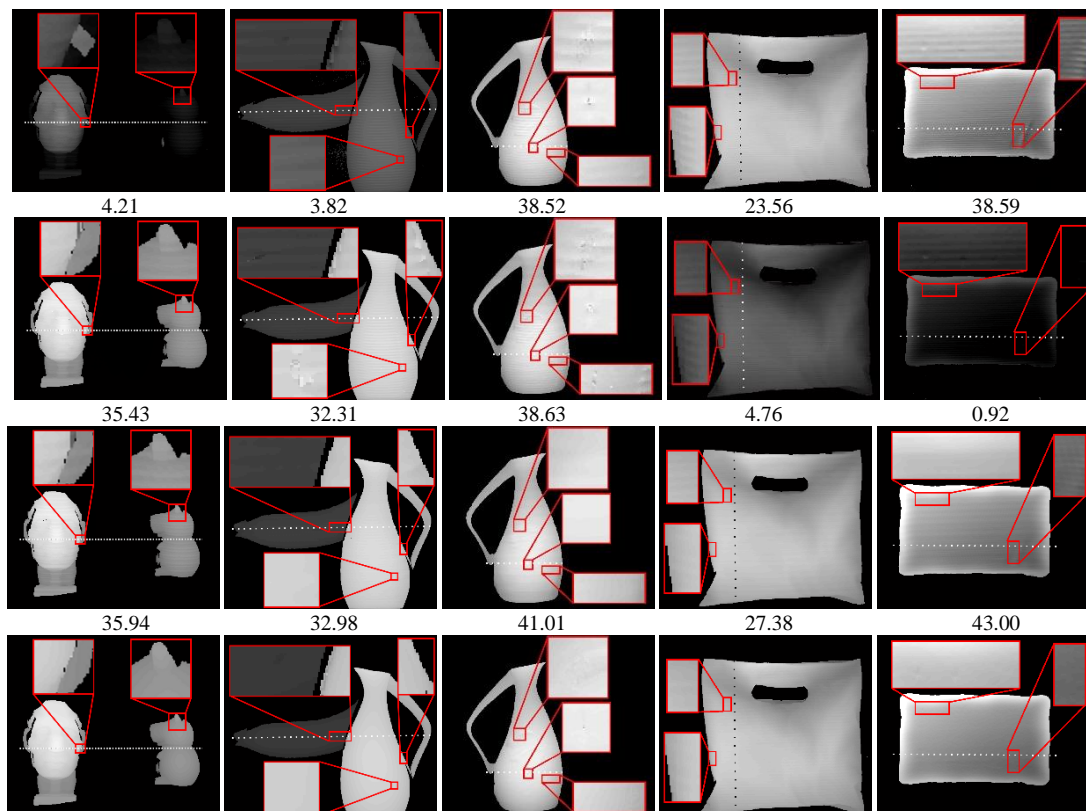


Figure 5-10. 3D reconstruction of various complex scenes with multiple objects, occlusion, highlight regions, and textures. (First row) Results of the conventional PSP+Goldstein method; (second row) results of the PSP-Speckle method; (third row) results of the proposed method; and (fourth row) the ground truth. The numbers under the images of the first 3 rows are the SNR (in dB) as compared with the ground truth.

Besides, incorrect period order information is generated when the object itself contains large textural pattern (such as the fourth and the fifth scene). They are confused with the speckles and lead to the erroneous k-value estimation as shown in Figure 5-10 (second row, fourth and fifth columns). The same problem does not exist for the proposed algorithm since, by using the modified MCA, the code pattern can be effectively separated from the textural pattern of the object, as they have different morphological structures. Together with the dictionary learning method which significantly enhance the classification power, the proposed algorithm (the third row) can accurately recover the 3D model of objects and the results are close to the ground truth (as can be seen in the images in the third row of Figure 5-10). More experimental results are shown in Figure 5-11. They show the robustness of the proposed algorithm.



Figure 5-11. A scene of complex objects (the first column). Result of 3-D reconstruction using the proposed algorithm (second column). The top view of 3D reconstruction (the last column).

## 5.4 SUMMARY

In this chapter, we have presented a robust algorithm for fringe projection profilometry (FPP). The proposed approach solves the ambiguity problem by embedding codes patterns which carry the period order information to the fringe patterns. Unlike the traditional approaches, the proposed algorithm does not require special hardware setup or projecting additional fringe patterns. When comparing with the marker approach in Chapter 4, the implementation of the proposed algorithm in this chapter is more flexible since the number of unique markers is not only controlled by the system setup but also the resolvability of the decoding algorithm. There can then be many possibilities and different methods can be used to optimize the performance of FPP in different applications. For the proposed algorithm, we adopt a modified morphological component analysis (MCA) for separating the code patterns and the fringe patterns; and a sparse dictionary learning and classification procedure for determining the  $k$ -values from the extracted code patterns. They are integrated to a multilevel quality guide phase unwrapping procedure to allow the phase unwrapping to be carried out in fringe images of complex scene. Experimental results have demonstrated the superiority of the proposed algorithm over the traditional approaches in terms of robustness and accuracy. The proposed algorithm

only requires approximately 300ms when running on a normal personal computer in the Matlab environment. We believe the computational efficiency can be further increased when working in industrial-grade computing systems.

# CHAPTER 6

## CONCLUSIONS AND FUTURE WORKS

In this chapter, we conclude this research and discuss possible extension works of this research in the future.

### 6.1 CONCLUSIONS

The general objective of this research is to develop robust FPP methods that can function effectively in adverse working environments. While there can be many problems in practical working environments, we have focused on those that are often encountered when the target objects form a complex scene. By complex scenes, we refer to the situation that the captured fringe images contain one or more of the following: (i) high noise level in the dark regions of the image; (ii) bias due to the texture and coloration of the objects; (iii) reflection due to strong global illumination; (iv) sudden intensity change due to the discontinuities or sharp structural changes of the objects; and (v) occlusion due to multiple objects. Such kind of fringe images are often obtained in real working environments, and we have demonstrated in the last few chapters that serious distortion will be resulted in the final reconstructed 3D model if they are not carefully taken care of.

The general strategy that we have adopted for achieving the objective of this project can be summarized into the following two points:

- Develop efficient and effective methods to enhance the captured images which are affected by the interference in the working environment.
- Develop good projection methods so that the projection patterns can be robustly detected despite of the possible artifacts in the captured images introduced by the working environment.

More specifically, the following three algorithms have been developed and they are the major contributions of this research work:

**1. Developed an iterative regularization inpainting algorithm to regenerate the missing fringes due to the specular highlights.**

In this research work, we have developed an iterative regularization algorithm for inpainting fringe patterns washed out by the specular highlights due to the global illumination. The proposed method is realized using the 2D-DTCWT which has the nearly shift invariant and minimum aliasing properties. Based on these properties, two highlight detection approaches are developed for finding the affected area automatically. The highlight region can be detected accurately by thresholding the smoothed fringe pattern image. The threshold value is estimated using the Gaussian mixture model (GMM). Besides, the proposed algorithm also generates the geometric structure to initialize the inpainting algorithm such that the iterative regularization process will converge to the global minimum. The simulation and experimental results show that the proposed inpainting method can regenerate accurate fringe patterns which are washed out by strong specular highlights of large size.

**2. Developed a marker encoded fringe pattern and a period order estimation algorithm for solving the ambiguity problem of FPP.**

A novel marker encoding algorithm has been specifically designed for fringe patterns so as to carry the period order information and in turn assist the phase unwrapping process. The markers are a set of impulse functions embedded at different spatial positions of the fringe pattern. They are resistive to the ambient illumination and has a low sensitivity to the surface reflectivity variations of the object. Hence they can be easily detected from the fringe image. Since the proposed algorithm is developed under the DTCWT FPP framework, it can be applied to FPP systems using a single fringe pattern (such as FTP) and for objects with color texture. Based on the embedded markers, the robustness of the original DTCWT framework is further improved such that it performs equally well with fringe images having a complex scene (e.g. multiple objects). It has a low computational complexity that does not introduce much burden computationally to the original DTCWT framework. The above has been fully demonstrated in the simulation and experimental results.

**3. Developed a robust FPP method via dictionary learning and sparse classification for accurate 3D shape measurement of a complex scene.**

Rather than using markers of fixed shape, a code patterns encoding and decoding algorithm is developed for robust FPP. Similar to the fixed marker approach, the proposed algorithm can reconstruct the 3D model of objects that form a complex scene (such as containing multiple objects, occlusions, and having sudden changes in light intensity). However, the proposed algorithm relieves the restriction that the number of unique markers does not control solely by the system setup, but also the resolvability of the decoding algorithms. In the proposed FPP method, two main approaches are adopted to

develop the decoding system, namely, 1) a modified MCA for separating the code pattern and the fringe pattern and 2) the dictionary learning and the sparse classification procedure for determining the *k-values* from the extracted code pattern. They are integrated into a multilevel quality guided phase unwrapping procedure to estimate the true phase value. The experimental results show that the proposed algorithm can recover the 3D model of objects that form a complex scene accurately and efficiently. It only requires approximately 300ms when running on a personal computer. We believe the computational efficiency can be further increased when working in industrial-grade computing systems.

Each algorithm as mentioned above has been extensively verified by numerous simulation and experiment results. We can conclude that the objective of this research has been fully achieved.

## 6.2 FUTURE WORKS

FPP methods face a fundamental trade-off between temporal and spatial resolutions. While it is well known that a more accurate 3D model can be obtained by projecting more fringe patterns, the time required for doing so limits its application to dynamic applications where the target objects are moving in time. One solution is to develop more robust reconstruction algorithms which we have demonstrated in this thesis. Another possible solution is to increase the speed of projection and imaging, e.g. using high speed cameras and projectors, which however will incur high hardware cost. Meanwhile, in the photography imaging area, there have been some techniques that allow sampling, representing, and reconstructing the space-time volume efficiently to achieve the high speed photography using only a consumer camera

[155]. In the future, a similar approach can be applied to FPP by capitalizing good sampling and sparse representation techniques such that many fringe patterns can be represented by only a small amount of patterns (and ultimately, a single pattern) and projected to the objects. Hence, without additional hardware costs, many fringe images can be obtained within a short period of time such that accurate 3D models can be reconstructed even when the objects are moving. We believe that it is a very interesting research direction since it will integrate a few currently hot research topics in signal processing, such as compressive sensing, sparse representation, 3D image coding, etc. into an important optical engineering problem. It is believed to draw a lot of attention from the signal processing and optical engineering communities and fruitful results are expected.

## APPENDIX A

Prove: Given  $N_m$  is an odd integer, show that the mapping function in (4-3) ensures neighboring markers will have a difference in  $\theta_y(k_y)$  with value at least  $\frac{(N_m-1)\pi}{N_m}$ .

Proof: It is given in (4-3) that

$$\begin{aligned}\theta_y(k_y) &= M \left( \left\langle k_y \right\rangle_{N_m} \right) = \left\langle \left\langle k_y \right\rangle_{N_m} \cdot \frac{N_m+1}{2} \right\rangle_{N_m} \cdot \frac{2\pi}{N_m} \\ &= \left\langle k_y \cdot \frac{N_m+1}{2} \right\rangle_{N_m} \cdot \frac{2\pi}{N_m}\end{aligned}$$

Hence the neighboring marker for the period  $k_y+1$  will have,

$$\theta_y(k_y+1) = \left\langle (k_y+1) \cdot \frac{N_m+1}{2} \right\rangle_{N_m} \cdot \frac{2\pi}{N_m}$$

Let

$$\left\langle (k_y+1) \cdot \frac{N_m+1}{2} \right\rangle_{N_m} = a \quad \text{and} \quad \left\langle (k_y) \cdot \frac{N_m+1}{2} \right\rangle_{N_m} = b$$

Since  $N_m$  is odd,  $a$  must be either greater than or smaller than  $b$ .

If  $a > b$  then  $N_m > a - b > 0$ . Then

$$\begin{aligned}\frac{2\pi}{N_m}(a-b) &= \frac{2\pi}{N_m} \langle a-b \rangle_{N_m} \\ &= \frac{2\pi}{N_m} \left\langle \left\langle (k_y+1) \cdot \frac{N_m+1}{2} \right\rangle_{N_m} - \left\langle (k_y) \cdot \frac{N_m+1}{2} \right\rangle_{N_m} \right\rangle_{N_m} \\ &= \frac{2\pi}{N_m} \left\langle (k_y+1) \cdot \frac{N_m+1}{2} - (k_y) \cdot \frac{N_m+1}{2} \right\rangle_{N_m} \\ &= \frac{2\pi}{N_m} \left\langle \frac{N_m+1}{2} \right\rangle_{N_m} = \frac{2\pi}{N_m} \frac{N_m+1}{2} = \frac{(N_m+1)\pi}{N_m}\end{aligned}$$

If  $b > a$  then  $N_m > b - a > 0$ . Then

$$\begin{aligned}
\frac{2\pi}{N_m}(b-a) &= \frac{2\pi}{N_m} \langle b-a \rangle_{N_m} \\
&= \frac{2\pi}{N_m} \left\langle \left\langle (k_y) \cdot \frac{N_m+1}{2} \right\rangle_{N_m} - \left\langle (k_y+1) \cdot \frac{N_m+1}{2} \right\rangle_{N_m} \right\rangle_{N_m} \\
&= \frac{2\pi}{N_m} \left\langle (k_y) \cdot \frac{N_m+1}{2} - (k_y+1) \cdot \frac{N_m+1}{2} \right\rangle_{N_m} \\
&= \frac{2\pi}{N_m} \left\langle -\frac{N_m+1}{2} \right\rangle_{N_m} = \frac{2\pi}{N_m} \left\langle N_m - \frac{N_m+1}{2} \right\rangle_{N_m} \\
&= \frac{2\pi}{N_m} \frac{N_m-1}{2} = \frac{(N_m-1)\pi}{N_m}
\end{aligned}$$

Since  $\frac{(N_m-1)\pi}{N_m} < \frac{(N_m+1)\pi}{N_m}$ , the statement is proved.

(Q.E.D.)

## APPENDIX B

Consider the minimization problem as stated in (5-12),

$$\arg \min_{\alpha_1, \alpha_2} \|G - \mathcal{K}(\Phi_1 \alpha_1 + \Phi_2 \alpha_2)\|_2^2 + \lambda_1 \|\alpha_1\|_1 + \lambda_2 \|\alpha_2\|_1$$

Applying the variable splitting method, the above problem can be reformulated as,

$$\arg \min_{v, \alpha} f_1(v) + f_2(\alpha) \quad s. t. \quad v = \alpha$$

where

$$f_1(v) = \|G - \mathcal{K}\Phi v\|_2^2, \quad f_2(\alpha) = \lambda_1 \|\alpha_1\|_1 + \lambda_2 \|\alpha_2\|_1$$

$$\Phi = [\Phi_1 \quad \Phi_2], \quad v = \begin{bmatrix} v_1 \\ v_2 \end{bmatrix}, \quad \alpha = \begin{bmatrix} \alpha_1 \\ \alpha_2 \end{bmatrix}, \quad \lambda = \begin{bmatrix} \lambda_1 \\ \lambda_2 \end{bmatrix}$$

Using the augmented Lagrangian method (ALM), the solution of the above problem can be written as an iterative algorithm as follows:

**Initialize**  $k \leftarrow 0, \mu > 0, d^0$ , and  $v^0$

**Repeat**

$$\alpha^{k+1} \leftarrow \arg \min_{\alpha} \lambda_1 \|\alpha_1\|_1 + \lambda_2 \|\alpha_2\|_1 + \frac{\mu}{2} \|\alpha - v^k - d^k\|_2^2$$

$$v^{k+1} \leftarrow \arg \min_v \|G - \mathcal{K}\Phi v\|_2^2 + \frac{\mu}{2} \|\alpha^{k+1} - v - d^k\|_2^2$$

$$d^{k+1} \leftarrow d^k - (\alpha^{k+1} - v^{k+1})$$

$$k \leftarrow k + 1$$

**Until** meet the stopping criteria

In the above algorithm, line 3 can be solved using the soft-thresholding while line 4 is a least squares problem which can be solved in its explicit form. By substituting  $z = \alpha - d$ , the above algorithm can be rewritten as,

**Initialize**  $k \leftarrow 0, \mu > 0, d^0$ , and  $v^0$

**Repeat**

$$z^{k+1} \leftarrow S_{\lambda/\mu}(v^k + d^k) - d^k$$

$$v^{k+1} \leftarrow (\Phi^T \mathcal{K}^T \mathcal{K} \Phi + \mu I)^{-1} (\Phi^T \mathcal{K}^T G + \mu z^{k+1})$$

$$d^{k+1} = v^{k+1} - z^{k+1}$$

$$k \leftarrow k + 1$$

**Until** meet the stopping criteria

where  $S_x(y)$  is the soft-thresholding of  $y$  with a threshold  $x$ . Now let us focus on the first term in line 4 of the above algorithm. Since we adopt a tunable Q-factor wavelet

transform (TQWT) which has a tight frame ( $\Phi_i \Phi_i^T = I$ ) for both  $\Phi_1$ , and  $\Phi_2$ , we have:

$$\Phi \Phi^T = [\Phi_1 \quad \Phi_2] \begin{bmatrix} \Phi_1 \\ \Phi_2 \end{bmatrix} = 2I$$

Thus applying the Sherman-Morrison-Woodbury matrix inversion lemma to the first term in line 4, we have

$$(\Phi^T \mathcal{K}^T \mathcal{K} \Phi + \mu I)^{-1} = \frac{1}{\mu} (I - \Phi^T \mathcal{K}^T (\mu I + 2\mathcal{K} \mathcal{K}^T)^{-1} \mathcal{K} \Phi)$$

Also, since the TQWT is adopted,  $\Phi_1$  and  $\Phi_2$  can be implemented efficiently in the Fourier domain. Assume that  $\mathcal{K}$  can be approximated as a circular convolution operator. Then  $\mathcal{K}, \Phi_1$ , and  $\Phi_2$  can be factorized as,

$$\mathcal{K} = U^T H U, \quad \Phi_i = U^T C_i U, \quad \Phi_i^T = U^T C_i^T U, \quad \forall i \in 1, 2$$

where  $U$  represents the discrete Fourier transform (DFT),  $U^T = U^{-1}$  is its inverse;  $H$  and  $C_i$  are some diagonal matrices. Therefore the above terms can be written as,

$$\begin{aligned} & \Phi^T \mathcal{K}^T (\mu I + 2\mathcal{K} \mathcal{K}^T)^{-1} \mathcal{K} \Phi \\ &= U^T C_i^T H^* U (\mu U^T U + 2U^T H H^* U)^{-1} U^T H C_i U \\ &= U^T \underbrace{C_i^T H^* (\mu + 2|H|^2)^{-1} H C_i}_F U \end{aligned}$$

where  $H^*$  is the complex conjugate of  $H$ ;  $|H|^2$  is the squared absolute values of the entries of the diagonal matrix  $H$ ; and  $C = [C_1 \quad C_2]$ . By substituting the above term to the algorithm, **Algorithm I** is obtained as follows:

**Initialize**  $k \leftarrow 0$ ,  $\mu > 0$ ,  $d^0$ , and  $v^0$

**Repeat**

$$z^{k+1} \leftarrow S_{\lambda/\mu}(v^k + d^k) - d^k$$

$$v^{k+1} \leftarrow \frac{1}{\mu} (I - U^T F U) (\Phi^T \mathcal{K}^T G + \mu z^{k+1})$$

$$d^{k+1} = v^{k+1} - z^{k+1}$$

$$k \leftarrow k + 1$$

**Until** meet the stopping criteria

(Q.E.D.)

## REFERENCES

- [1] B. Shi, B. Zhang, F. Liu, J. Luo, and J. Bai, "360° Fourier Transform Profilometry in Surface Reconstruction for Fluorescence Molecular Tomography," *IEEE J. Biomed. Health Inform.*, vol. 17, pp. 681-689, 2013.
- [2] R. R. Garcia and A. Zakhor, "Consistent Stereo-Assisted Absolute Phase Unwrapping Methods for Structured Light Systems," *IEEE J. Sel. Topics Signal Process.*, vol. 6, pp. 411-424, 2012.
- [3] F. Sadlo, T. Weyrich, R. Peikert, and M. Gross, "A practical structured light acquisition system for point-based geometry and texture," presented at the Eurographics/IEEE VGTC Symp. Proc. Point-Based Graphics, 2005.
- [4] S. Zhang, "High-resolution, High-speed 3-D Dynamically Deformable Shape Measurement Using Digital Fringe Projection Techniques," in *Advances in Measurement Systems*, M. K. Sharma, Ed., ed: InTech, 2010, pp. 29-50.
- [5] Z. Song, R. Chung, and X.-T. Zhang, "An Accurate and Robust Strip-Edge-Based Structured Light Means for Shiny Surface Micromasurement in 3-D," *IEEE Trans. Ind. Electron.*, vol. 60, pp. 1023-1032, 2013.
- [6] T.-W. Hui and G. K.-H. Pang, "3-D Measurement of Solder Paste Using Two-Step Phase Shift Profilometry," *IEEE Trans. Electron. Packag. Manuf.*, vol. 31, pp. 306-315, 2008.
- [7] Y. Wang, K. Liu, Q. Hao, X. Wang, D. L. Lau, and L. G. Hassebrook, "Robust Active Stereo Vision Using Kullback-Leibler Divergence," *IEEE Trans. Pattern Anal. Mach. Intell.*, vol. 34, pp. 548-563, 2012.
- [8] M. Gupta, Q. Yin, and S. K. Nayar, "Structured Light in Sunlight," presented at the Proc. IEEE Int. Conf. Comput. Vision (ICCV), 2013.
- [9] M. Gupta, A. Agrawal, A. Veeraraghavan, and S. Narasimhan, "A Practical Approach to 3D Scanning in the Presence of Interreflections, Subsurface Scattering and Defocus," *Int. J. Comput. Vision*, vol. 102, pp. 33-55, 2013.
- [10] T. Chen, H. P. A. Lensch, C. Fuchs, H.-p. Seidel, and M. Informatik, "Polarization and PhaseShifting for 3D Scanning of Translucent Objects," presented at the Proc. IEEE Conf. Comput. Vision and Pattern Recognition (CVPR), 2007.
- [11] A. Kolb, E. Barth, R. Koch, and R. Larsen, "Time-of-Flight Cameras in Computer Graphics," *Computer Graphics Forum*, vol. 29, 2010.
- [12] S. Schuon, C. Theobalt, J. Davis, and S. Thrun, "LidarBoost: Depth superresolution for ToF 3D shape scanning," presented at the Proc. IEEE Conf. Comput. Vision and Pattern Recognition (CVPR), 2009.
- [13] D. Scharstein, *View synthesis using stereo vision*. Berlin: Springer, 1999.
- [14] R. Hartley and A. Zisserman, *Multiple View Geometry in Computer Vision*: Cambridge University Press, 2003.
- [15] H. Chen and Z. Xu, "3D Map Building Based on Stereo Vision," presented at the Proc. IEEE Int. Conf. Netw., Sens. and Control (ICNSC), 2006.
- [16] N. Uchida, T. Shibahara, T. Aoki, H. Nakajima, and K. Kobayashi, "3D face recognition using passive stereo vision," presented at the Proc. IEEE Int. Conf. Image Process. (ICIP), 2005.
- [17] K. Miyazawa and T. Aoki, "A robot-based 3D body scanning system using passive stereo vision," presented at the Proc. IEEE Int. Conf. Image Process. (ICIP), 2008.

- [18] W. S. Fife and J. K. Archibald, "Improved Census Transforms for Resource-Optimized Stereo Vision," *IEEE Trans. Circuits Syst. Video Technol.*, vol. 23, pp. 60-73, 2013.
- [19] J. Batlle, E. Mouaddib, and J. Salvi, "Recent progress in coded structured light as a technique to solve the correspondence problem: a survey," *Pattern Recognition*, vol. 31, pp. 963-982, 7/31/ 1998.
- [20] J. Salvi, J. Pagès, and J. Batlle, "Pattern codification strategies in structured light systems," *Pattern Recognition*, vol. 37, pp. 827-849, 2004.
- [21] J. Salvi, J. Batlle, and E. Mouaddib, "A robust-coded pattern projection for dynamic 3D scene measurement," *Pattern Recognition Letters*, vol. 19, pp. 1055-1065, 1998.
- [22] S. Y. Chen, Y. F. Li, and J. Zhang, "Vision Processing for Realtime 3-D Data Acquisition Based on Coded Structured Light," *IEEE Trans. Image Process.*, vol. 17, pp. 167-176, 2008.
- [23] K. L. Boyer and A. C. Kak, "Color-Encoded Structured Light for Rapid Active Ranging," *IEEE Trans. Pattern Anal. Mach. Intell.*, vol. PAMI-9, pp. 14-28, 1987.
- [24] W.-H. Su, "Color-encoded fringe projection for 3D shape measurements," *Opt. Express*, vol. 15, pp. 13167-13181, 2007/10/01 2007.
- [25] J. L. Posdamer and M. D. Altschuler, "Surface measurement by space-encoded projected beam systems," *Computer Graphics and Image Processing*, vol. 18, pp. 1-17, 1982.
- [26] E. Horn and N. Kiryati, "Toward optimal structured light patterns," in *3-D Digital Imaging and Modeling, 1997. Proceedings., International Conference on Recent Advances in*, 1997, pp. 28-35.
- [27] D. Caspi, N. Kiryati, and J. Shamir, "Range Imaging With Adaptive Color Structured Light," *IEEE Trans. Pattern Anal. Mach. Intell.*, vol. 20, pp. 470-480, 1998.
- [28] P. H. Jian hui Pan, Song Zhang, and Fu-Pen Chaing, "Color n-ary gray code for 3-d shape measurement," in *Int Conf on Experimental Mechanics (ICEM)*, 2004.
- [29] J. Pagès, J. Salvi, C. Collewet, and J. Forest, "Optimised De Bruijn patterns for one-shot shape acquisition," *Image and Vision Computing*, vol. 23, pp. 707-720, 2005.
- [30] J. Pages, J. Salvi, and J. Forest, "A new optimised De Bruijn coding strategy for structured light patterns," presented at the Proc. Conf. Pattern Recognition (ICPR), 2004.
- [31] Z. Li, B. Curless, and S. M. Seitz, "Rapid shape acquisition using color structured light and multi-pass dynamic programming," in *Proc. of 1st Int. Symp. on 3D Data Process. Vis. and Transmission, 2002.* , 2002, pp. 24-36.
- [32] V. Couture, N. Martin, and S. Roy, "Unstructured Light Scanning Robust to Indirect Illumination and Depth Discontinuities," *Int. J. Comput. Vision*, vol. 108, pp. 204-221, 2014/07/01 2014.
- [33] P. Huang, "A Fast Three-Step Phase Shifting Algorithm for Real-Time Three-Dimensional Shape Measurement," *Frontiers in Optics 2007/Laser Science XXIII/Organic Materials and Devices for Displays and Energy Conversion*, 2007.
- [34] P. S. Huang and S. Zhang, "Fast three-step phase-shifting algorithm," *Appl. Opt.*, vol. 45, pp. 5086-5091, 2006.

- [35] K. Liu, Y. Wang, D. L. Lau, Q. Hao, and L. G. Hassebrook, "Dual-frequency pattern scheme for high-speed 3-D shape measurement," *Opt. Express*, vol. 18, pp. 5229-5244, 2010.
- [36] Y. Wang, K. Liu, Q. Hao, D. L. Lau, and L. G. Hassebrook, "Period Coded Phase Shifting Strategy for Real-time 3-D Structured Light Illumination," *IEEE Trans. Image Process.*, vol. 20, pp. 3001-3013, 2011.
- [37] S. Zhang, X. Li, and S.-T. Yau, "Multilevel quality-guided phase unwrapping algorithm for real-time three-dimensional shape reconstruction.," *Appl. Opt.*, vol. 46, pp. 50-7, 2007.
- [38] S. Zhang and S.-T. Yau, "High-resolution, real-time 3D absolute coordinate measurement based on a phase-shifting method," *Opt. Express*, vol. 14, pp. 2644-2649, 2006.
- [39] Y. Zhang, Z. Xiong, and F. Wu, "Unambiguous 3D measurement from speckle-embedded fringe," *Appl. Opt.*, vol. 52, pp. 7797-7805, 2013.
- [40] Y. Zhang, Z. Xiong, Z. Yang, and F. Wu, "Real-Time Scalable Depth Sensing With Hybrid Structured Light Illumination," *IEEE Trans. Image Process.*, vol. 23, pp. 97-109, 2014.
- [41] B. Freedman, A. Shpunt, M. Machline, and Y. Arieli, "Depth mapping using projected patterns," 2008.
- [42] F. Alhwarin, A. Ferrein, and I. Scholl, "IR Stereo Kinect: Improving Depth Images by Combining Structured Light with IR Stereo," in *PRICAI 2014: Trends in Artificial Intelligence*. vol. 8862, D.-N. Pham and S.-B. Park, Eds., ed: Springer International Publishing, 2014, pp. 409-421.
- [43] D. Scharstein and R. Szeliski, "High-accuracy stereo depth maps using structured light," presented at the Proc. IEEE Conf. Comput. Vision and Pattern Recognition (CVPR), 2003.
- [44] M. Takeda and K. Mutoh, "Fourier transform profilometry for the automatic measurement of 3-D object shapes," *Appl. Opt.*, vol. 22, pp. 3977-3982, 1983.
- [45] X. Su and W. Chen, "Fourier transform profilometry: a review," *Optics and Lasers in Engineering*, vol. 35, pp. 263-284, 2001.
- [46] H. Guo, "3-D Shape Measurement Based on Fourier Transform and Phase Shifting Method," Doctor of Philosophy, Mechanical Eng., Stony Brook University, NY, 2009.
- [47] D. Malacara, *Optical Shop Testing (Wiley Series in Pure and Applied Optics)*: Wiley-Interscience, 2007.
- [48] T. Chen, "Modulated phase-shifting for 3D scanning," presented at the Proc. IEEE Conf. Comput. Vision and Pattern Recognition (CVPR), 2008.
- [49] S. Gai and F. Da, "A novel phase-shifting method based on strip marker," *Optics and Lasers in Engineering*, vol. 48, pp. 205-211, 2010.
- [50] K. Itoh, "Analysis of the phase unwrapping algorithm," *Appl. Opt.*, vol. 21, p. 2470, 1982.
- [51] D. C. G. a. M. D. Pritt, *Two-dimensional phase unwrapping : theory, algorithms, and software*: John Wiley & Sons, 1998.
- [52] R. M. Goldstein, H. A. Zebker, and C. L. Werner, "Satellite radar interferometry: Two-dimensional phase unwrapping," *Radio Science*, vol. 23, pp. 713-720, 1988.
- [53] D. J. Bone, "Fourier fringe analysis: the two-dimensional phase unwrapping problem," *Appl. Opt.*, vol. 30, pp. 3627-3632, 1991/09/01 1991.

- [54] L. Meng, S. Fang, P. Yang, L. Wang, M. Komori, and A. Kubo, "Image-inpainting and quality-guided phase unwrapping algorithm," *Appl. Opt.*, vol. 51, pp. 2457-2462, 2012/05/01 2012.
- [55] K. Chen, J. Xi, and Y. Yu, "Quality-guided spatial phase unwrapping algorithm for fast three-dimensional measurement," *Optics Communications*, vol. 294, pp. 139-147, 5/1/ 2013.
- [56] M. Zhao, L. Huang, Q. Zhang, X. Su, A. Asundi, and Q. Kemao, "Quality-guided phase unwrapping technique: comparison of quality maps and guiding strategies," *Appl. Opt.*, vol. 50, pp. 6214-6224, 2011/11/20 2011.
- [57] T. Flynn, "Consistent 2-D phase unwrapping guided by a quality map," presented at the Int. Symp. Geosci. Remote Sens. (IGARSS), 1996.
- [58] L. Qian, J. F. Vesecky, and H. A. Zebker, "New approaches in interferometric SAR data processing," *IEEE Trans. Geosci. Remote Sens.*, vol. 30, pp. 560-567, 1992.
- [59] T. J. Flynn, "Two-dimensional phase unwrapping with minimum weighted discontinuity," *Journal of the Optical Society of America A*, vol. 14, p. 2692, 1997.
- [60] W. Gao, N. T. T. Huyen, H. S. Loi, and Q. Kemao, "Real-time 2D parallel windowed Fourier transform for fringe pattern analysis using Graphics Processing Unit," *Opt. Express*, vol. 17, pp. 23147-23152, 2009.
- [61] Q. Kemao, "Windowed Fourier Transform for Fringe Pattern Analysis," *Appl. Opt.*, vol. 43, pp. 2695-2702, 2004.
- [62] Q. Kemao, "Two-dimensional windowed Fourier transform for fringe pattern analysis: Principles, applications and implementations," *Optics and Lasers in Engineering*, vol. 45, pp. 304-317, 2007.
- [63] Q. Kemao, H. Wang, and W. Gao, "Windowed Fourier transform for fringe pattern analysis: theoretical analyses," *Appl. Opt.*, vol. 47, pp. 5408-5419, 2008.
- [64] A. Z. Abid, M. A. Gdeisat, D. R. Burton, M. J. Lalor, and F. Lilley, "Spatial fringe pattern analysis using the two-dimensional continuous wavelet transform employing a cost function," *Appl. Opt.*, vol. 46, pp. 6120-6126, 2007.
- [65] A. Dursun, S. Özder, and F. N. Ecevit, "Continuous wavelet transform analysis of projected fringe patterns," *Measurement Science and Technology*, vol. 15, p. 1768, 2004.
- [66] M. A. Gdeisat, A. Abid, D. R. Burton, M. J. Lalor, F. Lilley, C. Moore, *et al.*, "Spatial and temporal carrier fringe pattern demodulation using the one-dimensional continuous wavelet transform: Recent progress, challenges, and suggested developments," *Optics and Lasers in Engineering*, vol. 47, pp. 1348-1361, 2009.
- [67] T.-C. Hsung, D. Pak-Kong Lun, and W. W. L. Ng, "Efficient fringe image enhancement based on dual-tree complex wavelet transform," *Appl. Opt.*, vol. 50, pp. 3973-3986, 2011.
- [68] J. Zhong and J. Weng, "Spatial Carrier-Fringe Pattern Analysis by Means of Wavelet Transform: Wavelet Transform Profilometry," *Appl. Opt.*, vol. 43, pp. 4993-4998, 2004.
- [69] W. W.-L. Ng and D. P.-K. Lun, "Effective bias removal for fringe projection profilometry using the dual-tree complex wavelet transform," *Appl. Opt.*, vol. 51, pp. 5909-5916, 2012.

- [70] S. Zhang and S.-T. Yau, "High-speed three-dimensional shape measurement system using a modified two-plus-one phase-shifting algorithm," *Optical Engineering*, vol. 46, pp. 13603-113603-6, 2007.
- [71] F. Yang and X. He, "Two-step phase-shifting fringe projection profilometry: intensity derivative approach," *Appl. Opt.*, vol. 46, pp. 7172-7178, 2007.
- [72] P. Cong, Z. Xiong, Y. Zhang, S. Zhao, and F. Wu, "Accurate Dynamic 3D Sensing With Fourier-Assisted Phase Shifting," *IEEE J. Sel. Topics Signal Process.*, vol. 9, pp. 396-408, 2015.
- [73] S. K. Nayar, G. Krishnan, M. D. Grossberg, and R. Raskar, "Fast Separation of Direct and Global Components of a Scene Using High Frequency Illumination," *ACM Trans. Graph.*, vol. 25, pp. 935-944, 2006.
- [74] Budianto and D. P. K. Lun, "Inpainting For Fringe Projection Profilometry Based on Iterative Regularization," presented at the Int. Conf. Digital Signal Processing, Hong Kong, 2014.
- [75] M. Holroyd and J. Lawrence, "An analysis of using high-frequency sinusoidal illumination to measure the 3D shape of translucent objects," in *Proc. IEEE Conf. Comput. Vision and Pattern Recognition (CVPR)*, 2011, pp. 2985-2991.
- [76] M. Holroyd, J. Lawrence, and T. Zickler, "A Coaxial Optical Scanner for Synchronous Acquisition of 3D Geometry and Surface Reflectance," *ACM SIGGRAPH*, vol. 29, pp. 99:1--99:12, 2010.
- [77] S. K. Nayar, "Micro Phase Shifting," presented at the Proc. IEEE Conf. Comput. Vision and Pattern Recognition (CVPR), Providence, RI, 2012.
- [78] C. Hermans, Y. Francken, T. Cuyppers, and P. Bekaert, "Depth from sliding projections," presented at the Proc. IEEE Conf. Comput. Vision and Pattern Recognition (CVPR), 2009.
- [79] Y. Wang, S. Yang, and X. Gou, "Modified Fourier transform method for 3D profile measurement without phase unwrapping," *Opt. Lett.*, vol. 35, pp. 790-792, 2010.
- [80] J. Gass, A. Dakoff, and M. K. Kim, "Phase imaging without  $2\pi$  ambiguity by multiwavelength digital holography," *Opt. Lett.*, vol. 28, pp. 1141-1143, 2003.
- [81] W.-H. Su and H. Liu, "Calibration-based two-frequency projected fringe profilometry: a robust, accurate, and single-shot measurement for objects with large depth discontinuities," *Opt. Express*, vol. 14, pp. 9178-9187, 2006.
- [82] J. M. Huntley and H. Saldner, "Temporal phase-unwrapping algorithm for automated interferogram analysis," *Appl. Opt.*, vol. 32, pp. 3047-52, 1993.
- [83] Y. Wang and S. Zhang, "Novel phase-coding method for absolute phase retrieval," *Opt. Lett.*, vol. 37, pp. 2067-2069, 2012.
- [84] G. Sansoni, M. Carocci, and R. Rodella, "Three-Dimensional Vision Based on a Combination of Gray-Code and Phase-Shift Light Projection: Analysis and Compensation of the Systematic Errors," *Appl. Opt.*, vol. 38, p. 6565, 1999.
- [85] Y. Liu, X. Su, and Q. Zhang, "A novel encoded-phase technique for phase measuring profilometry," *Opt. Express*, vol. 19, pp. 14137-14144, 2011.
- [86] B. Budianto and D. P. K. Lun, "Inpainting For Fringe Projection Profilometry Based on Geometrically Guided Iterative Regularization," *IEEE Trans. Image Process.*, vol. 24, pp. 5531-5542, 2015.
- [87] J. Park and A. C. Kak, "3D Modeling of Optically Challenging Objects," *IEEE Trans. Vis. Comput. Graphics*, vol. 14, pp. 246-262, 2008.

- [88] S. Nayar, X.-S. Fang, and T. Boult, "Separation of Reflection Components Using Color and Polarization," *Int. J. Comput. Vision*, vol. 21, pp. 163-186 LA - English, 1997.
- [89] V. Couture, N. Martin, and S. Roy, "Unstructured light scanning to overcome interreflections," presented at the Proc. IEEE Int. Conf. Computer Vision (ICCV), 2011.
- [90] PingTan, S. Lin, L. Quan, and H.-Y. Shum, "Highlight removal by illumination-constrained inpainting," presented at the Proc. IEEE Int. Conf. Computer Vision (ICCV), Nice, France, 2003.
- [91] R. T. Tan, K. Nishino, and K. Ikeuchi, "Separating reflection components based on chromaticity and noise analysis," *IEEE Trans. Pattern Anal. Mach. Intell.*, vol. 26, pp. 1373-1379, 2004.
- [92] H.-L. Shen and Z.-H. Zheng, "Real-time highlight removal using intensity ratio," *Appl. Opt.*, vol. 52, pp. 4483-4493, 2013.
- [93] H.-L. Shen, H.-G. Zhang, S.-J. Shao, and J. H. Xin, "Chromaticity-based separation of reflection components in a single image," *Pattern Recognition*, vol. 41, pp. 2461-2469, 2008.
- [94] H. Kim, H. Jin, S. Hadap, and I. Kweon, "Specular Reflection Separation Using Dark Channel Prior," presented at the Proc. IEEE Conf. Comput. Vision and Pattern Recognition (CVPR), 2013.
- [95] P. Koirala, P. Pant, M. Hauta-Kasari, and J. Parkkinen, "Highlight detection and removal from spectral image," *Journal of the Optical Society of America A*, vol. 28, pp. 2284-2291, 2011.
- [96] S. A. Shafer, "Using color to separate reflection components," *Color Research & Application*, vol. 10, pp. 210-218, 1985.
- [97] J. W. Park and K. H. Lee, "Inpainting Highlights Using Color Line Projection," *IEICE - Trans. Inf. Syst.*, vol. E90-D, pp. 250-257, 2007.
- [98] J. H. Massig and J. Heppner, "Fringe-pattern analysis with high accuracy by use of the Fourier-transform method: theory and experimental tests," *Appl. Opt.*, vol. 40, pp. 2081-2088, 2001/05/01 2001.
- [99] C. Roddier and F. Roddier, "Interferogram analysis using Fourier transform techniques," *Appl. Opt.*, vol. 26, pp. 1668-1673, 1987/05/01 1987.
- [100] M. Dai and Y. Wang, "Fringe extrapolation technique based on Fourier transform for interferogram analysis," *Opt. Letters*, vol. 34, pp. 956-958, 2009/04/01 2009.
- [101] W. Haibin, W. Liquan, Y. Xiaoyang, B. Hao, and W. Di, "Exploration on exemplar-based encoding image inpainting of coded structured light system," in *Strategic Technology (IFOST), 2011 6th International Forum on*, 2011, pp. 1092-1095.
- [102] A. Criminisi, P. Perez, and K. Toyama, "Region filling and object removal by exemplar-based image inpainting," *IEEE Trans. Image Process.*, vol. 13, pp. 1200-1212, 2004.
- [103] O. Guleryuz, "Nonlinear approximation based image recovery using adaptive sparse reconstructions and iterated denoising-part II: adaptive algorithms," *IEEE Trans. Image Process.*, vol. 15, pp. 555 - 571, 2006.
- [104] O. G. Guleryuz, "Nonlinear approximation based image recovery using adaptive sparse reconstructions and iterated denoising-part I: theory," *IEEE Trans. Image Process.*, vol. 15, pp. 539-554, 2006.

- [105] F. Li and T. Zeng, "A Universal Variational Framework for Sparsity-Based Image Inpainting," *IEEE Trans. Image Process.*, vol. 23, pp. 4242-4254, 2014.
- [106] Y.-R. Li, L. Shen, and B. W. Suter, "Adaptive Inpainting Algorithm Based on DCT Induced Wavelet Regularization," *IEEE Trans. Image Process.*, vol. 22, pp. 752-763, 2013.
- [107] J.-F. Cai, R. H. Chan, and Z. Shen, "A framelet-based image inpainting algorithm," *Applied and Computational Harmonic Analysis*, vol. 24, pp. 131-149, 2008.
- [108] G. S. Guoshen Yu, "DCT image denoising: a simple and effective image denoising algorithm," *Image Processing On Line*, vol. 1, 2011.
- [109] A. N. Akansu and P. R. Haddad, *Multiresolution Signal Decomposition: Transforms, Subbands, and Wavelets*: Academic Press, 2000.
- [110] J.-L. Starck, E. J. Candes, and D. L. Donoho, "The curvelet transform for image denoising," *IEEE Trans. Electron. Packag. Manuf.*, vol. 11, pp. 670-684, 2002.
- [111] D. L. Donoho, "De-noising by soft-thresholding," *IEEE Trans. Inf. Theory*, vol. 41, pp. 613-627, 1995.
- [112] I. W. Selesnick, R. G. Baraniuk, and N. C. Kingsbury, "The dual-tree complex wavelet transform," *IEEE Signal Process. Mag.*, vol. 22, pp. 123-151, 2005.
- [113] T.-C. Hsung, D. P. Lun, and W. W. L. Ng, "Zero spectrum removal using joint bilateral filter for Fourier transform profilometry," presented at the Visual Communications and Image Processing (VCIP), 2011 IEEE, 2011.
- [114] N. Otsu, "A Threshold Selection Method from Gray-Level Histograms," *IEEE Trans. Syst. Man Cybern. (1971-1995)*, vol. 9, pp. 62-66, 1979.
- [115] J. Kittler and J. Illingworth, "Minimum error thresholding," *Pattern Recognition*, vol. 19, pp. 41-47, 1986.
- [116] C. M. Bishop, *Pattern Recognition and Machine Learning (Information Science and Statistics)*. Secaucus, NJ, USA: Springer-Verlag New York, Inc., 2006.
- [117] R. T. Trevor Hastie, Jerome Friedman, *The Elements of Statistical Learning: Data Mining, Inference, and Prediction*, 2 ed.: Springer-Verlag New York, 2009.
- [118] S. Masnou, "Disocclusion: a variational approach using level lines," *IEEE Trans. Image Process.*, vol. 11, pp. 68-76, 2002.
- [119] F. Cao, Y. Gousseau, S. Masnou, and P. Pérez, "Geometrically Guided Exemplar-Based Inpainting," *SIAM Journal on Imaging Sciences*, vol. 4, pp. 1143-1179, 2011.
- [120] J. F. Hughes, A. Van Dam, J. D. Foley, and S. K. Feiner, *Computer Graphics: Principles and Practice*: Addison-Wesley, 2013.
- [121] E. Bertolazzi and M. Frego, "G1 fitting with clothoids," *Math. Methods Appl. Sci.*, vol. 38, pp. 881-897, 2015.
- [122] A. Criminisi, P. Perez, and K. Toyama, "Object removal by exemplar-based inpainting," presented at the Proc. IEEE Conf. Comput. Vision and Pattern Recognition (CVPR), 2003.
- [123] D. Tschumperle and R. Deriche, "Vector-valued image regularization with PDEs: a common framework for different applications," *IEEE Trans. Pattern Anal. Mach. Intell.*, vol. 27, pp. 506-517, 2005.

- [124] D. Weisheng, S. Guangming, and L. Xin, "Nonlocal Image Restoration With Bilateral Variance Estimation: A Low-Rank Approach," *IEEE Trans. Image Process.*, vol. 22, pp. 700-711, 2013.
- [125] J. J. Huang, W. C. Siu, and T. R. Liu, "Fast Image Interpolation via Random Forests," *IEEE Trans. Image Process.*, vol. 24, pp. 3232-3245, 2015.
- [126] B. Budianto, P. K. D. Lun, and T.-C. Hsung, "Marker encoded fringe projection profilometry for efficient 3D model acquisition," *Appl. Opt.*, vol. 53, pp. 7442-7453, 2014.
- [127] H. Cui, W. Liao, N. Dai, and X. Cheng, "A flexible phase-shifting method with absolute phase marker retrieval," *Measurement*, vol. 45, pp. 101-108, 2012.
- [128] N. Kingsbury, "A dual-tree complex wavelet transform with improved orthogonality and symmetry properties," presented at the Proc. IEEE Int. Conf. on Image Process. (ICIP), 2000.
- [129] L. Sendur and I. W. Selesnick, "Bivariate shrinkage with local variance estimation," *IEEE Signal Process. Lett.*, vol. 9, pp. 438-441, 2002.
- [130] L. Sendur and I. W. Selesnick, "Bivariate shrinkage functions for wavelet-based denoising exploiting interscale dependency," *IEEE Trans. Signal Process.*, vol. 50, pp. 2744-2756, 2002.
- [131] D. L. Donoho and I. M. Johnstone, "Adapting to Unknown Smoothness via Wavelet Shrinkage," *Journal of the American Statistical Association*, vol. 90, pp. 1200-1224, 1995.
- [132] A. Vo and S. Orintara, "On the distributions of the relative phase of complex wavelet coefficients," presented at the IEEE Int. Symp. Circuits and Syst. (ISCAS), 2009.
- [133] A. Vo and S. Orintara, "A study of relative phase in complex wavelet domain: Property, statistics and applications in texture image retrieval and segmentation," *Signal Processing: Image Communication*, vol. 25, pp. 28-46, 2010.
- [134] J. Fauqueur, N. Kingsbury, and R. Anderson, "Multiscale Keypoint Detection using the Dual-Tree Complex Wavelet Transform," presented at the Proc. IEEE Int. Conf. Image Process. (ICIP), 2006.
- [135] H. Shi, B. Hu, and J. Zhang, "A Novel Scheme for the Design of Approximate Hilbert Transform Pairs of Orthonormal Wavelet Bases," *IEEE Trans. Signal Process.*, vol. 56, pp. 2289-2297, 2008.
- [136] Budianto and D. P. K. Lun, "Robust Fringe Projection Profilometry via Sparse Representation," *IEEE Trans. Image Process.*, vol. 25, pp. 1726-1739, 2016.
- [137] I. W. Selesnick, "Resonance-based signal decomposition: A new sparsity-enabled signal analysis method," *Signal Processing*, vol. 91, pp. 2793-2809, 2011.
- [138] İ. Bayram and I. W. Selesnick, "A Dual-Tree Rational-Dilation Complex Wavelet Transform," *IEEE Trans. Signal Process.*, vol. 59, pp. 6251-6256, 2011.
- [139] M. V. Afonso, J. M. Bioucas-Dias, and M. A. T. Figueiredo, "Fast Image Recovery Using Variable Splitting and Constrained Optimization," *IEEE Trans. Image Process.*, vol. 19, pp. 2345-2356, 2010.
- [140] M. V. Afonso, J. M. Bioucas-Dias, and M. A. T. Figueiredo, "An Augmented Lagrangian Approach to the Constrained Optimization Formulation of

- Imaging Inverse Problems," *IEEE Trans. Image Process.*, vol. 20, pp. 681-695, 2011.
- [141] M. A. T. Figueiredo, J. M. Bioucas-Dias, and M. V. Afonso, "Fast frame-based image deconvolution using variable splitting and constrained optimization," presented at the IEEE/SP 15th Workshop on Statistical Signal Processing, 2009.
- [142] M. Aharon, M. Elad, and A. Bruckstein, "K-SVD: An Algorithm for Designing Overcomplete Dictionaries for Sparse Representation," *IEEE Trans. Signal Process.*, vol. 54, pp. 4311-4322, 2006.
- [143] S. Chen, D. Donoho, and M. Saunders, "Atomic Decomposition by Basis Pursuit," *SIAM J. on Sci. Comput.*, vol. 20, pp. 33-61, 1998.
- [144] R. Tibshirani, "Regression shrinkage and selection via the lasso: a retrospective," *Journal of the Royal Statistical Society: Series B (Statistical Methodology)*, vol. 73, pp. 273-282, 2011.
- [145] J. Mairal, F. Bach, J. Ponce, and G. Sapiro, "Online Dictionary Learning for Sparse Coding," presented at the Proc. Int. Conf. Machine Learning (ICML), New York, NY, USA, 2009.
- [146] S. G. Mallat and Z. Zhang, "Matching pursuits with time-frequency dictionaries," *IEEE Trans. Signal Process.*, vol. 41, pp. 3397-3415, 1993.
- [147] Z. Jiang, Z. Lin, and L. S. Davis, "Label Consistent K-SVD: Learning a Discriminative Dictionary for Recognition," *IEEE Trans. Pattern Anal. Mach. Intell.*, vol. 35, pp. 2651-2664, 2013.
- [148] J. Mairal, F. Bach, and J. Ponce, "Task-Driven Dictionary Learning," *IEEE Trans. Pattern Anal. Mach. Intell.*, vol. 34, pp. 791-804, 2012.
- [149] D.-S. Pham and S. Venkatesh, "Joint learning and dictionary construction for pattern recognition," presented at the Proc. IEEE Conf. Comput. Vision and Pattern Recognition (CVPR), 2008.
- [150] J. Mairal, F. Bach, J. Ponce, G. Sapiro, and A. Zisserman, "Discriminative learned dictionaries for local image analysis," presented at the Proc. IEEE Conf. Comput. Vision and Pattern Recognition (CVPR), 2008.
- [151] Q. Zhang and B. Li, "Discriminative K-SVD for dictionary learning in face recognition," presented at the Proc. IEEE Conf. Comput. Vision and Pattern Recognition (CVPR), 2010.
- [152] I. Ramirez, P. Sprechmann, and G. Sapiro, "Classification and clustering via dictionary learning with structured incoherence and shared features," presented at the Proc. IEEE Conf. Comput. Vision and Pattern Recognition (CVPR), 2010.
- [153] M. Yang, L. Zhang, X. Feng, and D. Zhang, "Sparse Representation Based Fisher Discrimination Dictionary Learning for Image Classification," *Int. J. Comput. Vision*, vol. 109, pp. 209-232, 2014.
- [154] I. W. Selesnick, "Wavelet Transform With Tunable Q-Factor," *IEEE Trans. Signal Process.*, vol. 59, pp. 3560-3575, 2011.
- [155] D. Liu, J. Gu, Y. Hitomi, M. Gupta, T. Mitsunaga, and S. K. Nayar, "Efficient Space-Time Sampling with Pixel-Wise Coded Exposure for High-Speed Imaging," *IEEE Trans. Pattern Anal. Mach. Intell.*, vol. 36, pp. 248-260, 2014.